TECHNISCHE UNIVERSITÄT MÜNCHEN
Fakultät für Physik

Max-Planck-Institut für Physik
(Werner-Heisenberg-Institut)

CLAWS

An Injection Background Monitoring System for the Second and Third Phase of the SuperKEKB Commissioning

Hendrik Uwe Windel

Vollständiger Abdruck der von der Fakultät für Physik der Technischen Universität München zur Erlangung des akademischen Grades eines

Doktors der Naturwissenschaften (Dr. rer. nat.)

genehmigten Dissertation.

Vorsitzender:

Prof. Dr. Andreas Weiler

Prüfer der Dissertation:

1. Hon.-Prof. Dr. Allen C. Caldwell
2. Prof. Dr. Stephan Paul

Die Dissertation wurde am 27. September 2021 bei der Technischen Universität München eingereicht und durch die Fakultät für Physik am 30. November 2021 angenommen.

Technische Universität München
Fakultät für Physik

Max-Planck-Institut für Physik
(Werner-Heisenberg-Institut)

Claws

An Injection Background Monitoring System for the Second and Third Phase of the SuperKEKB Commissioning

Dissertation by
Hendrik Uwe Windel

December 22, 2021

Hendrik Uwe Windel: CLAWS - An Injection Background Monitoring System for the Second and Third Phase of the SuperKEKB Commissioning, December 22, 2021.

ABSTRACT

The Belle 2 experiment is a collider-based high energy physics experiment at the intensity and precision frontier and is based at the only collision point of the SuperKEKB collider located at the KEK research institute in Tsukuba, Japan. The B-factory circulates electrons and positrons at asymmetric beam energies of 7 GeV and 4 GeV, respectively, and aims at reaching the world highest instantaneous luminosity of $6 \cdot 10^{35}\,\mathrm{cm}^{-2}\,\mathrm{s}^{-1}$ within a decade of commissioning in 2025. Substantially decreasing beam currents due to collisions are compensated by top-up injections at 50 Hz. These injections cause a considerable injection induced beam background at the interaction point (IP) eventually decreasing the overall performance especially of the Belle 2 vertex detectors. A detailed knowledge of the background conditions at the IP is the basis for a successful mitigation of the injection induced beam background. The development and performance of a dedicated injection background monitoring system for SuperKEKB is presented in this thesis.

The Claws system is developed in two distinct detector designs for the Phases 2 and 3 of the SuperKEKB commissioning campaign which started at the end of March 2018. The detector design consists of a scintillating tile with silicon photomultiplier read-out detecting mostly charged particles. In Phase 2, two detectors ladders with 8 independent channels each have been placed in 22 mm distance around the interaction point inside the Belle 2 detector. A C++-based DAQ software applies a fast reconstruction and other analyses to the recorded waveforms featuring up to 10 000 continuous particle revolutions at a sampling rate of 1.25 GHz. The analysis results are displayed with an update rate of around 1 Hz in the SuperKEKB and Belle 2 control rooms considerably improving the understanding of the background conditions at the IP. For Phase 3, a total of 32 single-channel newly developed Claws modules are placed at multiple locations on the final focussing magnets in the interaction area and read out by an extended DAQ system.

Furthermore, this thesis investigates the capabilities of the developed detector systems and studies the injection induced background behavior using the data collected in Phase 2. It is shown that the Claws system achieves a time resolution of (347 ± 2) ps for 10 MIP signals and a MIP response stability of $-3.0\,\%$ to $+5.5\,\%$ over the course of 3.5 month. This precision allows studying bunch-by-bunch beam behavior and enables performing advanced time dependent analyses. The thesis demonstrates in detail the potential of Claws of detecting minimal irregularities of the beam which builds the basis for the present use of the system as a beam abort system substantially outperforming all previous systems.

ZUSAMMENFASSUNG

Das Belle 2-Experiment ist ein Beschleuniger-basiertes Hochenergiephysikexperiment an der Energie- und Intensitätsfront. Es befindet sich an dem einzigen Kollisionspunkt des SuperKEKB-Beschleunigers welcher sich am KEK-Forschungsinstitut in Tsukuba, Japan, befindet. Die B-Mesonen-Fabrik kollidiert Elektronen und Positronen mit asymmetrischen Strahlenergien von 7 GeV bzw. 4 GeV und zielt darauf ab, die welthöchste Luminosität von $6 \cdot 10^{35}\,\mathrm{cm}^{-2}\,\mathrm{s}^{-1}$ nach etwa 10 Jahren der Inbetriebnahme im Jahr 2025 zu erreichen. Stark abnehmende Strahlströme aufgrund der hohen Kollisionsrate werden durch Teilcheninjektionen mit 50 Hz kompensiert. Diese Teilcheninjektionen verursachen einen beträchtlichen injektionsinduzierten Strahlenuntergrund am Kollisionspunkt, der die Gesamtleistung insbesondere der Belle II-Vertexdetektoren verringert. Eine detailliertes Wissen des Strahlenuntergrunds am Kollisionspunkt ist die Grundlage für eine erfolgreiche Reduzierung des injektionsinduzierten Strahluntergrunds. In dieser Arbeit wird die Entwicklung und Leistungsfähigkeit eines Systems zur Überwachung des injektionsinduzierten Strahlenuntergrunds für den SuperKEKB-Beschleuniger vorgestellt.

Das Claws-System wurde in zwei verschiedenen Detektordesigns für die Phasen 2 und 3 der Inbetriebnahmekampagnen des SuperKEKB-Beschleunigers entwickelt. Das Detektordesign besteht aus einer szintillierenden Kachel welche mit einem Silizium-Photomultiplier ausgelesen wird. Das System ist hauptsächlich sensitiv für geladene Teilchen. In Phase 2 wurden zwei Detektorleitern mit jeweils acht unabhängigen Kanälen im Abstand von 22 mm um den Kollisionspunkt im Belle 2-Detektor platziert. Eine C++-basierte Software zur Steuerung und Datennahme wendet eine schnelle Rekonstruktion und andere Analysen auf die aufgezeichneten Wellenformen an, welche bis zu 10 000 Teilchenumläufe mit einer Abtastrate von 1,25 GHz beinhalten. Die Analyseergebnisse werden mit einer Aktualisierungsrate von etwa 1 Hz in den Kontrollräumen des SuperKEKB-Beschleunigers und des Belle 2-Detektors angezeigt, was das Verständnis des Strahlenuntergrunds am Kollisionspunkt erheblich verbessert. Für die Phase 3 wurden insgesamt 32 Claws-Module mit je einem Kanal neu entwickelt und an mehreren Stellen um die Fokussierungsmagneten im Interaktionsbereich platziert und von einem erweiterten Datennahmesystem gesteuert und ausgelesen.

Darüber hinaus wird in dieser Arbeit die Leistungsfähigkeit der entwickelten Detektorsysteme untersucht und der injektionsinduzierte Strahlenuntergrund anhand der in Phase 2 gesammelten Daten untersucht. Es wird gezeigt, dass das Claws-System eine Zeitauflösung von (347 ± 2) ps für Signale von 10 MIP und eine stabile MIP-Resonanz von $-3{,}0\,\%$ to $+5{,}5\,\%$ über einen Zeitraum von 3,5 Monaten erreicht. Diese Präzision ermöglicht die Untersuchung des Strahlverhaltens individuell für jedes Teilchenpaket

und die Durchführung zeitabhängiger Analysen. Diese Dissertation demonstriert detailliert das Potenzial des CLAWS-Systems minimale Unregelmäßigkeiten in den Teilchenstrahlen zu erkennen was die Grundlage für den derzeitigen Einsatz des Systems als Strahlenabbruchsystem bildet und damit alle bisherigen Systeme deutlich übertrifft.

CONTENTS

LIST OF FIGURES

LIST OF TABLES

INTRODUCTION

The Standard Model of particle physics is the current theory describing the interactions at a fundamental level from the smallest to the largest scales in the universe. However, several observations such as the matter anti-matter asymmetry in the universe remain unexplained. New physics beyond the Standard Model is needed. Collider-based experiments at the intensity and precision frontier are one option tackling the unsolved challenges in high energy physics. The Belle 2 experiment is such an experiment with the goal of finding deviations in the Standard Model processes. The corresponding Belle 2 detector is located at the only collision point of the new SuperKEKB collider which is located at the KEK research institute in Tsukuba, Japan. The collider circulates electrons and positrons with asymmetric energies of 4 GeV and 8 GeV, respectively. The center of mass energy of 10.58 GeV is slightly above the $\Upsilon(4S)$ resonance making the collider a B-meson factory. It will reach the worlds highest instantaneous luminosity of $6 \cdot 10^{35}\,\mathrm{cm}^{-2}\,\mathrm{s}^{-1}$ by two different measures. First, by using high beam currents of 2.8 A and 2.0 A for electrons and positrons, respectively, and, second, by applying the novel nano beam scheme in which the colliding beams are squeezed down to a few tens of nanometers at the interaction point. The new collider started operation after around 10 years of construction in 2016 and is forseen to reach its design luminosity in 2025.

Reaching this high luminosity is a challenging task. The long commissioning time of around 9 years is the result of a step-wise increase of the beam currents and the step-wise narrowing of the beams at the collision point. Especially the increase of the beam currents is accompanied by increasing beam backgrounds. These negatively affect the detector performance, leads to an increased degrading or damaging of the detectors. In addition, the high luminosity results in short beam life times of $\mathcal{O}(10\,\mathrm{min})$. For this reason, new particles are injected with a rate of 50 Hz and at full energy into the main rings. These continuous injections are the origin of an additional injection induced particle background. Mitigating these beam backgrounds is of paramount importance for the success of the Belle 2 experiment.

The SuperKEKB commissioning campaign is referred to as BEAST and is divided into three phases. In each phase a different set of dedicated background detectors monitored the background conditions in the interaction region. In the scope of this thesis, the CLAWS detector system specialized on the observation of injection induced background is developed for the second and third phase of BEAST starting in early 2018. The distinct geometric and physical requirements led to two different concepts of the detector hardware. The data acquisition software was developed from scratch for the second commissioning phase and was extended for the usage in the third

phase. The detector system is mostly sensitive to charged particles and is capable of recording the time development of the injection induced background over up to 40 000 particle revolutions at a high sampling rate of 1.25 GHz. A subsequent analysis of the data recorded in BEAST phase 2 presents the capabilities of the detector system. For example, beam turbulences which can potentially lead to high intensity beam losses damaging especially the innermost Belle 2 sub-detectors are reliably detected.

This thesis is organized in four parts. The first part sets the theoretical and experimental foundation of this thesis. The current understanding of our nature and their limitations are summarized in chapter 1. Chapter 2 introduces the SuperKEKB collider and recaps the basics of accelerator physics. The Belle 2 experiment and detector is briefly introduced in chapter 3 before the different BEAST phases are described in detail in chapter 4.

The second part presents the developed CLAWS systems. It begins with a detailed description of the two different detector hardwares and their characterization and calibration in chapter 5 and is followed by the detailed explanation of the data acquisition software implementation in chapter 6. Furthermore, the developed online monitors and a comprehensive benchmark of the real-time capabilities of the system are presented.

The third part of this thesis illustrates the potential of the developed detector system using the data recorded at the experiment. Chapter 7 analyzes the raw data in terms of the timing capabilities, the hit energy spectra and the time structure of the injection induced backgrounds. Afterwards, the fast reconstructed data, which was saved over the entire run time, is studied in detail regarding the cooling time of the injection induced background.

The fourth and last part recaps the presented developments and findings and outlines the present and future use of the CLAWS detector system.

This thesis provides work towards a better understanding of the injection induced background at the SuperKEKB collider. The system developed in the scope of this thesis provides exclusively relevant information about the background processes at the interaction point in the second phase of the SuperKEKB commissioning. In the third commissioning phase, CLAWS became a permanent background detector offering detailed information about the injection induced beam background observed within the Belle 2 detector. Furthermore, the system sets the foundation for a beam abort system at the SuperKEKB collider outperforming the previous existing systems substantially.

Part I

EXPERIMENTAL AND THEORETICAL BACKGROUND

1

PHYSICS MOTIVATION

This chapter sets the physics motivation and experimental foundation for the work presented in this thesis. It begins with an introduction of the Standard Model (SM) before the open questions of particle physics are discussed. In the last section, a state of the art experiment testing the SM is presented.

1.1 THE STANDARD MODEL

The *Standard Model* is the state of the art particle physics theory describing most of the interactions between the fundamental building blocks our nature consists of. There are bosons with integer spins and fermions with a spin of $\frac{1}{2}$. The gauge bosons with a spin of 1 are the carriers of the elementary forces: the strong force is mediated by gluons, the weak force by W- and Z-bosons, and the electromagnetic force by photons. All visible matter is formed by charged fermions consisting of six quarks, three leptons, and three neutrinos. Fermions are further organized in three families, each consisting of two quarks, one lepton and one neutrino. Quarks form composite particles which are referred to as hadrons. Hadrons consisting of a quark anti-quark pair are called mesons and hadrons with three quarks are referred to as baryons. The Higgs boson with spin zero is the measurable manifestation of the everything surrounding and mass giving Higgs field. In addition, each particle in the SM, except the bosons, has an anti-particle with equal properties but the charge which has an opposite sign.

This is the SM particle content as it is predicted since almost 50 years. Its last major theory extension followed on the observation of CP-violation in the decays of neutral kaons by Cronin and Fitch in 1964 [1] which cannot be explained with only two fermion generations which was the state of the art knowledge at that time. In 1973, Kobayashi and Maskawa solved this issue by proposing a third fermion family which introduces a CP-violating phase [2, 3]. From that day on, the theoretical physicists have developed a theory consisting of 17 particles in total. At that time, nine of the particles had been undiscovered predictions and were waiting for their discovery.

Fortunately, it took not too long for the first discoveries. Already one year later, the first of the nine undiscovered particles, the charm quark, was independently observed at the *Stanford Linear Accelerator Center (SLAC)* and at the *Brookhaven National Laboratory* [4, 5] and followed by four more particle discoveries in the 1970s. Over the last decades, the high energy particle physics community chased the undiscovered particles with always bigger and more powerful particle colliders. From the year

2000 on, all but one particle predicted by the SM had been discovered. This last missing particle, a spin zero boson, has been proposed in the 1960s, already, and is needed to explain why gauge bosons have mass. The Higgs field provides this mass generating mechanism through electroweak symmetry breaking. The Higgs boson is the observable manifestation of this Higgs field [6–8] and was finally discovered at the *Large Hadron Collider (LHC)* completing the SM [9, 10] in 2012.

Since then, the self-consistency of the SM was verified in multiple experiments around the world. Fig. 1.1 illustrates a summary of several SM total production cross section measurements which are corrected for branching fractions. In addition, it compares the corresponding theoretical expectations with observations by the ATLAS experiment at CERN. The plot features for the all processes an agreement between the theory prediction and the experimental measurement and illustrates nicely the consistency of the SM. At the current level of reached collision energies and experimental precision, the SM is so far the best tested theory describing the nature from the smallest to the largest scales in the universe at a fundamental level.

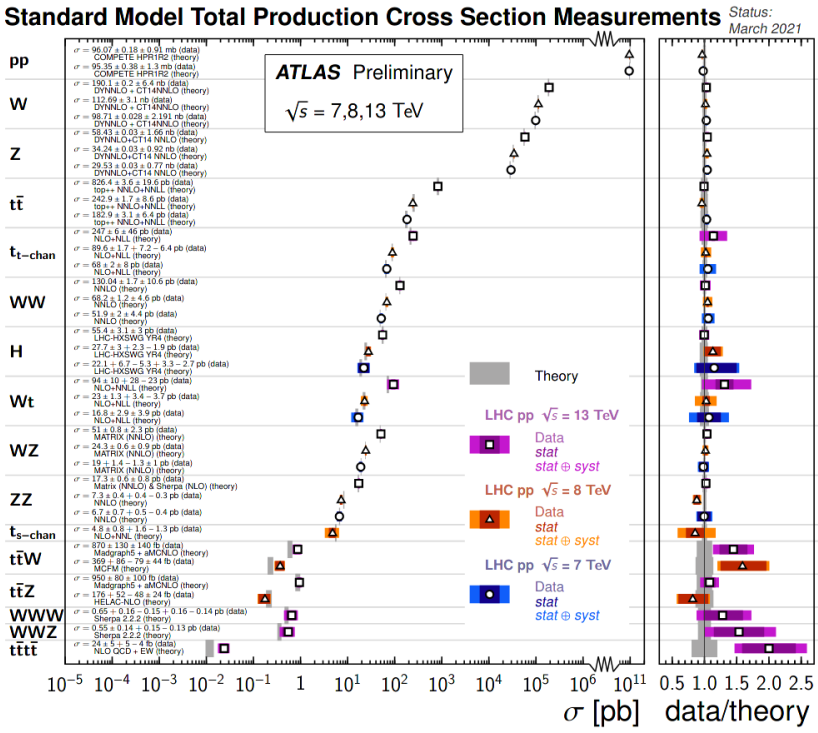

Figure 1.1: Standard Model total production cross section measurements. Taken from [11] and modified.

1.2 OPEN QUESTIONS IN PARTICLE PHYSICS

Despite its great success in describing the fundamental particles and their interactions, many fundamental questions are unanswered by the SM. For example:

- The fundamental gravitational force is not explained.
- There is no explanation for dark matter which accounts for around 85 % of the matter in the universe.
- At the cosmological scale, the observed matter-antimatter asymmetry is by orders of magnitude too large to be explained by known SM processes.

The listed shortcomings illustrate the incompleteness of the SM. New theories beyond the SM are required to answer the open questions. These new theories mostly predict either new particles and/or small deviations of existing SM processes. However, there are dozens of new theories existing in parallel at the moment. For a long time the high energy particle physic was driven by finding all components of the well established SM. The future, in contrast, is experimentally driven. The physics community needs to discover unknown particles or reduce the uncertainties of known processes in order to find the road to the *theory of everything*. In general, the effort of finding new physics beyond the SM can be categorized in three different approaches:

The first category are *passive observations* of beyond SM phenomena. These can happen, for example, with earth or space based telescopes observing the cosmological structures in the visible universe. Another option is the passive search with ground based detectors. This is done, for example, by the *Cosinus experiment* [12] in the Gran Sasso underground laboratory. It searches for dark matter particles in dependence of the annual rotation of the earth around the sun.

The second category is the active search with *collider-based experiments at the energy frontier*. In this approach, particles are accelerated on and on increasing their energy level. Because this approach is very resource consuming, there is only one collider, the LHC, allowing for experiments following this concept. It is the biggest machine ever build by humans and aims at the direct production of new particles by colliding protons at very high energies. Several new physics models such as the supersymmetry predict new particles at the TeV scale. However, there were no new particles observed up to now.

The last category is the active search with *accelerator-based experiments at the intensity & precision frontier*. In this approach, SM processes are precisely measured at moderate energies with the goal of finding deviations from the SM predictions. One example is the *g-2 experiment* [13] at Fermilab. g-2 aims at measuring the muon anomalous magnetic moment a factor of four more precisely than previous experiments achieved. The most recent experimental results made the experiment more famous in the general

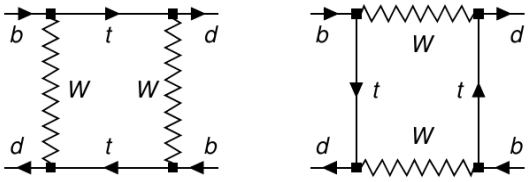

Figure 1.2: Dominant contributions to $B\bar{B}$-mixing in the Standard Model. Taken from [15].

public since it measured a deviation of $4.2\,\sigma$ to the SM predictions [14] which can be interpreted as a first hint of new physics. However, the deviation is not yet a clear discovery and needs to be verified with more data.

An historic example shows that results from collider-based experiments at the intensity and precision frontier have been quite useful narrowing energy ranges for theoretical predicted but undiscovered particles. In 1987, the ARGUS experiment at the DORIS collider at DESY [15] operated at the $\Upsilon(4S)$ resonance which is slightly above the energy threshold producing entangled B-meson pairs originating from e^+e^- collisions. ARGUS was able to measure the first evidence of $B\bar{B}$-mixing by observing the reaction $\Upsilon(4S) \to B^0\bar{B}^0 \to B^0B^0$. At that time, the top quark was not yet discovered and its mass limit of $m_t > 23\,\text{GeV}$ was driven by direct searches. However, the dominant contributions to the $B\bar{B}$-mixing come from box diagrams with intermediate top quarks as illustrated in Fig. 1.2. Thanks to this measurement, the new top mass limit of $m_t > 50\,\text{GeV}$ gave the first indication that the top quark could not be directly observed at SLAC and LEP, CERN. Finally, in 1995, the top quark was produced by TEVATRON at the *Fermi National Accelerator Laboratory*, USA, with a mass of $m_t = 171\,\text{GeV}$ [15].

1.3 TESTING THE STANDARD MODEL

Another collider-based experiment at the precision frontier is the *Belle 2 experiment* [16] at the SuperKEKB collider located at the KEK research laboratory in Tsukuba, Japan. Its main physics goals are to improve the precision of the SM parameters and to search for new physics in the flavour sector. Its high precision measurements are enabled by two main factors. First, colliding leptons instead of baryons leads to a precise knowledge of the initial state and to less background processes. Second, the SuperKEKB collider aims at reaching an unprecedented luminosity allowing to observe also rare SM processes.

The Belle 2 experiment has several advantages compared to other experiments which are perfectly suited to test several open questions in particle physics. Similar to ARGUS, most of the data will be collected at the $\Upsilon(4S)$ resonance producing entangled B-meson pairs at a low background environment. This allows for a high trigger rate and the efficient reconstruction of several final states containing photons. The asymmetric beam energies provide a boost of the center-of-mass system enabling

$B-$ and $D-$ mesons to travel a reasonable distance before decaying. Thanks to the excellent vertex resolution, the travelling distances can be measured precisely allowing for measurements of the time-dependent *charge-parity symmetry (CP)* violation. The precise knowledge rather than reconstructing the initial state of the collision allows to perform missing mass analyses inferring the existence of new particles, e.g. dark matter candidates, via energy and momentum conservation of the observed decay products. The full reconstruction of B or D decays in a hadronic or semileptonic final state enables to measure rare decays with neutrinos with a minimal model dependence.

The road to these and even more measurements sensitive to new physics beyond the standard model is a high luminosity. The Belle 2 experiment tackles the challenging task of finding new physics phenomena by analyzing the collision products delivered by the SuperKEKB collider. An unprecedented luminosity level was already reached by SuperKEKB: The current luminosity world record of $3.12 \cdot 10^{34}\,\mathrm{cm}^{-1}\,\mathrm{s}^{-1}$ was reached on June 22, 2021. One of the main factors of reaching such high luminosities is to decrease the betatron function β^* at the interaction point which can be described as the envelope in which the circulating particles are able to move (more detailed information about the luminosity and betatron function is given in Section 2.2 and Section 2.1.2). Fig. 1.3 depicts the achieved betatron functions at the interaction point of several existing and planned colliders versus time. It shows that the SuperKEKB collider (in red) achieved already the worlds smallest betatron function. Overall, the trend of smaller and smaller betatron functions is observable among all depicted colliders and will be one key factor for many future collider experiments. The SuperKEKB collider reaches a new milestone which is beneficial for all future lepton colliders and the collider-based high energy physics community.

Nonetheless, Fig. 1.3 also shows that there is still a long way to go for the SuperKEKB collider in order to reach the final design of the betatron function. For this reason, the next chapter introduces the SuperKEKB collider, the accelerator physics behind, and presents the challenges the SuperKEKB faces before reaching its full performance.

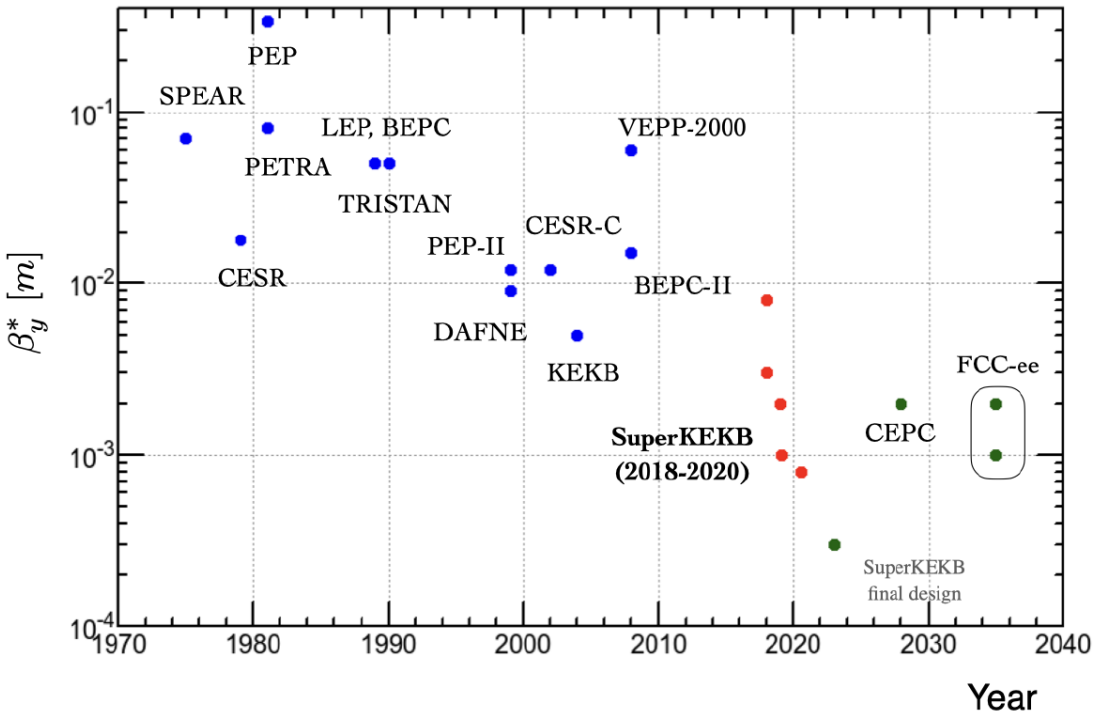

Figure 1.3: β_y^* versus time and collider. The blue dots illustrate mostly non-active accelerators or colliders, the red dots demonstrate the history of the SuperKEKB collider, and the green dots are projections of future goals. Taken from [17].

2

THE SUPERKEKB COLLIDER

At the end of June, 2010, the KEKB collider at the high energy accelerator research organization KEK in Tsukuba, Japan, finished operation after more than 10 years of runtime. The electron-positron synchrotron machine delivered an integrated luminosity of 1041 fb^{-1} to the Belle experiment. Colliding leptons with an instantaneous peak luminosity of $2.108 \cdot 10^{34}\,\mathrm{cm}^{-2}\,\mathrm{s}^{-1}$ the KEKB machine achieved a world record which is surpassed only by his successor: SuperKEKB. [18, 19]

Fig. 2.1 illustrates a sketch of the SuperKEKB collider which is a major upgrade of the KEKB machine. As part of the upgrade process several parts of the accelerator and collider infrastructure have been replaced, such as the positron ring, the damping ring as well as the final focussing system. Electrons and positrons circulate with asymmetric energies of 7 GeV and 4 GeV, respectively, in the two separate storage rings. The *high energy ring (HER)* for electrons as well as the *low energy ring (LER)* for positrons operate with beam currents of 2.8 A and 2.0 A [20], respectively, and have a circumference of around 3 km resulting in a revolution time of $T_{\mathrm{rev}} = 10.0614\,\mu\mathrm{s}$. The center-of-mass energy is primarily chosen as 10.58 GeV corresponding to the $\Upsilon(4s)$ resonance. This resonance is the lightest state of two bound bottom quarks decaying into two B mesons making SuperKEKB a *B factory* for the corresponding Belle 2 detector. The detector is placed at the only collision point in the *Tsukuba Area* located at the northern part of the main rings. More details about the Belle 2 detector follows in Chapter 3. SuperKEKB aims at a target instantaneous luminosity of $\mathcal{L} = 6 \cdot 10^{35}\,\mathrm{cm}^{-2}\,\mathrm{s}^{-1}$ [20] which is a factor 30 higher than its predecessor KEKB achieved. SuperKEKB is expected to deliver around 50 ab^{-1} of integrated luminosity which is a factor 50 larger than Belle received from KEKB [16, 19]. This ambitious luminosity goal is reached by its large beam currents and the worlds first *nano beam scheme* (more details in Section 2.2). Low beam life times of the order of several minutes are the side-effect of the high instantaneous luminosity. Keeping the beam currents constant over time demands continuous injections at a design injection rate of 50 Hz resulting in a periodic background contribution from injections which is studied in detail in the analysis part of this thesis.

In order to guide the particles around the collider rings, dedicated beam optics hardware is installed: There are normal-conducting dipole magnets guiding the particles around the arcs, quadrupole magnets are placed in sequences in order to focus the particle beam in the vertical and horizontal direction, and the *superconducting final focusing magnets (QCS)* left and right of the IP squeeze the colliding beams to an unprecedented level of a few tens of nanometers. In the Nikko, Fuji, and Oho areas

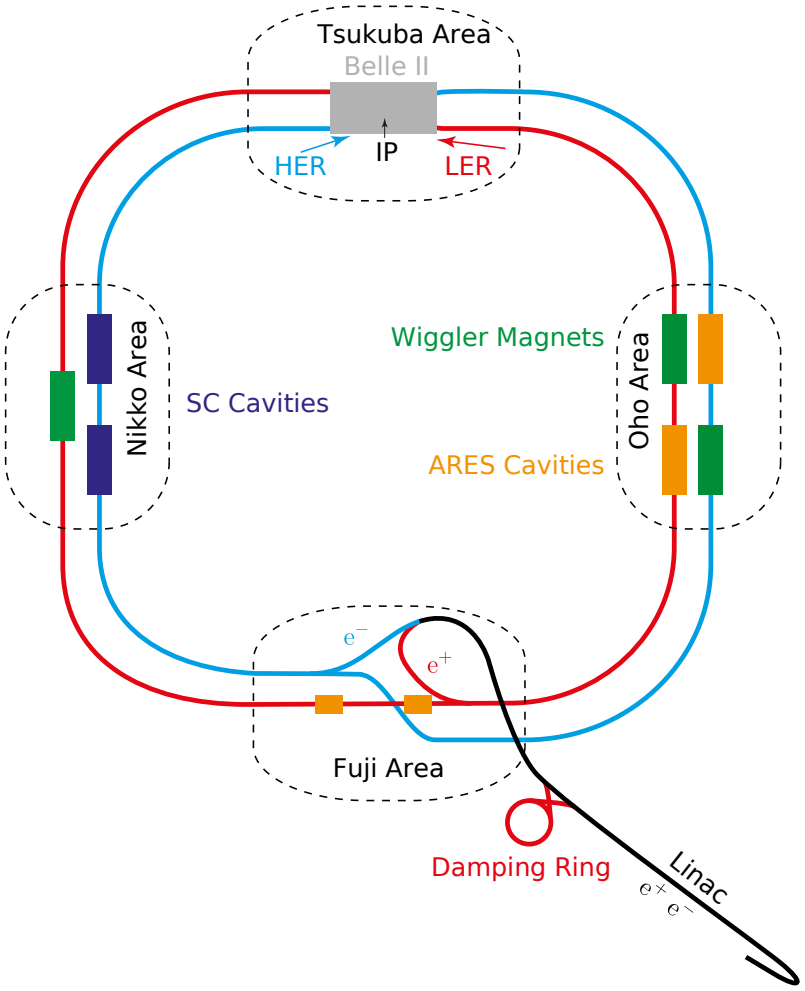

Figure 2.1: Sketch of the SuperKEKB e^+e^- collider. Taken from [21] and modified.

dedicated RF cavities compensate for beam energy loss using *accelerator resonantly coupled with energy storage (ARES)* and *superconducting RF (SC)* cavities. The Nikko and Oho areas contain, in addition, *Wiggler* magnets performing active synchrotron radiation dampening on the beam which will be explained in detail in Section 2.1.5.

In this chapter, first, the beam properties and dynamics in the storage ring are introduced in Section 2.1 before the novel nano beam scheme of the final focussing is presented in Section 2.2. Section 2.3 gives detailed insights into the particle generation and the following injection into the main rings. At the end an overview of the expected beam background sources is given in Section 2.4.

The next sections introduces the basic beam properties and dynamics of the particles in a synchrotron storage ring at the high-energy limit of $v/c \approx 1$. The presented information is based on the excellent literature found in [19, 22–27]. However, the information provided here is only an introduction and cannot cover the entirety of knowledge about accelerator physics.

2.1 BEAM PROPERTIES, DYNAMICS & DAMPENING

In most particle accelerators, particles do not propagate as single particles through the beam pipe but in so called *bunches* which are collections of several million or billion particles. The bunches are located at stable areas in the phase space defined by the RF elements. These stable regions are centered around multiples of the RF phase ϕ_s and are referred to as *RF buckets*. In SuperKEKB the time distance between two buckets is $T_{\text{bucket}} = 1.965\,\text{ns}$. However, by design not every RF bucket is occupied by a bunch in order to fit the collision frequency to the read-out capabilities of the detector. For example, in SuperKEKB each ring is filled with 2500 bunches with a design distance in time of $T_{\text{bunch}} = 2 \cdot T_{\text{bucket}} = 3.93\,\text{ns}$. Each bunch consists of around $65 \cdot 10^9$ positrons or $90 \cdot 10^9$ electrons. The particles of a bunch are arranged in a three dimensional normal distribution which implies that the vast majority of particles do not travel on the *ideal orbit*. Almost each particle differs of the *ideal particle* in energy E and space ($x(z)$, $x'(z)$, $y(z)$, $y'(z)$, z). A schematic coordinate system is illustrated in Fig. 2.2 (left).

Noting the large amount of particles with each six degrees of freedom it would be impractical to calculate the trajectory along the ring for every individual particle. For this reason, the following sections introduce a representation of the particle beam by its boundaries or envelopes and their properties and behavior.

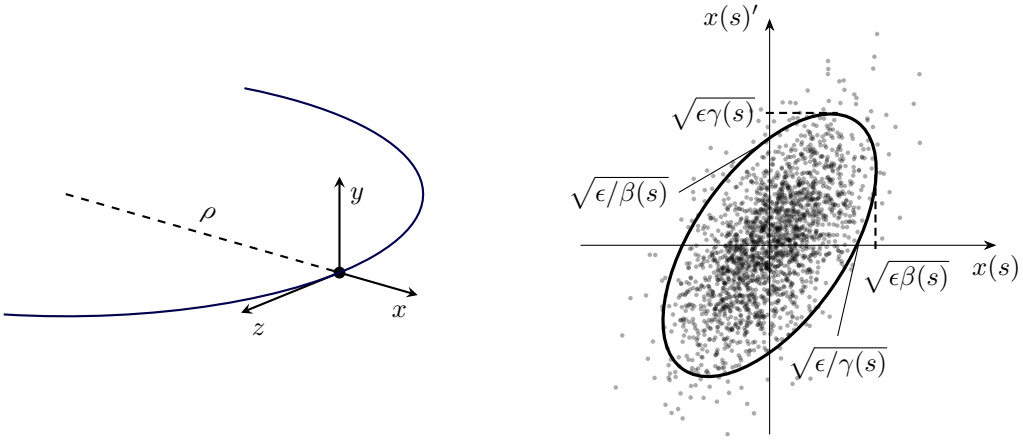

Figure 2.2: *(left)* Coordinate system used to describe the particle motion. *(right)* Exemplary drawing of the emittance. The area and limits of the emittance ellipse are defined by the Twiss parameters.

2.1.1 *Transversal Beam Emittance*

The beam emittance is defined as the occupied volume of the particle bunch in the phase space of position and momentum. In the approximation of linear beam

dynamics the coupling between the horizontal and vertical beam dynamics is ignored. The emittance is expressed as

$$\epsilon = \gamma(z)\, x(z)^2 + 2\,\alpha(z)\, x(z)\, x'(z) + \beta(z)\, x'(z)^2. \tag{2.1}$$

The parameters $\alpha(z)$, $\beta(z)$, and $\gamma(z)$ are functions of the location along the ideal orbit and known as *Twiss parameters* [22]. They describe the eccentricity, orientation and area of the *phase ellipse* as illustrated in Fig. 2.2 (right). The area of the ellipse is given with $A = \pi\epsilon$ resulting in a correlation of the Twiss parameters of $1 = \beta\gamma - \alpha^2$. Using this ellipse it is possible to calculate the trajectories of the particle beam along the ring if their initial conditions are known. *Liouville's theorem* states that under the influence of conservative forces the density in phase space is preserved. For this reason is the area of the ellipse and the emittance an invariant of the particle motion. If we assume that

$$\epsilon = \gamma_0\, x_0^2 + 2\,\alpha_0\, x_0\, x_0' + \beta_0\, {x_0'}^2 \tag{2.2}$$

describes the phase ellipse of the beam at $z = 0$. Any change of the particle trajectory from $z = 0$ to any other point $z \neq 0$ is given by the transformation

$$\begin{bmatrix} x(z) \\ x'(z) \end{bmatrix} = \mathcal{M} \begin{bmatrix} x_0 \\ x_0' \end{bmatrix} \tag{2.3}$$

with $\mathcal{M}$ as the *transformation matrix* which is unique for each component, e.g. bending or focussing magnets or the product of any combination along the beam line. As an example, we define

$$\mathcal{M} = \begin{bmatrix} C(z) & S(z) \\ C'(z) & S'(z) \end{bmatrix}.$$

Solving Eq. (2.3) for x_0 and x_0' and inserting it into Eq. (2.1) we yield after sorting of the coefficients

$$\begin{aligned} \epsilon = \quad & x^2(z) && (S'^2\gamma_0 - 2\,S'C'\alpha_0 + C'^2\beta_0) + \\ & x(z)\,x'(z) && (-SS'\gamma_0 + S'C\alpha_0 + SC'\alpha_0 - CC'\beta_0)\cdot 2 + \\ & x'(z)^2 && (S^2\gamma_0 - 2\,SC\alpha_0 + C^2\beta_0) \end{aligned}$$

where the dependence of C, C', S, and S' of the position z along the beam transport line was omitted for better readability. Comparing this result to Eq. (2.1) we can formulate the Twiss parameters in matrix representation

$$\begin{bmatrix} \beta \\ \alpha \\ \gamma \end{bmatrix} = \begin{bmatrix} C^2 & -2SC & S^2 \\ -CC' & (S'C + SC') & -SS' \\ C'^2 & -2S'C' & S'^2 \end{bmatrix} \begin{bmatrix} \beta_0 \\ \alpha_0 \\ \gamma_0 \end{bmatrix}. \tag{2.4}$$

The area of the ellipse $A = \epsilon\pi$ is still the same. Though, the shape and angle of the ellipse is changed by the propagation of the beam through the *magnet lattice* which is the arrangement of the different magnets along the beam transport line. The discussion above only treats the phase space spanned by the $(x,\ x')$ plane but is applied similar to the $(y,\ y')$ plane.

2.1.2 *Betatron Oscillations*

So far we learned that the emittance of a particle bunch is an invariant under the propagation through the magnet lattice and can be understood as a kind of temperature of the beam. Now, we will have a look at what happens to the single particle within the bunch under the shape and orientation transformation of the phase ellipse.

The differential equation of motion of a single particle is given by

$$u''(z) + k(z)\, u(z) = 0 \tag{2.5}$$

where $u(z)$ represents one of the transversal degrees of freedom in space, x or y, and the magnet lattice function $k(z)$. A general solution of this equation is found by applying the method of variation of integration constants and the usage of an z-dependent amplitude and phase [22]. It is given by

$$u_i(z) = \sqrt{\epsilon\beta(z)}\ cos\left(\psi(z) - \psi_{0;\,i}\right) \tag{2.6}$$

with the emittance ϵ and $\psi_{0;\,i}$ as integration constants and the *phase function* $\psi(z) = \sqrt{k_0}(z - z_0)$. The function $u_i(z)$ describes the transversal movement of the i-th beam particle and is known as *betatron oscillation function*. It is a quasi periodic function with varying amplitude and frequency. By selecting for every point z of the orbit the i-th particle with the true value of $cos\left(\psi(z) - \psi_{0;\,i}\right) = \pm 1$, one yields the *beam envelope* as illustrated in Fig. 2.3. The beam envelope is therefore give with

$$E(z) = \pm\sqrt{\epsilon\beta(z)} \tag{2.7}$$

and contains all particles of the ellipse defined by the beam emittance. While the beam emittance is constant over the course of the orbit, the *betatron function* $\beta(z)$ represents the external forces of the magnet lattice and especially of the focusing magnets. As we will see later in more detail, the betatron function is an important parameter to optimize when increasing the luminosity.

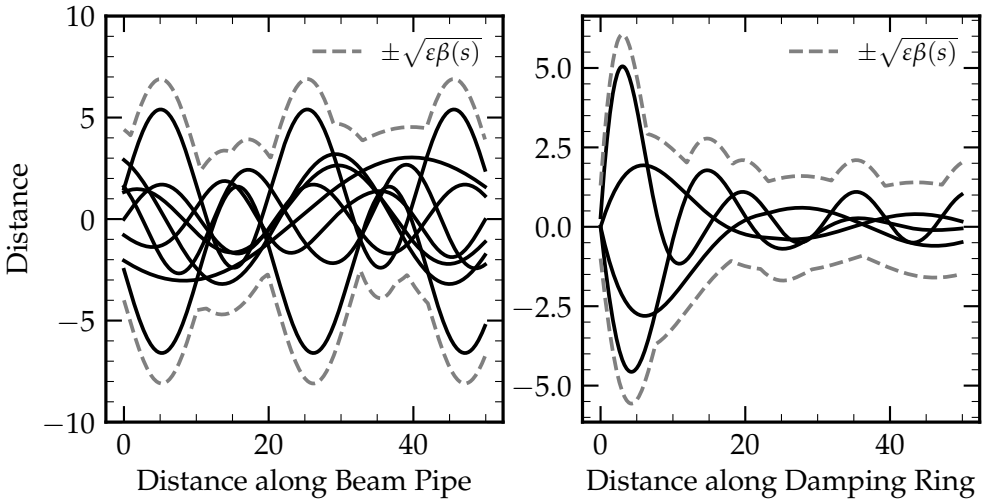

Figure 2.3: Sketch of betatron oscillations drawn with continuous lines and the corresponding beam envelope drawn with dashed lines. The emittance and the beam envelope are decreased in a damping illustrated on the right.

A number which we will study later in the analysis chapters is the so called *betatron tune*. It defines the number of transversal oscillations per turn and is given as

$$\nu_{x;\,y} = \frac{1}{2\pi} \oint \frac{dz}{\beta(z)}. \tag{2.8}$$

For SuperKEKB the design parameters for the horizontal ν_x and vertical ν_y design tunes are 45.5/45.6 and 58.5/52.6 for the LER and HER, respectively.

2.1.3 *Momentum Dispersion*

So far, we covered the particle displacements in the transversal direction with the ideal momentum. In order to describe the dynamics of real particles one has to include chromatic effects caused by a deviation in the beam energy. The trajectory of a particle with the wrong energy in any magnet or electric field deviates from the ideal particle with the ideal energy. The analytical *dispersion function* is given as

$$D(z) = \int_0^z \frac{1}{\rho(\bar{z})} \left[S(z)C(\bar{z}) - C(z)S(\bar{z}) \right] d\bar{z}. \tag{2.9}$$

Its physical interpretation is understood best with the introduction of the relative energy deviation from the ideal momentum δ. The function $f(x) = \delta D(z)$ determines the offset of the ideal orbit. It shows that unlike the emittance the momentum dispersion changes throughout the propagation of the particles along the beam pipe. It is important to note that there is only a contribution to the dispersion function when there is at least one magnet manipulating the beam.

The described mechanisms of the momentum dispersion does not only contribute to the already introduced betatron oscillations acting in the transverse directions. In addition, there are contributions to a longitudinal motion within the bunch which is introduced in the next paragraph.

2.1.4 *Synchrotron Oscillations*

The longitudinal degree of freedom was so far not taken into account. The momentum dispersion explained above leads to a transversal and longitudinal displacement of the single particles with respect to the ideal particle. Effects of the longitudinal displacement of a particle is illustrated in Fig. 2.4. A longitudinal displaced particle arrives at the acceleration stage phase-shifted. Depending on the sign of the displacement the particle either experiences a larger or lower acceleration with respect to the ideal particle. Remembering that we are acting in the high energy limit with $v/c \approx 1$, the acceleration is proportional to an increase of the particle energy. The *slip factor* η relates to the fractional change in the *orbit period* τ with respect to the energy E increase by

$$\frac{\Delta\tau}{\tau} = \eta \frac{\Delta E}{E} \,. \tag{2.10}$$

Using the slip factor η we now can introduce the *synchrotron tune* representing - similar to the betatron tune - the number of oscillations per turn, but as longitudinal oscillation:

$$\nu_z = \sqrt{\frac{h\eta\, eV\, cos(\phi_z)}{2\pi E}} \,. \tag{2.11}$$

The newly introduced *harmonic number h* is a high integer number relating the particle revolution frequency f_{rev} and the frequency of the RF system f_{RF} with $f_{\text{RF}} = h f_{\text{rev}}$. For the calculations we assumed small amplitude synchrotron oscillations.

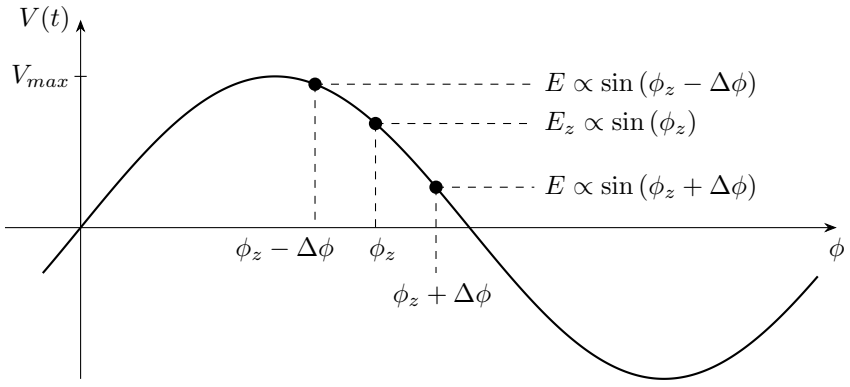

Figure 2.4: Phase dependent energy gain of the particle from an RF wave.

For SuperKEKB, the design synchrotron tunes are 0.0213 and 0.0117 for the LER and HER, respectively, and therefore notably smaller than the betatron oscillations as presented previously.

2.1.5 *Radiation Dampening*

Betatron and synchrotron oscillations lead to particle movements within the bunch. This increases the chance of intra bunch interactions which are responsible for undesired beam backgrounds. However, a relativistic particle undergoing centripetal acceleration radiates parts of their own energy as *synchrotron radiation* in the direction of the tangent to the trajectory. This emission reduces the magnitude of the momentum of the particle in all three dimensions. On the other hand, the particle acceleration with RF waves keeps the longitudinal momentum constant over long periods. As a consequence the transversal and longitudinal emittance reduces which in principle violates Liouville's theorem. However, the theorem does only apply for conservative forces which excludes intra bunch interactions.

This procedure is known as *synchrotron radiation dampening* and is widely used in e^+e^- machines. At the SuperKEKB storage rings the dampening effect is increased by dedicated wiggler magnets. However, despite the damping effect the emittances never reach zero, but stabilize at an equilibrium between the radiation dampening and excitation caused by the magnet lattice and intra bunch interactions. In general, the horizontal emittance in the bending plane is significantly larger than the vertical emittance.

2.2 LUMINOSITY & NANO BEAM SCHEME

The luminosity $\mathcal{L}$ is next to the center-of-mass energy the most important performance parameter of a particle collider. It defines the intensity of colliding beam machines and is crucial for deriving the number events observed over a period of time. Especially the high precision measurements carried out at the SuperKEKB collider depend on a high luminosity. The number of detected collision events given the luminosity is expressed by

$$N = A\sigma \int \mathcal{L} \mathrm{d}t \,, \tag{2.12}$$

with the detector acceptance A and the cross-section of the underlying process σ. The time-integral over the instantaneous luminosity is known as integrated luminosity $\mathcal{L}_{\mathrm{int}}$. For the success of the experiment it is important to maximize the number of detected events N. For this reason, the luminosity is optimized since A is a detector parameter and σ a physical constant.

By definition, the luminosity $\mathcal{L}$ is the density of collision centers in the target multiplied by the number of particles colliding with this target per unit time [22]. In the case of the SuperKEKB collider, one beam is the target of the other and the luminosity is written as

$$\mathcal{L} = f_{\text{rev}} \cdot \frac{N_{e^-} N_{e^+}}{4\pi \sqrt{\epsilon_x \beta_x^*} \sqrt{\epsilon_y \beta_y^*}} \cdot \mathcal{F} \,, \tag{2.13}$$

with the revolution frequency f_{rev} and the total number of electrons and positron in the main rings $N_{e^\pm}$. The factor $\mathcal{F} \leq 1$ accounts for the crossing angle and other effects. These parameters are all fixed by the machine and cannot be varied to further increase the luminosity. However, the measures of the colliding plane $\sigma_{x/y} = \sqrt{\epsilon_{x/y} \beta_{x/y}^*}$ with the betatron function at the IP $\beta_{x/y}^*$ are optimizable and are one of the main subjects of the time-consuming SuperKEKB commissioning. The goal for the vertical betatron function at the IP is $\beta_y^* = 0.27\,\text{mm}$ and $0.30\,\text{mm}$ for LER and HER, respectively.

In order to reach a factor 30 larger luminosity compared to its predecessor, two distinct measures are applied. First, the beam currents are doubled which increases the luminosity by a factor of 1.5. Second, a further increase by a factor of 20 will be achieved by minimizing the colliding areas of the two beams at the IP using the novel *nano beam scheme*.

NANO BEAM SCHEME The idea of the nano beam scheme for a circular collider was first proposed in 2006 [28] and consists of a small emittance and a small betatron function at the IP compared to the bunch length. For SuperKEKB the bunch measures at the IP differ by around one order of magnitude for each dimension. The bunch length increases at the IP while the horizontal size shrinks to around $10\,\mu\text{m}$. The smallest measure is reached for the vertical beam size with $59\,\text{nm}$. In comparison, the horizontal and vertical bunch size at the IP of KEKB was around $46\,\mu\text{m}$ and $54\,\mu\text{m}$, respectively, and therefore substantially larger [29]. Fig. 2.5 illustrates the beam shapes of KEKB (top) and SuperKEKB (bottom). The considerable large crossing angle of $2\phi = 83\,\text{mrad}$[1] is specifically chosen in order to minimize the *effective bunch length* $d = (\sigma_x^* / \phi)$ which is the horizontal size of the cutting plane of the two crossing bunches.

1 For a better imagination of that number: This is around 1.2 times the angle at which the Leaning Tower of Pisa leans.

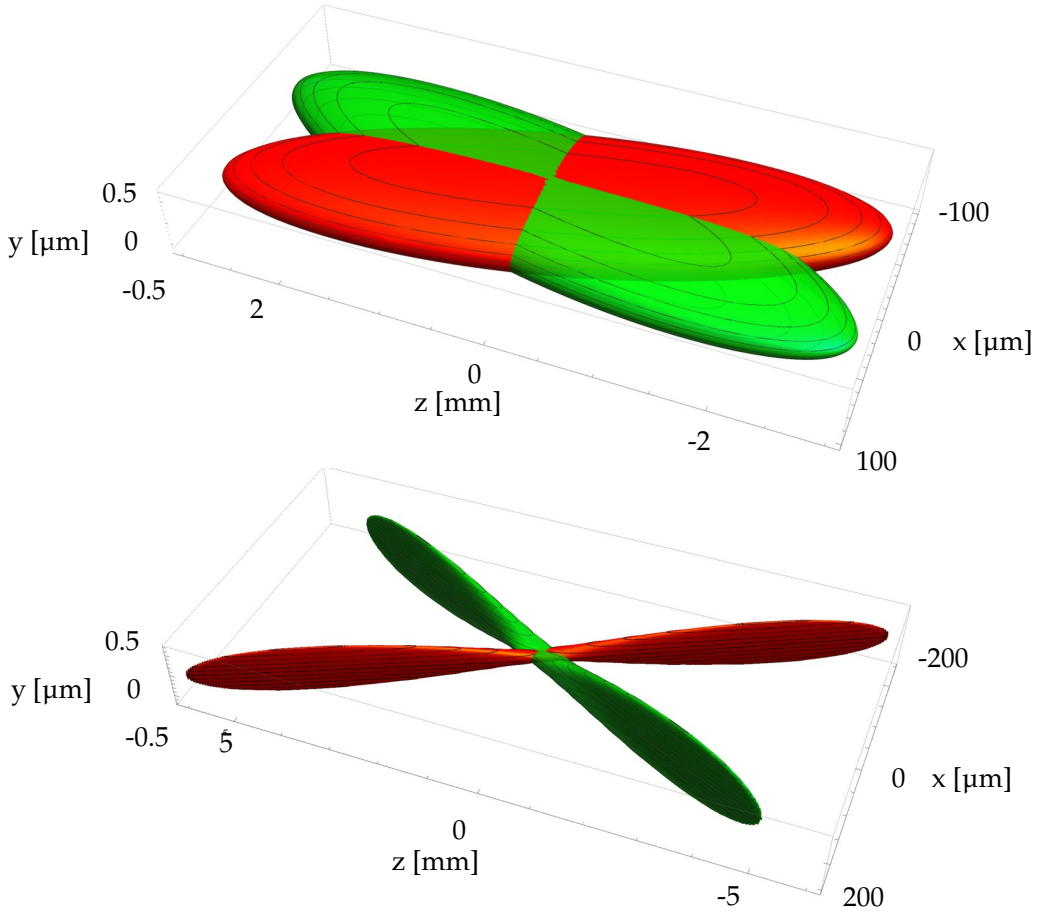

Figure 2.5: Bunch geometries at the IP of KEKB *(top)* and SuperKEKB *(bottom)*. Taken from [30] and modified.

2.3 PARTICLE GENERATION, LINAC & PARTICLE INJECTION

As part of the SuperKEKB upgrade the particle generation and injection structure was modified. Table 2.1 compares the previous KEKB parameters with the design parameters of SuperKEKB. In addition to the different beam energies various other parameters are changed. The biggest differences are observed for the bunch charges which are a factor of 5 and 4 larger and the vertical and horizontal emittances which are up to a factor 5 and 105 smaller for HER and LER, respectively. These three parameters are mandatory for reaching the high luminosity levels as discussed in the previous section.

In the following, the injection process will be illustrated from the particle generation of the electrons and positrons until the particle injection into the SuperKEKB main rings.

	KEKB		SuperKEKB	
	e^-	e^+	e^-	e^+
Beam energy [GeV]	8	3.5	7	4
Bunch charge [nC]	1	1(10*)	5	4(10*)
Normalized vertical emittance [mm mrad]	100	2100	20	20
Normalized horizontal emittance [mm mrad]	100	2100	50	100
Energy spread [%]	0.050	0.125	0.080	0.070
Bunch length [mm]	1.3	2.6	1.3	0.7
Max bunch repetition [Hz]	50			

* Primary electron beam for positron production.

Table 2.1: Main Parameters of the KEKB and SuperKEKB injector linacs. Taken from [31].

PARTICLE GENERATION & LINAC SuperKEKB requires high charge and low emittance bunches before the injection into the main rings. The particle production begins with a photocathode RF gun consisting of a Ytterbium-doped laser with a center wavelength of 259 nm and a pulse width of 30 ps [32]. The gun shoots at a target producing 5 nC electrons at a repetition rate of 25 Hz [32]. The RF gun location is depicted in the schematic of the SuperKEKB linac illustrated in Fig. 2.6. After the e^- production, the electrons are accelerated by a linear accelerator to 1.5 GeV and bent in the J-ARC and further accelerated to 3.5 GeV. At this point there are two different paths the electrons can take. The first option is an acceleration to 7 GeV followed by the injection into the HER ring of SuperKEKB which is explained in more detail in the next paragraph. The second path guides the electrons at a target with the goal

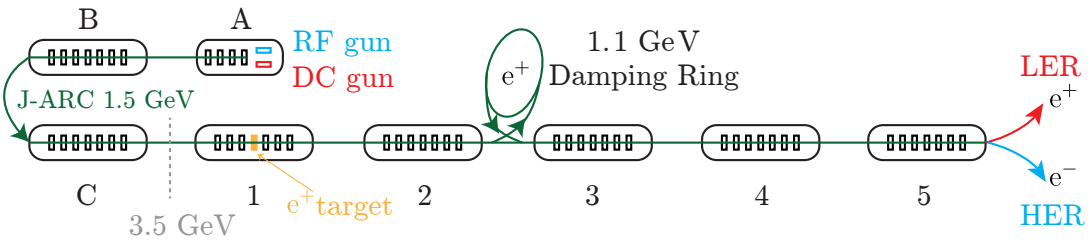

Figure 2.6: Schematic of the SuperKEKB injector linac structure. Taken from [21].

of producing positrons. The electrons are shot at e.g. a tungsten[2] target producing high energetic bremsstrahlung photons. The photons then produces electrons and positron via the pair production process. Magnetic fields behind the target separate the positrons from the electrons. During run time, the electrons switch pulse-wise between the paths.

The produced positrons have a high emittance of around $\epsilon_{x;\,y} = 1500\,\mu\text{m}$ [33] and are therefore guided into the dedicated damping ring. In the damping ring the positrons are accelerated to 1.1 GeV and the emittance is reduced down to the design value. Afterwards, the positrons are re-injected into the main linac, accelerated to 4 GeV and injected into the LER main ring. Both, electrons and positrons use the same linear accelerator before their injection into the corresponding main ring.

PARTICLE INJECTION Large beam losses due to background effects and the high luminosity result in a low beam life time of $\mathcal{O}(10\,\text{min})$. For this reason uses SuperKEKB a *top-up injection* scheme to compensate for the large particle loss. In this scheme, small amounts of particles are injected at full energy alternating into each main ring and continuously with a design rate of $2 \times 25\,\text{Hz}$ on top of low charge circulating bunches. This is, however, a crucial process for maintaining low emittance beams since Liouvilles theorem (cfg. Section 2.1.1) forbids to inject the daughter bunch into the same phase space occupied by the stable circulating mother bunch. In order to decrease the separation, two distinct top-up injection schemes find application [34]. Both scheme require the same hardware configuration in form of two *kicker magnets* and a *septum magnet* as illustrated in Fig. 2.7. The kicker magnet consists of two dipole magnets with the ability to rapidly switch the path of the beam similar to a railroad switch. The septum magnet is a dipole magnet with the special property of creating a magnet field free region towards the circulating beam. This way the mother bunch is not influenced by the magnet field of the septum which is located in the close vicinity of the circulating beam.

In the *betatron injection* scheme as shown in Fig. 2.7 (left), the injected particles have the same energy as the stored beam. As a consequence, the trajectory of the daughter bunch does not fit to the mother bunch which results in betatron oscillations of the

2 The target was switched more than once during the SuperKEKB runtime since 2016.

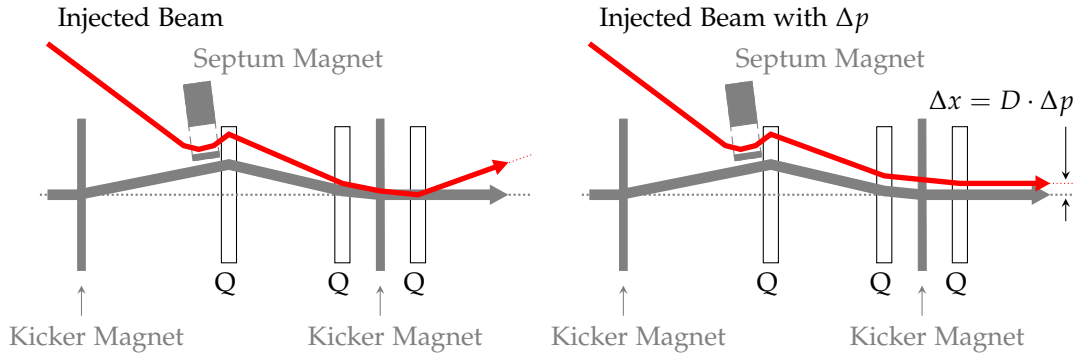

Figure 2.7: Schematic overview of two top-up injection schemes. *(left)* Injections with an orbit offset are referred to as *betatron injections*. *(right)* Injections with a momentum offset are called *synchrotron injections*. The objects marked with Q are focusing quadrupole magnets.

daughter bunch around the ideal orbit. These oscillations are constantly mitigated by radiation dampening until the injected daughter bunch merged into the phase space of the circulating mother bunch.

The *synchrotron injection* scheme is illustrated in Fig. 2.7 (right) and is mostly free of such betatron oscillations. In this scheme the daughter bunch is injected with a momentum difference with respect to the circulating beam. If the momentum difference is properly chosen, the transversal offset of the daughter bunch is converted to synchrotron oscillations. Here, the transversal offset Δx of the daughter bunch is defined by the dispersion D at the position of injection and the momentum offset Δp by

$$\Delta x = D \cdot \Delta p \ . \tag{2.14}$$

At SuperKEKB, synchrotron oscillations have a smaller amplitude than betatron oscillations and, therefore, cause less beam background. Similar to the betatron oscillations the synchrotron oscillations are damped by the radiation dampening effect. Nonetheless, the injection procedure causes a substantial particle background emerging from the RF bucket or mother bunch in which the daughter bunch was injected. The particle background, therefore, appears in a narrow time window of the by-passing bunch repeating each revolution.

2.4 BEAM BACKGROUND SOURCES

Circulating particles in a collider provoke undesired particles referred to as *beam background*. In general one can differentiate between three different sources of beam backgrounds. In the following the background sources are mentioned with their corresponding background types. More detailed explanations of each background type are listed afterwards.

1. *Beam induced backgrounds* are caused by circulating the beams in the collider. These type of background source includes *synchrotron radiation*, *beam gas scattering*, and *Touschek background*.

2. *Luminosity induced backgrounds* originate from particle collisions. The processes to these type of backgrounds are *radiative Bhabha scattering* and the *pair production via the two photon process*.

3. Other beam background sources are the *injection induced particle background* and the *huge beam loss events*.

Beam Induced Backgrounds

SYNCHROTRON RADIATION *Synchrotron radiation* is emitted by an electric charge propagating in a magnetic field which is transversally accelerated. In a e^+e^- synchrotron with a constant radius of curvature within the bending magnets, the energy loss in MeV per turn due to the synchrotron radiation is given by

$$W = 8.85 \cdot 10^{-5} \frac{E^4}{\rho} \,. \tag{2.15}$$

Here, the energy E is in the unit of GeV and the curvature ρ in km. As mentioned earlier in Section 2.1.5, the emission of synchrotron radiation is used for radiation dampening reducing the emittance of the beams. However, this process has the by-effect of emitting unwanted photons which disturb the measurement of collision events. The typical spectrum of synchrotron photons in the interaction region of SuperKEKB are in the range of a few to several tens of keV.

BEAM GAS SCATTERING *Beam gas scattering* appears when particles of the beam collide with residual gas particles in the beam pipe. It combines the two processes of bremsstrahlung and Coulomb scattering. Beam gas scattering changes the momenta of beam particles which then eventually hit the beam pipe, magnets, detectors or other hardware. The amount of background by beam gas scattering is proportional to the beam current and the dynamic vacuum pressure in the rings.

TOUSCHEK BACKGROUND The *Touschek* scattering is an intra-bunch process which changes the momenta of beam particles. As a consequence the beam particles possibly interact with the surrounding beam pipe, magnets, detectors or other hardware. This process is proportional to the beam current, number of bunches and inverse proportional to the beam size.

Luminosity Induced Backgrounds

RADIATIVE BHABHA SCATTERING The term *Bhabha scattering* refers to the elastic scattering of electrons and positron which dominates the e^+e^- cross section. The *radiative Bhabha scattering* process is always accompanied by radiative effects reducing the energy of the beam particles $e^+e^- \rightarrow e^+e^-\gamma$. This well understood process is proportional to the luminosity and is therefore used as the primary method for luminosity monitoring. The emitted photons propagate approximately parallel to the beam before they collide with collider or detector elements. Since for the majority of interactions the deflection angle is small, the scattered particles continue to propagate along the beam lines. In the case of low momentum changes the particles might be able to maintain a stable orbit. For sufficiently large momentum changes the particles interact with the beam pipe or magnets. Another background appears when emitted photons interact with the iron of the accelerator elements. This process results in a large number of low energetic gamma rays and neutrons via the giant resonance.

PAIR PRODUCTION VIA THE TWO PHOTON PROCESS Low momentum e^+e^- pairs are produced via the two photon process $e^+e^- \rightarrow e^+e^- + \gamma\gamma \rightarrow e^+e^-e^+e^-$. The magnet field induced by the Belle 2 solenoid makes these low momentum electrons and positron perform spiral movements and causing a large amount of hits in the detector.

Other Backgrounds

INJECTION INDUCED PARTICLE BACKROUND As introduced earlier, particles injected into the main rings undergo betatron and synchrotron oscillations with large amplitudes before they merge into the circulating mother bunch. Parts of the bunch interact with accelerator or detector hardware leading to particle showers. This type of background is bound to the bunch or bucket number in which the particles have been injected and therefore appear only once every turn at the IP. However, these extended oscillations lead to a significantly increased background rate at the IP.

HUGE BEAM LOSS EVENTS Another background source are huge beam loss events due to malfunctions of steering and final focussing magnets, bad collimator settings or other yet unknown reasons. Some of these events coincide with particle injections. At SuperKEKB, especially the LER is prone to such events. For example, from in total seven quenches of the final focussing magnets between April and June 2021 are six attributed to the LER. The consequences of such huge beam losses is exemplarily presented in Fig. 2.8. It shows a collimator damage due to the positron beam in the LER ring. These types of particle losses are especially undesired because of the serious

damage to the accelerator and detector hardware and the lost beam time due to the replacement work.

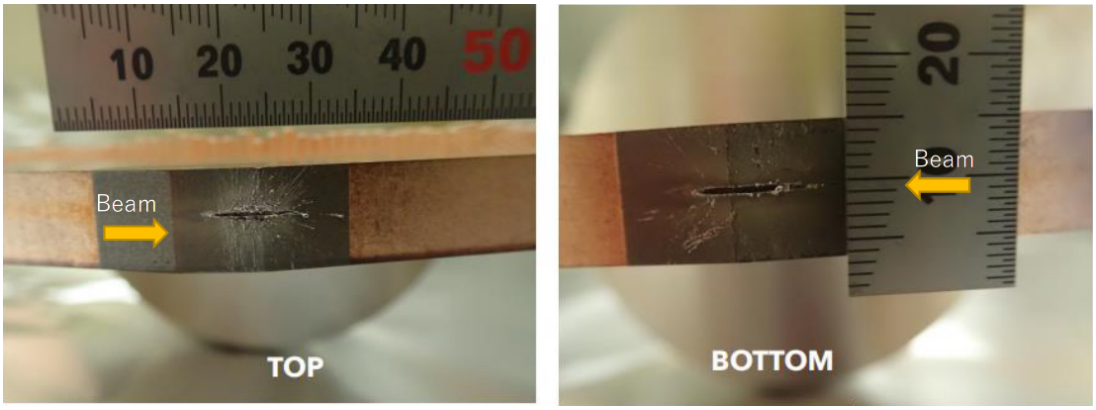

Figure 2.8: Photo of a damaged collimator after the huge beam loss event at June 6, 2021, in the LER. The replacement work took 3 to 4 days. Taken from [35].

3

THE BELLE II EXPERIMENT

The Belle 2 experiment is the only experiment at the SuperKEKB collider. It is located in the northern part of the collider rings in the Tsukuba area. Fig. 3.1 shows an illustration of the Belle 2 detector with its sub-detectors. Defined by the propagation direction of the high energetic e^-, the region of the incoming e^- beam is referred to as backward (BWD) and of the outgoing e^- beam as forward (FWD) region. The ambitious physics program demands a high performance of the Belle 2 detector. A small collision point in combination with a good vertexing performance with a spatial resolution of 50 µm or better ensures resolving the vertices of a B-meson decay, for example, for the measurement of the time dependent CP violation. In general, a good reconstruction efficiency of the momenta and tracks of charged particles over the full kinematic range is required. Thanks to the rather low center of mass energy the kinematic range stretches from 50 MeV up to 8 GeV. In order to identify the various decay modes of B-mesons a separation of pions, kaons, protons, electrons and muons demands an efficient particle identification system that performs well over the full energy range. In addition, the energy and direction information of photons requires an electromagnetic calorimeter. A fast and reliable trigger system sets another requirement to exploit the worlds highest instant luminosity. Following on that, of course, the data acquisition system should be capable of storing large quantities of data in short time intervals.

In the following, an overview of the various detector components is given starting from the sub-detector closest to the beryllium beam pipe in the center of Belle 2 with only 10 mm in diameter [16]. At the end the implications of the high particle background on the Belle 2 detector are illustrated.

- The first detector layer is occupied by the **vertex detector (VXD)** which consists of two layers of the *pixel detector (PXD)* [36] followed by four layers of the *silicon vertex detector (SVD)* [37].

  Eight PXD modules are located at radii of 14 mm and twelve modules at 22 mm around the beam pipe. The PXD uses the *depleted field effect transistor (DEPFET)* technology allowing to construct self-supporting 75 µm thick modules. Its eight megapixels are read out continuously every 20 µs. The SVD consists of four double-sided silicon strip layers at radii between 38 mm to 135 mm around the beam pipe. The detector provides a precise spatial resolution while having a low material budget. Together with the PXD both sensors are able to reconstruct low-p_t tracks down to a few tens of MeV/c.

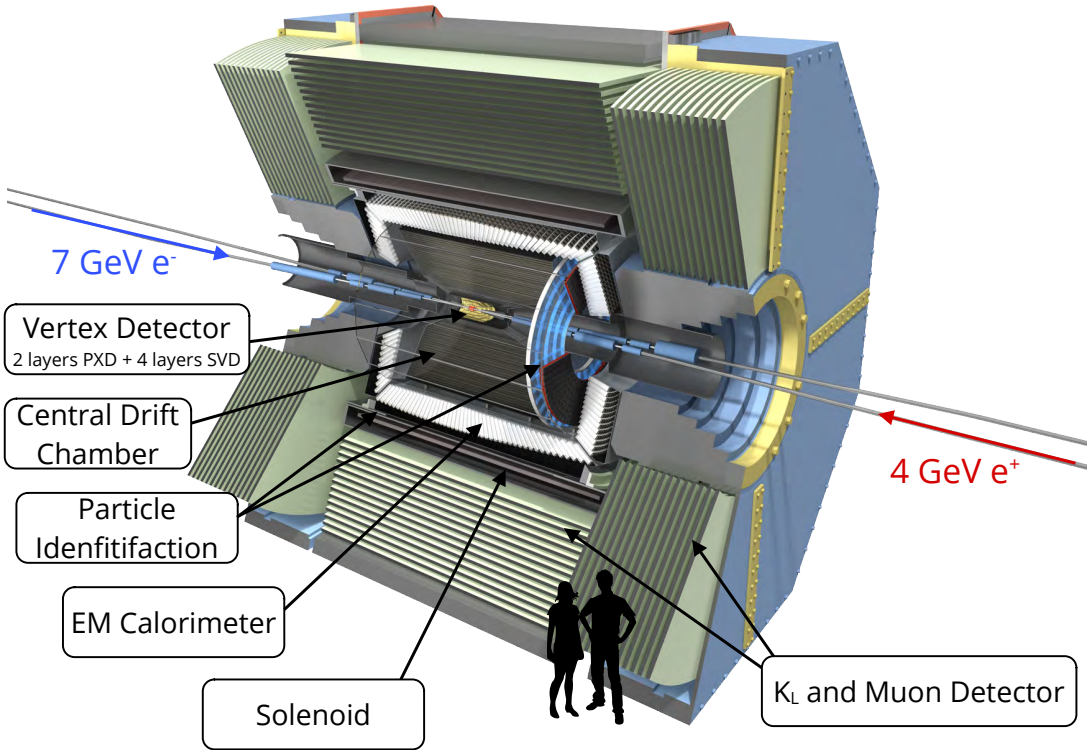

Figure 3.1: The Belle 2 detector. The sub-detector components are displayed correspondingly.

- The **central drift chamber (CDC)** [38] is a cylindrical volume equipped with 14 336 sense wires and 42 240 field wires organized alternatingly parallel to the beam pipe. The volume is filled with equal amounts of He and C_2H_6. The CDC has three important roles in the experiment: First, reconstructing charge tracks and measure precisely the momenta; second, identifying particles based on their energy loss in the gas volume, especially for low momentum particles which do not reach the outer particle identification device; third, serving as exclusive input for the *first level trigger*.

- The **particle identification (PID)** device discriminates in particular between kaons and pions and determines their velocity based on a measurement of the Cherenkov angle. There are two different systems installed on the barrel and forward endcap. In the barrel region a *time of propagation (TOP)* counter [39] consisting of long rectangular quartz bars right next to the CDC. The bars are read out by one photomultiplier tube at each end with a time resolution of around 25 ps. At the forward endcaps an *aerogel ring-imaging Cherenkov (ARICH)* detector [40] with an aerogel radiatior of 2 cm thickness determines the Cherenkov angles using dedicated photon sensors.

- The **electromagnetic calorimeter (ECL)** [41] determines the energy of charged and even neutral particles using a CsI(Tl) scintillating crystal as active material.

The main tasks of the calorimeter are the precise determination of the energy and angular coordinates, electron identification, K_L^0 detection with the following KLM, and an online luminosity measurement. The ECL is divided into a barrel, FWD and BWD region.

- The superconducting **solenoid magnet** provides a magnetic field of 1.5 T in a cylindrical volume of 3.4 m in diameter and 4.4 m in length. The magnetic field is parallel to the beam direction forcing charged particles travelling perpendicular to the magnetic field on a curved trajectory. The curvature of the particle is then used to determine its momentum.

- The **K_L-Muon (KLM)** [42, 43] detector is the outermost Belle 2 sub-detector and surrounds the solenoid magnet. It is designed in an alternating sandwich structure with 4.7 cm iron plates and active detector components. The iron plates serve as the magnetic flux return for the solenoid. Its main purpose is the detection of muons leaving the detector. In addition it detects hadronic showers created by K_L mesons which interact in the ECL or the iron plates.

In addition to the citation of the individual sub-detectors, a more detailed description of the Belle 2 detector is available in [16, 44].

IMPACT OF THE PARTICLE BACKGROUND In contrast to its predecessor, the Belle 2 detector has to cope with a factor of 50 higher physics event rate and a factor of 20 higher background rate. This has numerous implications for the sub-detectors. First of all, the substantial higher background level can cause high occupancies and pile-up events which result in read-out issues and a bad data quality. An accelerated detector aging due to radiation damage is, in addition, a side effect of the higher event and background rate. As of August 2021, such effects are already seen in the CDC as well as for the photo-multiplier tubes of the TOP. High intensity backgrounds emerging from huge beam loss events are one of the most serious background sources especially for the inner detectors. For example, as a result of a huge beam loss event on Mai 10, 2021, around 1 % of the PXD pixels are completely dead [45]. In addition, several read-out gates are instable or noisy which leads by other yet unknown effects to more noise [45]. The consequences of all huge beam loss events combined are the loss of a few percent of pixels [46]. In addition, the huge beam losses often cause noisy and inefficient regions which require time consuming adjustments of module parameters to recover stable conditions [46]. However, in terms of the physics performance, the damage is fortunately not significant yet [46].

However, there are counteractions applied by each detector system mitigating these effects. For example, the PXD as well as the SVD included the presumed background levels and event rates in their entirely new detector design. Other detectors such as the CDC or ECL, which mostly kept their Belle design, counteract the increased pile-up

noise with new and much faster read-out electronics. The increased backgrounds due to particle injections would lead to pile-up noise or a high occupancy in the sub-detectors. These effects are handled by interrupting the data taking of several Belle 2 sub-detectors for a narrow time frame around the by-passing injection bunch.

But not only the Belle 2 sub-detectors employ countermeasures to cope with beam background. The SuperKEKB accelerator applies several actions mitigating and preventing the beam backgrounds. This begins with the injection of low emittance electrons and positrons into the main rings. The positron damping ring is completely new designed and installed for SuperKEKB. Wiggler magnets in the Nikko and Oho sections of the main ring further decrease the emittance of the beam. This leads to less interactions of the beam with, for example, the surrounding beam pipe or other beam instrumentation since the beam size is proportional to the square root of the emittance. Multiple horizontal and vertical collimators along the main rings cut off the tails and therefore the off-track particles. Dedicated heavy-metal shields are installed inside the VXD volume in order to keep secondary shower particles from reaching the detectors. Furthermore, the beryllium beam pipe in the interaction area has a gold coated inner surface in order to absorb synchrotron radiation.

The importance of background detectors increased in the first years of SuperKEKB operation since the background levels observed by the Belle 2 detectors are higher than expected. This leads to the fact that the planned luminosity goal as stated in the Belle 2 technical design report [16] cannot be achieved anymore and has been reduced [20]. The detector systems and analyses presented in this thesis belong to a collaboration wide effort to understand beam backgrounds as good and as fast as possible.

4

BEAST - THE SUPERKEKB COMMISSIONING CAMPAIGN

Around six years after the shutdown of KEKB, the major upgrade to SuperKEKB reached a first milestone by circulating particles for the first time. The first storage was achieved with positrons in the LER on February 10, 2016 and six days later in the HER [47]. At that time, there was no final focussing system installed, no Belle 2 detector on the beam line and the positron damping ring was not ready to use. Nevertheless, a suite of dedicated background detectors, collectively referred to as the BEAST detectors, observed the background behavior in each of the three SuperKEKB commissioning phases. The goal of the commissioning phases is to ensure a safe operation of the Belle 2 detector. A successful operation of Belle 2 and SuperKEKB depends critically on limiting and mitigating the different beam backgrounds introduced in Section 2.4. For each phase the BEAST experiment consisted of a different set of detectors. In the following each of the three commissioning phases is introduced.

4.1 PHASE 1

The first phase of the SuperKEKB commissioning took place from February until June 2016. The experimental setup is explained in the introduction of this chapter. At this stage, the goal for the SuperKEKB collider was mainly vacuum scrubbing before the Belle 2 roll-in in the second phase, carry out basic machine studies such as low emittance optimization of the beam optics and tuning of the system feedback. The goals for the BEAST detectors was mainly getting a first impression on the background levels at the interaction region, improving the background simulations and making the detector prototypes ready for the later following phases.

In this phase, a set of eight detector systems was mounted on a metal support structure in the interaction region. A total of 64 PIN diodes measured the instantaneous dose rate at multiple positions. The Diamond system placed four diamond sensors in the close vicinity of the IP for a fast dose rate measurement. This system was the prototype of the beam abort system which is currently in place. The Crystal system placed in total 18 CsI(Tl), CSI, and LYSO crystals measuring the electromagnetic energy spectrum and the injection induced backgrounds. Eight BGO crystals observed the electromagnetic dose rate. The first version of the CLAWS system used eight detectors based on plastic scintillator tiles with silicon photomultiplier read-out observing the injection induced beam background over extended times and with a sub-nanosecond sampling rate. A set of four ^{3}He tubes collected data about the thermal neutron rate while four TPC detectors measured the fast neutron flux. The

QCSS system used four detectors based on plastic scintillators in order to observe charged particles.

A comprehensive paper of the Phase 1 detectors, procedures and results is given in [48]. Results and procedures with more focus on CLAWS in this phase is available in [49–51].

4.2 PHASE 2

The second phase of the SuperKEKB commissioning took place from February till end of July 2018. In this phase, the final focussing system was in place and the LER damping ring was operational. The Belle 2 detector was in place, but with a modified inner vertex detector. Due to the close vicinity to the IP, the PXD and SVD detectors are exposed to the highest particle rates. For this reason, the inner vertex volume was equipped with a set of dedicated detectors measuring the beam background.

For the SuperKEKB collider, the major goal for this phase was to confirm the safe environment for the VXD and the first collision of particles up to a target luminosity of $1 \cdot 10^{34}\,\mathrm{cm}^{-2}\,\mathrm{s}^{-1}$. From the Belle 2 point of view, an improvement and understanding of the different beam background sources with simulations and studies were the goals for this phase.

Fig. 4.1 depicts a CAD drawing of the Phase 2 BEAST detector. From the original Belle 2 detectors two PXD ladders and four layers of SVD detectors are placed in horizontal direction at the outer side of the two main rings. A former Atlas pixel detector FE-I4 [52] is sensitive to charged tracks and low energetic X-rays of around 10 keV and is referred to as the Fangs detector [53]. Three Fangs staves are placed at the first PXD layer at 90°, 180° and 270° in ϕ. The CLAWS detector principle is the same as in Phase 1, but the detector geometry changed to a ladder format with eight scintillating tiles in a row. Two ladders are placed at the second PXD layer at angles of 135° and 225° in ϕ. The CLAWS detector in Phase 2 system is one main subject of this thesis and presented in detail in Section 5.3.1. Two ultra-light double-sided ladders equipped with CMOS pixel sensors referred to as Plume detector [54] are placed in the second PXD layer at 125° and 225° in ϕ. One detector is additionally tilted at an angle of 18° in θ. Its around $8 \cdot 10^6$ pixels have been operated at a low detection threshold enabling a sensitivity to electrons with energies greater than 40 keV and X-rays in the range of 2 keV to 10 keV. One ^{3}He detector and eight TPC detectors [55] mostly as used in Phase 1 measure neutrons and are located outside of the VXD volume at the dock box area close to the ARICH detector at various angles.

As writing this, a comprehensive paper describing the detector setups, study procedures and results of the second commissioning phase is currently in the final stage of publishing. Results from individual detector systems are available for the Plume detector [57], the background simulation [58], and the CLAWS system in Part iii.

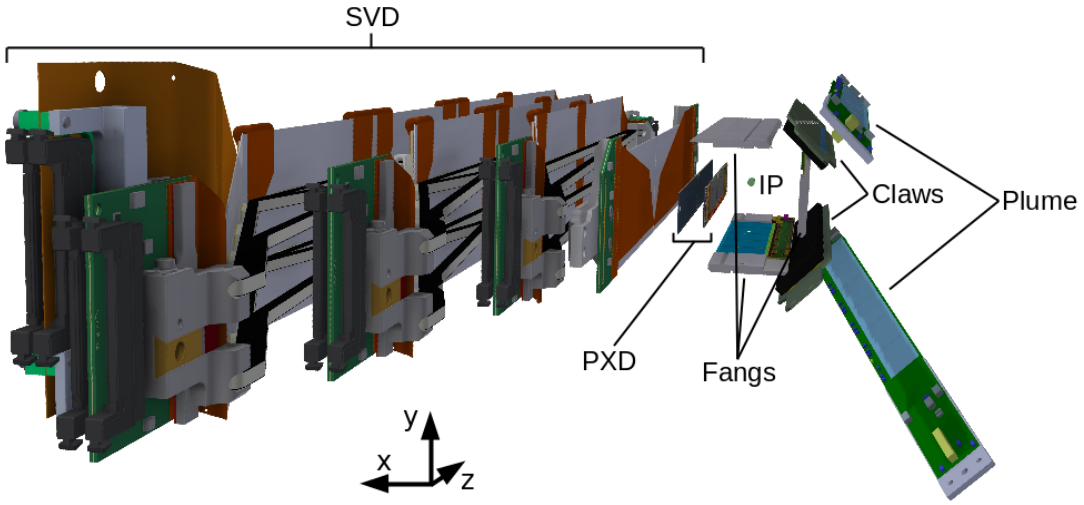

Figure 4.1: BEAST Phase 2 CAD with the sub-detectors. Taken from [56] and modified.

4.3 PHASE 3

The third and final commissioning phase of the SuperKEKB collider began in the spring of 2019 and continues until 2025. The Belle 2 detector is complete with exception of the PXD which has only 2 out of 12 outer ladders in place. Installing a full second PXD layer is forseen for the long summer shutdown in 2022.

The goals of this phase are various. One of the major goals is to increase the instantaneous luminosity to its design value of $6 \cdot 10^{35}\,\mathrm{cm}^{-2}\,\mathrm{s}^{-1}$. This will be reached by squeezing of the beams at the IP down to the design parameters and the increase of the beam currents in each main ring. However, increasing the beam currents is limited due to the high beam backgrounds. A continuous mitigation of the backgrounds with dedicated recurring beam studies are done tackling the high background conditions.

In Phase 3, most of the background detectors have been removed. Only three background detectors continued operation at new locations. Both neutron detectors ^{3}He and TPC moved at the walls of the massive concrete blocks shielding the ionizing radiation emerging from the interaction region. The CLAWS system changed again the detector geometry and consists of in total 32 detectors mounted at the final focussing magnets. CLAWS continues observing the injection induced particle backgrounds. More detailed information about CLAWS in Phase 3 follows in Section 5.3.2.

Part II

THE CLAWS SYSTEM

This part provides, first, detailed information about the detector hardware of the Claws system in Chapter 5 and gives, second, a comprehensive overview of the developed data acquisition system in Chapter 6.

Chapter 5 begins with a brief history of the Claws detector in Section 5.1. Afterwards, an introduction into the detector concept of Claws and its functional principal is given in Section 5.2. The different experimental setups of the Phases 2 and 3 of the SuperKEKB commissioning are presented one section later in Section 5.3. While the Phase 2 detector design was mostly developed by my former colleague Dr. Miroslav Gabriel, I was the leading developer of the detector design and technology for Phase 3 in the scope of this thesis. The following two sections give first a detailed understanding of the raw data the Claws system produces (Section 5.4) before the calibration procedure of the Phase 3 detectors (Section 5.5) is presented.

Chapter 6 gives a comprehensive understanding of the data acquisition system used in the Phases 2 and 3 which was developed in the scope of this thesis. The real-time analysis and the created online monitors are presented in Section 6.2 and Section 6.3 before the capabilities of the system is benchmarked in Section 6.4.

5

DETECTOR HARDWARE

The Claws system was born with the beginning of the SuperKEKB commissioning in 2016. Claws is designed to observe the beam background with special focus on the injection induced background. Its general detector principle of a scintillating tile with silicon photomultiplier (SiPM) readout is inherited from the CALICE-T3B experiment [59, 60] and is presented in Section 5.2. This technique coupled with an oscilloscope with a large internal memory enables recording continuous waveforms at a high sampling rate for multiple milliseconds - making it perfectly suited for the observation of injection bunches in an e^+e^- collider.

This hardware section starts with a brief overview about the evolution of Claws since 2016 and is followed by introducing the general detector concept which is equal for all of its versions. After that, a detailed description of two distinct Claws systems operating in the Phases 2 and 3 of the SuperKEKB commissioning is presented with its full read-out chain. In the last two sections of this chapter, the reader is invited to get an understanding of the raw signals, its uncertainties and other difficulties before the calibration of the Phase 3 modules is presented.

5.1 A BRIEF HISTORY OF CLAWS

On February 10, 2016, the first Claws system observed the very first turns of positrons in the interaction region of the SuperKEKB collider which was nicely featured in an article of the *CERN Courier* [61]. Over the following six month, Claws and the other Beast detectors studied the beams. The results of their studies improved the background conditions substantially and ensured a safe Belle 2 roll-in and beam operation in 2017. This first phase of the SuperKEKB commissioning resulted in one PhD thesis, a master's thesis, and a comprehensive paper [48–50].

Two years later, in March 2018, a second version of the Claws system was installed inside the Belle 2 detector, only a few centimeters away from the IP. Its geometry changed from a single channel module to an eight channel ladder format, fitting into the second layer PXD scaffold. In addition, the newly introduced high and low gain modes increased the sensitivity for low intensity conditions while being able to run in high intensity conditions. Another major innovation in Phase 2 is the new DAQ software. Its advanced design offers much greater performance in comparison to the Phase 1 DAQ software. The calibration and parts of the installation process is documented in a master's thesis [62]. A combined Phase 2 paper from the Beast community is expected to be published at the end of this year. The detector design

and innovations are discussed in Section 5.3.1and descriptive information of the DAQ software follows in Chapter 6.

In early 2019, the beginning of the third phase of SuperKEKB commissioning, CLAWS became a permanent beam monitoring system. The location was switched from the inner VXD volume to the final focusing magnets. In total, 32 sensors are placed at different angles and distances to the IP. The locations in forward and backward direction allow observing high intensity injection bunches. Its geometry was changed back to a similar design as the Phase 1 modules with one channel per module. In addition, one Ethernet socket on each module greatly simplifies the installation and cable routing. All signals and supply voltages are transported from and to the DAQ using one Ethernet cable only. The DAQ software did not change with respect to Phase 2. The detector and its new features are discussed in Section 5.3.2 and its calibration follows in Section 5.5.

In Autumn 2019, the injection background was mitigated down to a level where CLAWS is not sensitive anymore. However, in December 2020, the detector hardware got a second life as beam abort system. First tests showed CLAWS capability of detecting beam turbulences substantially earlier than the currently existing ones. This project is continued by a master student. More detailed information is presented in Section 9.3.

5.2 GENERAL DETECTOR CONCEPT

Throughout all Phases, the general detector concept of CLAWS did not change. This section gives first an overview of the general detector parts and later focuses on the main detector component: the silicon photomultiplier.

OVERVIEW One CLAWS channel uses an organic scintillator tile as active material as shown on the left in Fig. 5.1. The scintillator materials used are almost exclusively sensitive to charged particles. A centered dimple in the thin quadratic shaped plastic tile houses a SiPM, eventually detecting photons emitted by the tile. The scintillator shape is taken from the CALICE hadron calorimeter [63]. Additional wrapping of the tile in reflective foil (not shown in Fig. 5.1) increases the amount of photons detected by the SiPM. Both tile and SiPM are mounted together with additional electronics for amplification and signal transmission on a custom made printed circuit board (PCB). Additional wrapping of the active components in light shielding materials can be optionally added.

SILICON PHOTOMULTIPLIER A SiPM is a two dimensional array consisting of 100 to several 1000 small *avalanche photo diodes* (APDs) connected in parallel. The single

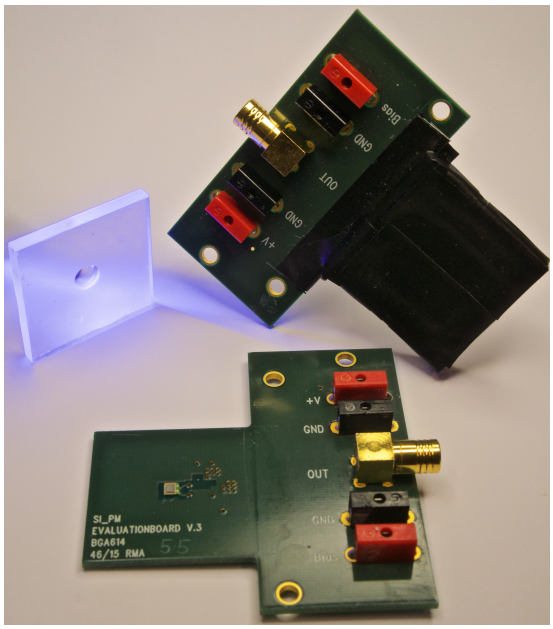

Figure 5.1: Phase 1 detector module at two different assembly stages. On the left, a scintillating tile shined on with UV light emphasizing its scintillating capabilities. On the bottom, the SiPM is visible in the middle of the quadratic shaped part on the left. In the back, a light tight wrapped Phase 1 module is presented.

APDs can be observed under a microscope as shown in Fig. 5.2 (left). A single APD is also referred to as a pixel.

An APD is a pn-junction with a bias voltage V_{bias} applied in reverse direction creating an electric field which leaves the p-side fully depleted. A SiPM can operate in two modes depending on the value of V_{bias}. For a bias voltage below the device specific breakdown voltage $V_{\text{bias}} < V_{\text{bd}}$ the APD operates in *proportional mode*, where the signal is proportional to the energy of the incoming photon. If $V_{\text{bias}} > V_{\text{bd}}$, an incident photon may trigger an avalanche. As this behavior is similar to a Geiger-Müller counter, this mode is called *Geiger mode*.

Fig. 5.2 (middle) illustrates the equivalent circuit diagram of an APD in Geiger mode. Once an electron-hole pair is generated the conceptional switch closes and the capacitance C_{d} begins to discharge through the series resistance R_{s}. The value of R_{s} is diminished by the avalanching carrier production and provides for a surge in the current flow while the potential difference across C_{d} (V_{d}) decays exponentially towards the break down voltage V_{bd}. Based on the circuit diagram, the current at C_{d} is described by

$$I_{\text{d}} = \frac{V_{\text{d}} - V_{\text{bd}}}{R_{\text{s}}} + \frac{V_{\text{bias}} - V_{\text{d}}}{R_{\text{q}}} \tag{5.1}$$

where the first term signifies the discharge and the second the recharge of C_{d}. With a large R_{q} of $\mathcal{O}(10\,\text{M}\Omega)$ the current flow from V_{bias} cannot sustain the discharge over R_{s}. Once the discharge of C_{d} is exhausted and reaches its trough, the avalanche

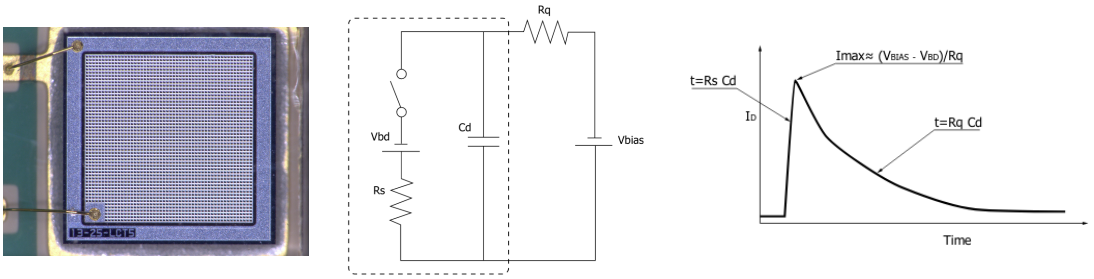

Figure 5.2: SiPM - Closeup and working principle. Different zoom factors of a SiPM. *(left)* Enlarged picture of a Hamamatsu MPPC S13360-1325PE with 25 µm pixel pitch. The active area of the SiPM has the dimensions of $1.3 \times 1.3\,\mathrm{mm}^2$ with 2668 pixels. Photo taken with a microscope at MPP. *(middle)* Equivalent circuit of a Geiger mode APD. Taken from [64]. *(right)* Conceptual output pulse of the circuit. Taken from [64].

process is quenched, the conceptual switch opens, and the recovery process of the APD begins. The recharge current flows through R_q and increases the voltage across C_d up to $(V_\mathrm{bias} - V_\mathrm{bd})$. During this recovery process, any excitation of the APD would result in a small amplitude output.

The signal generated by this process is depicted in Fig. 5.2 (right). Its rise time is defined by the discharge of C_d and is equal to $R_\mathrm{s} \cdot C_\mathrm{d}$ while the recovery time is given by $R_\mathrm{q} \cdot C_\mathrm{d}$. The signal's amplitude is adjusted by V_bias and peaks at $(V_\mathrm{bias} - V_\mathrm{bd})/R_\mathrm{q}$. The area under the signal is defined as the *gain* and quantifies the amount of charge generated by the excitation of one pixel. It is calculated with

$$G = \frac{C_\mathrm{d}\,(V_\mathrm{bias} - V_\mathrm{bd})}{q} \tag{5.2}$$

where q is the elementary electron charge. By design, the single pixels in a SiPM have approximately the same gain. Usual gain values are around 10^5 to 10^6 [65]. For this reason, the signal generated by the detection of one photon is constant for a constant bias voltage and called *photon equivalent* (p.e.). If more than one pixel gets excited, the signal's integral rises in integer increments of the 1 p.e. signal integral.

As many electric devices, a SiPM suffers from unwanted side effects, namely *noise*. The most important ones are *thermal dark noise*, *afterpulsing*, and *crosstalk*:

- **Thermal dark noise** describes the generation of electron hole pairs by thermal excitation which subsequently causes an avalanche. This noise rate scales exponentially with the temperature. Typical dark noise rates of state-of-the-art SiPMs are of several tens of kHz.

- **Afterpulsing** names an effect caused by trapped charge carriers in an APD triggering a second avalanche after a previous just terminated excitation. This effect can be observed as delayed signals which is not always easy to spot with decreasing afterpulsing rates in recent SiPM generations.

- **Crosstalk** is known as the effect of a photon produced in the recombination of a carrier pair triggering an avalanche in a neighboring pixel.

Further characteristic properties of SiPMs are *quantum efficiency*, *breakdown efficiency*, and *photon detection efficiency (PDE)*, :

The *quantum efficiency* is the probability of the creation of an electron hole pair by a photon. The *breakdown efficiency* is the chance of a carrier pair triggering an avalanche. The product of both yields the *PDE* which is the ratio of the number of detected photons divided by the number of photons that traversed the SiPM as a function of V_{bias} and the wavelength of the impinging photon. Typical values can go up to 50 % for certain wavelengths [66]. More detailed information of the underlying processes can be found in [65] and [66].

5.3 EXPERIMENTAL SETUPS

The detectors in Phase 2 and 3 faced different requirements which lead to two distinct detector layouts precisely fitting the preconditions of each Phase. However, the general CLAWS detector concept is the same throughout all three commissioning phases of the SuperKEKB collider. The geometric form factor as well as the setup location and parts of the readout electronics such as amplifiers, signal transport, and dock box designs may differ. This section gives a detailed overview over the different detector components and the experimental setups in the Phases 2 and 3 of the SuperKEKB commissioning.

5.3.1 *Phase 2*

During Phase 2, strict requirements on the available space and geometry of the detector and its cabling implicate restrictions concerning power consumption, cooling, signal transmission, and more. Furthermore, due to its vicinity of 22 mm to the IP, every component has to sustain a high level of radiation. This section describes the essential components of CLAWS in Phase 2. A detailed description of the assembly and calibration process can be found in [62].

DETECTOR In order to optimally use the available space of a second layer PXD module, a self-supporting ladder design was chosen. One CLAWS ladder measures $25.15 \times 2.50\,\text{cm}^2$ and consists of eight BC-408 [68] scintillator tiles of size $2.0 \times 2.0 \times 0.3\,\text{cm}^3$. Each tile is wrapped in *3M Day lighting Film DF2000MA* reflective foil [69] and is individually read out by a *Hamamatsu 13360-1325PE* SiPM [64] surface mounted on a PCB. The SiPM has an active area of $1.3 \times 1.3\,\text{mm}^2$ with 2668 pixels. The plastic tiles are fixed to the PCB using radiation hard Araldite and Kapton tape. Further packaging, for example for preventing ambient light disturbing the measurement, is

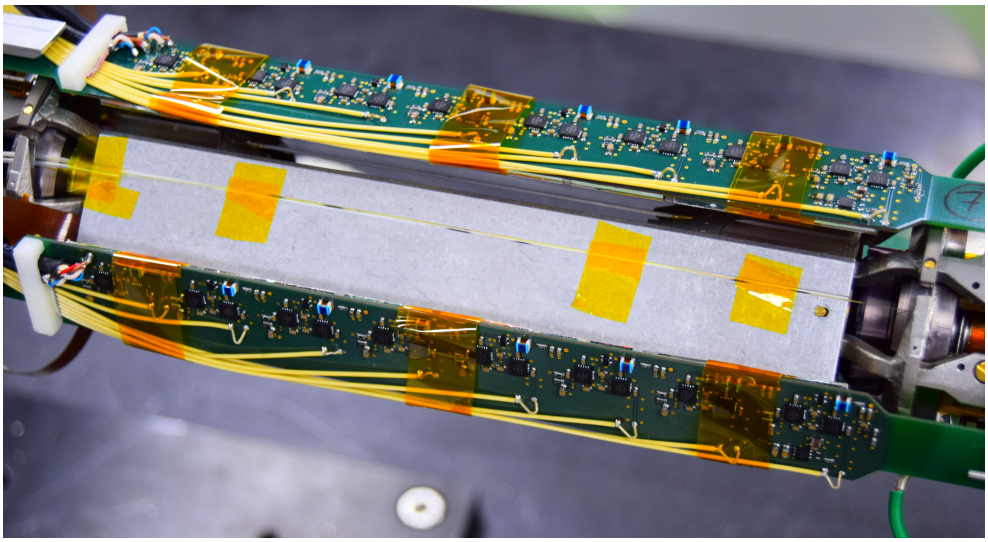

Figure 5.3: Phase 2 detector assembly on the vertex scaffold. The back of two CLAWS ladders are shown on the Phase 2 vertex detector. The yellow cables transport the analog signal generated by the SiPMs towards the DAQ system. The visible Kapton tape is part of a supporting structure keeping the scintillator tiles in position. Between the two CLAWS ladders, one Fangs stave (see Chapter 4) is shown. Taken from [67].

not needed. The installed detector is located in the center of Belle 2 and surrounded by several detectors, cables and cooling structure suppressing the arrival of ambient light at the sensors. One eight channel CLAWS detector is referred to as CLAWS ladder.

Except for the SiPMs, all of the on-board read-out electronics are located on the back of the PCB. Fig. 5.3 shows the back of two CLAWS ladders mounted on the scaffold. Each channel on the same ladder has its own full read-out electronics chain which is depicted in Fig. 5.4. Right after the SiPM, a dedicated switchable amplifier scheme enables a high and a low gain operation mode. In high gain mode, $V_{\text{preamp}} = 5\,\text{V}$ powers the inverting pre-amplifier and the switches which closes the upper circuit. The amplifier increases the signals by 19 dB or factor 8.9. In the low gain state, $V_{\text{preamp}} = 0\,\text{V}$ changes the state of the switches guiding the signal without amplification to the dock box. Switching between the two states is not supported for single channels. All eight channels on a ladder are switched at once.

Each ladder has a soldered connection to eight signal and two power lines. One power line supplies all SiPMs with the same bias voltage of around 57.5 V. The other power line serves all pre-amplifiers with 5 V when running in high gain mode. In low gain mode, no power is applied. The two gain modes enable a high sensitivity in low intensity conditions while also enabling measurements in high background conditions.

DOCK BOX AND READOUT SYSTEM The dock box is located in the general Belle 2 dock box space in around 1.5 m distance to the IP and is shown in Fig. 5.5 (left). It measures $23.6 \times 19.3 \times 5\,\text{cm}^3$. For each channel, it houses a *Mini-Circuits ZFL-500+*

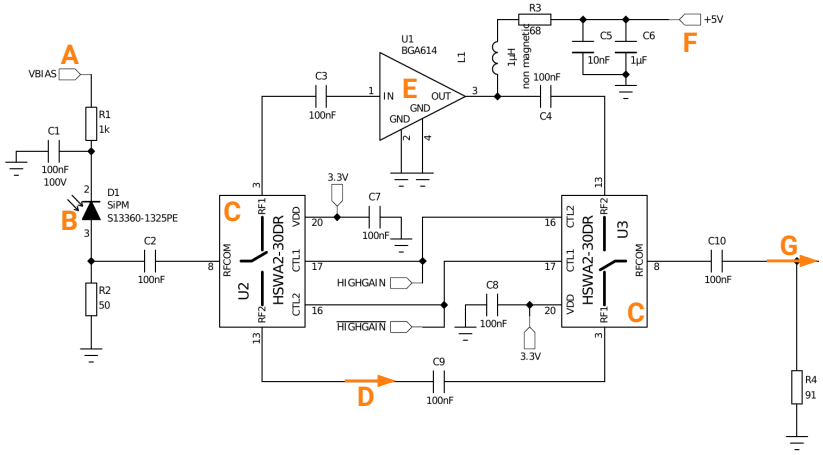

Figure 5.4: Phase 2 high & low gain mode circuit diagram. The most important parts are labeled with orange letters. The Hamamatsu SiPM S13360-1325PE *(B)* is supplied with a bias voltage $V_{\text{bias}} \approx 57\,\text{V}$ *(A)*. If the pre-amplifier supply voltage $V_{\text{preamp}} = 5\,\text{V}$ *(F)* is available, the RF switches *(C)* by Mini Circuits [70] close the top circuit including the Infineon BGA614 amplifier *(E)* [71] increasing the signal by a factor 8.9. In case there is no voltage applied at *(F)*, the signal bypasses the amplifier by using path *(D)* and is transmitted to the next amplifying stage in the dock box at *(G)*.

amplifier [72] of 20 dB, increasing the signal's amplitude before its transmission over a distance of 35 m to the DAQ system in the electronics hut. The dock box also serves as a patch panel distributing the power lines to the right Claws ladder and component. The bottom plate of the Claws dock box space is actively cooled by the SVD water cooling system. Tight space requirements in the dock box area made the design and construction of the dock box a challenging task. In total, the dock box has 41 jacks: 32 SMA connectors for signal in/out on coaxial cable, 3× 16-contact Lemo connectors as power input, 2× 5-contact Lemo connectors as power input, 4× 2-contact Lemo connectors providing power for the SiPMs and pre-amplifiers on each ladder. The 5 input power lines increase the cross section and minimize the total power loss over the 35 m cable path between dock box and electronics hut.

A star-like grounding scheme avoids grounding loops. Among all cables coming from the electronics hut and arriving at the dock box only one power cable's ground is connected to the dock box. All other grounds are isolated with respect to the dock box. In addition, only one ground out of the three cables connected to each Claws ladder is connected. All hardware parts match an impedance of 50 MΩ.

The remaining readout system is located in the electronics hut right next to the Belle 2 detector. Fig. A.1 (left) in Appendix A shows all of the read out components mounted in a rack. The power cables arrive at the top of the rack and connect to the patch panel which distributes the three voltages for SiPM, amplifier, and pre-amplifier provided by the modular *Keysight N6700* power supply. Four *PicoScope 6404D* digitize the analog signals with 8 bit and a sampling rate of 1.25 GHz per

channel. Its ultra deep 2 GSample buffer allows recording up to 400 ms per channel which corresponds to 40 000 particle revolutions in one single waveform. The input ranges reach from 50 mV to 2 V in 7 nonlinear steps. All oscilloscopes and the power supply are externally steerable and connected to the rack mountable *Fujitsu Celsius C740* work station via USB and Ethernet. The custom made DAQ software written in C++ steers the power supply and oscilloscopes. More details about the DAQ software including the fast reconstruction and online monitors is given in Chapter 6.

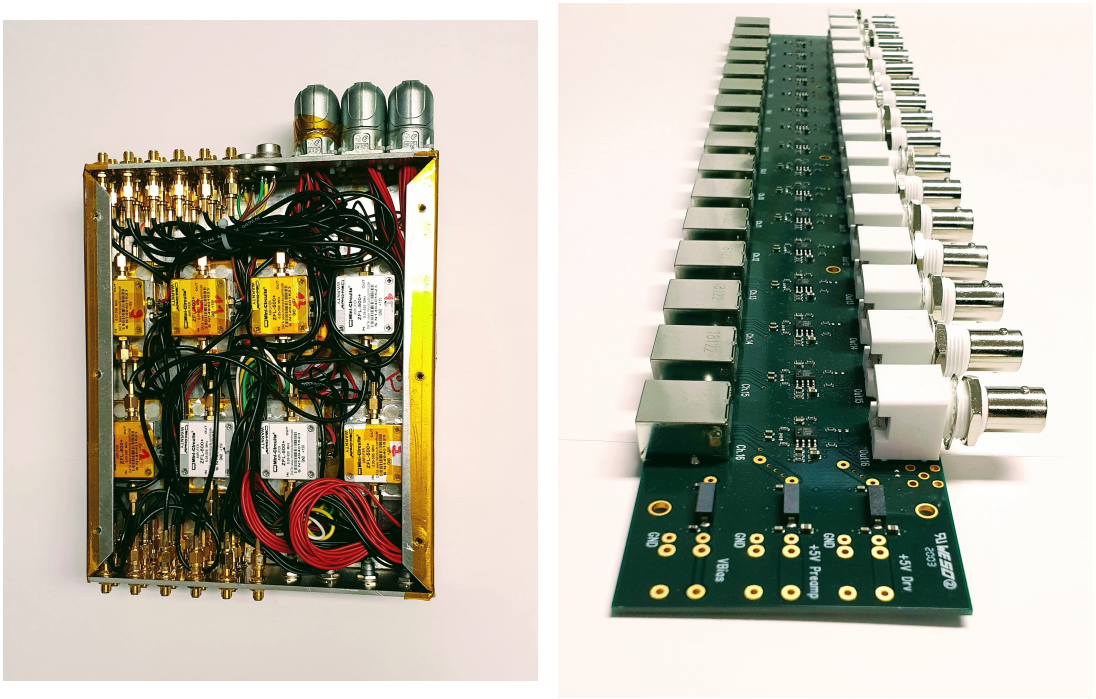

Figure 5.5: Phase 2 dock box and Phase 3 receiver board. *(left)* The dock box is equipped with one 20 dB amplifier per channel and works as a patch panel distributing the power to the correct destination, e.g. amplifier, SiPM or pre-amplifier. *(right)* Phase 3 receiver board with 16 channels. The Ethernet connections to the modules are on the left and the BNC signal outputs are on the right. Differential amplifiers back-transforming the differential signal are between Ethernet and BNC connector.

5.3.2 *Phase 3*

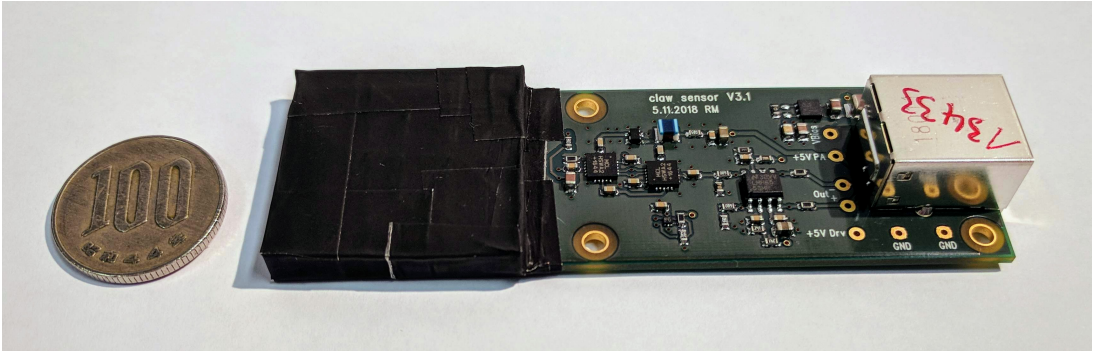

Figure 5.6: Phase 3 detector module in size comparison to a ¥100 coin. The black part on the left of the module is the active detector part: A scintillating tile on top of a SiPM is first covered in reflective foil and second generously wrapped in multiple layers of adhesive black aluminum foil shielding ambient light. The Ethernet plug on the right connects to the DAQ.

In the third phase of the SuperKEKB commissioning, the construction work on the Belle 2 detector and the SuperKEKB accelerator facility is complete. The circulating beams are understood well enough to allow operating the highly sensitive inner vertex sensors in a safe environment. For this reason, the space used by the CLAWS ladders in Phase 2 is occupied with the design vertex detectors.

The great success in Phase 2 lead to the continuation of CLAWS as a permanent SuperKEKB beam background monitor. Its location was changed onto the final focusing quadrupoles. Heavy metal of these magnets and other detectors block the direct view on the beam. Nevertheless, since CLAWS is designed observing the particularly large signals coming from injection bunches, the new location was not expected to inhibit its usage. In the following, the new detector design and the overall setup is presented.

DETECTOR One CLAWS channel as shown in Fig. 5.6 has the size of $3 \times 10.5\,\mathrm{cm}^2$ and is referred to as one CLAWS module. The scintillator tile is of size $3 \times 3 \times 0.3\,\mathrm{cm}^3$ and is made of POPOP doped polystyrene as used in the NA62 experiment [73]. As in Phase 2, the SiPM is located under a dome in the middle of the tile. The switchable pre-amplifier scheme close to the SiPM is the same as used in Phase 2. In the next stage, the signal is again amplified by a newly introduced differential amplifier increasing the signal by 12 dB. It additionally transforms the signal from a single-ended to a differential one. The corresponding circuit diagram is shown in Fig. 5.7. Thanks to this transformation, the signal can be transmitted using an off-the-shelf CAT 6A (or higher) Ethernet cable. The remaining three twisted pair wires of the Ethernet cable are used to deliver power for the SiPM, the pre-amplifier and the differential amplifier as depicted in Fig. 5.7 *(E)*.

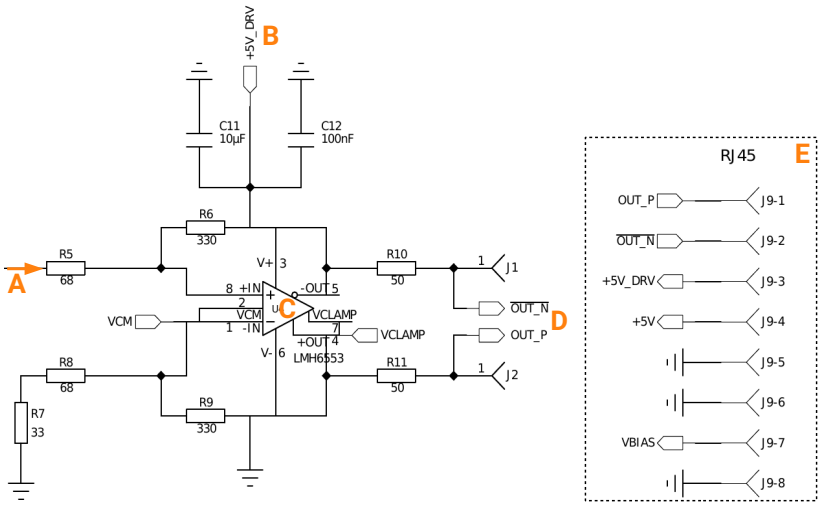

Figure 5.7: Phase 3 differential amplification circuit diagram. The most important parts are labeled with bold orange letters. The signal arrives from the switchable pre-amplifier scheme as depicted in Fig. 5.4 at *(A)*. The driver voltage $V_{\text{diff}} = 5\,\text{V}$ *(B)* is always turned on and powers the *LMH6553 Differential Amplifier (C)* by Texas Instruments [74]. The differential signal pair *(D)* is transmitted over the Ethernet cable to the electronics hut. *(E)* shows the wire layout of the Ethernet cable. From top to bottom in pairs of two: differential signal, two voltages of 5 V for the differential amplifier and the pre-amplifier, ground wires for the previous mentioned voltages, the SiPM voltage V_{bias} and its ground.

Fig. 5.8 shows the new detector locations on the final focusing magnets. Placed in their new positions, the modules are exposed to ambient light. For this reason, the active components of the Phase 3 modules are additionally wrapped in up to three layers of black adhesive aluminum foil shielding ambient light as shown in Fig. 5.6.

DOCK BOX AND READOUT SYSTEM Using the differential amplification scheme simplified the installation work substantially since there is only one cable per CLAWS module. In addition, it allows omitting active dock box components since all of the amplification is done on the module itself and the power distribution is done in the electronics hut. The Phase 3 dock box is a simple patch panel with 16 Ethernet bridges. One on each side of Belle 2, FWD and BWD. The cable length from each CLAWS module to the respective patch panel is 5 m. For the remaining distance to the CLAWS rack in the electronics hut a 35 m Ethernet cable is used. The patch panels allow easier handling of the cables during installation, modification, and maintenance of the CLAWS modules.

The readout hardware located in the electronics hut is duplicated with respect to Phase 2. Two independent DAQ systems steer the FWD and BWD modules, respectively. In total, two Fujitsu Celsius C740 workstations steer two Keysight N6700 power supplies and eight PicoScope 6404D oscilloscopes. One *16 channel receiver board* per readout system unwinds the twisted pair layouts. In addition, it back-transforms the signal from a differential to a single-ended using the reverse implementation of

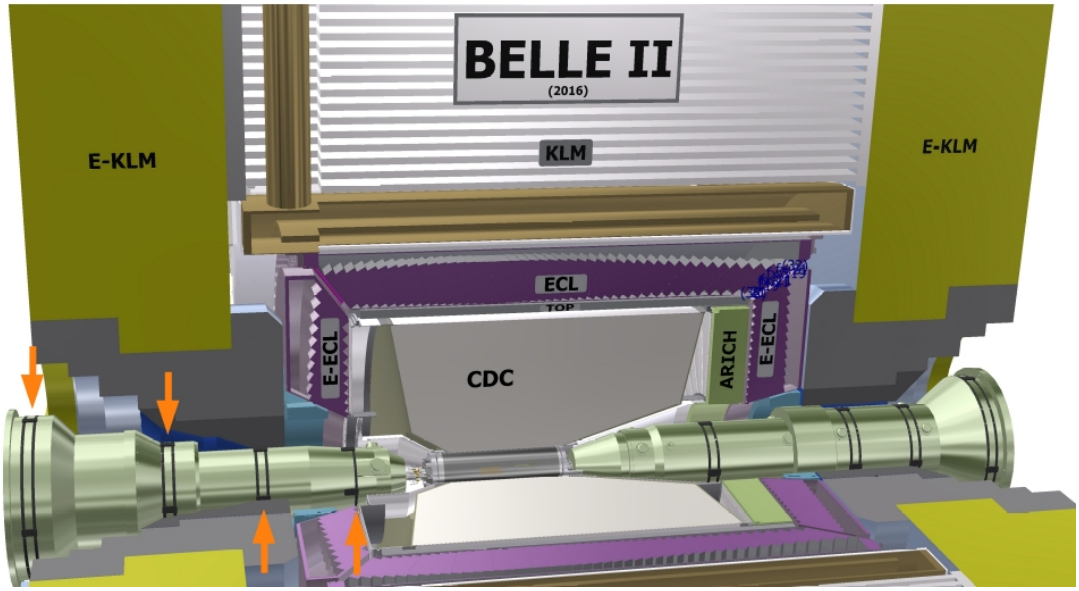

Figure 5.8: Phase 3 detector locations on the final focusing magnets inside of the Belle 2 detector. 16 CLAWS Phase 3 modules are located in four different positions along the beam direction and four different angles on each of the magnets. The locations are exemplarily marked on the backward magnet. The modules are fixed using two black straps at each z location.

the differential amplification scheme as described earlier. The back-transformation amplifies the signal a second time by 12 dB. A picture of a 16 channel receiver board prototype is presented in Fig. 5.5 (right).

Appendix A shows photos of the DAQ hardware in Phase 2 and 3 in Fig. A.1, a photo of the Phase 3 modules on the BWD final focusing magnet and the installed Phase 3 dock box in Fig. A.2. In addition, Table A.1 lists the detector differences in the Phases 2 and 3.

5.4 UNDERSTANDING THE RAW DATA

Both CLAWS systems offer capture modes with several vertical input ranges. Data recorded in different modes are converted to volts to be comparable. This sections aims at giving the reader a better understanding of the raw data, its structure, and uncertainty. It is applicable for data from the Phases 2 and 3.

CONVERSION FROM ADC TO VOLTS The data recorded by the oscilloscopes is digitized with 8 bit resolution and returned in one array per channel with one entry per sampling point. Each data point is given in units of the *analog digital converter* (ADC) and ranges from -32512 to $+32512$ in steps of 256. The time difference between adjacent array entries is defined by the sampling rate.

All values are given in mV

Vertical Range	Vertical Bit Size	Uncertainties	
		Systematic	Binary
50	0.39	1.50	0.11
500	3.94	15.00	1.14

Table 5.1: Uncertainties of the most used vertical range settings of the oscilloscopes. These values represent the uncertainties using the high gain mode. Multiplying these values with the absolute pre-amplification factor $|f_{\text{preamp}}|$ yields the uncertainties for the low gain mode.

For a reasonable comparison of data sets recorded with distinct vertical input ranges and amplification factors, a translation from ADC to volts is required. This conversion is done by

$$a_{volt} = \left(\frac{a_{ADC}}{32512} \cdot r\right) \cdot f_{\text{preamp}} \tag{5.3}$$

with the output value a_{volt} in volts, the input value a_{ADC} in ADC, and the input range of the oscilloscope r in volts. The factor $f_{\text{preamp}} \in \{1, -8.9\}$ depends on the gain mode used. In high gain mode, the inverting pre-amplifier is switched on ($f_{\text{preamp}} = 1$). The usage of the low gain mode changes these value to $f_{\text{preamp}} = -8.9$.

UNCERTAINTIES The uncertainty of the amplitude of the signals depends on the vertical range chosen for the oscilloscope. There are two types of uncertainties identified: a systematic and a binary uncertainty. The manufacturer states a systematic uncertainty of 3 % of the applied vertical range which can be assumed constant over the time of the experiment [75]. The binary uncertainty is given by the size of a bit in units of the ADC over $\sqrt{12}$. Table 5.1 shows the uncertainties for the most used vertical ranges.

Fig. 5.9 shows a 1 p.e. signal (left) and a high energetic hit (right) including their uncertainties. Noteworthy are the distinct vertical scales. The small signal on the left was captured during a calibration run with a vertical range of ± 50 mV and in high gain mode while the signal on the right was captured with a vertical range of ± 500 mV and in low gain mode. In order to match the uncertainties for data recorded in low gain mode, the values in Table 5.1 have to be multiplied by the absolute pre-amplification factor of $|f_{\text{preamp}}| = 8.9$. Important to note, the usage of a large vertical range as used for Fig. 5.9 (right) reduces the resolution. Single firing pixels cannot be resolved in this measurement mode but high energetic signals such as particles coming from injection bunches are recorded without exceeding the vertical range. However, these uncertainties play a minor role in both analyses, fast and offline, as shown in Section 6.2.2 and Part iii.

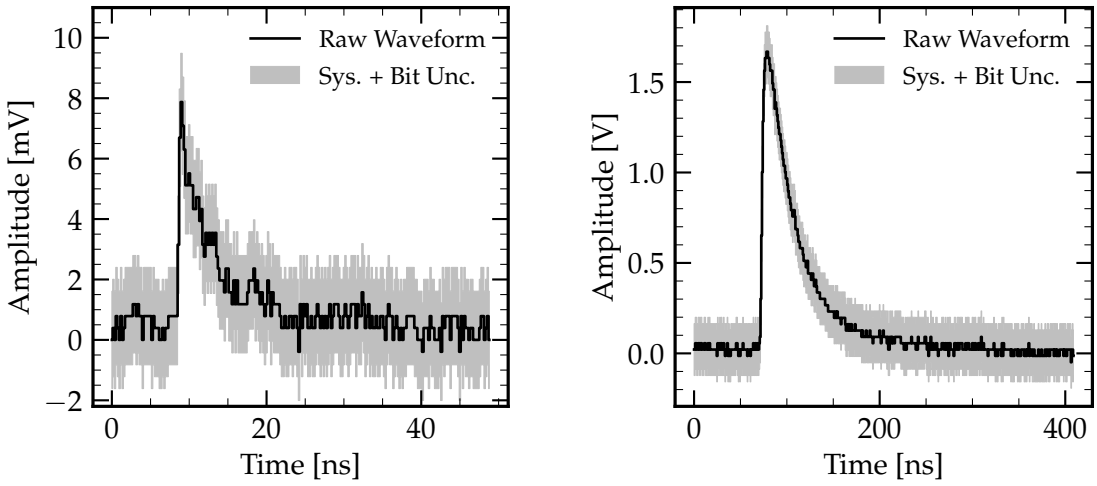

Figure 5.9: *(left)* The 1 p.e. signal from intrinsic SiPM noise was recorded with a vertical range of ±50 mV and in high gain mode. *(right)* High energetic MIP hit recorded with a vertical range of ±500 mV and in low gain mode. Please note the different scalings on the vertical axis.

A RAW PHYSICS WAVEFORM Fig. 5.10 shows a typical raw injection waveform as recorded with one CLAWS module. Noteworthy is the long capturing time of 30 ms with a sampling time of $t_{\text{sampling}} = 800\,\text{ps}$. The inset displays a zoom on an early time range of the recorded waveform.

This typical injection signal shows considerable hits at early times which decrease in amplitude and duration turn by turn. Recurring hits every $t \approx 10\,\mu\text{s}$, as nicely visible in the inset, match the SuperKEKB revolution time. The first hit in the inset is followed by an undershoot shifting the baseline to negative for a few microseconds. These undershoots appear subsequently to considerably large hits. They originate from reestablishing the capacity of the fired pixels and, therefore, should contain the same area as the hit.

5.5 CALIBRATION

The calibration of each individual detector module is the basis for the fast reconstruction described later in Section 6.2. In addition, it serves as a functionality test after the module assembly and ensures a proper performance. The calibration process consists of two parts. First, a *dark rate measurement* is performed and second, the most probable detector response known as the *light yield* is determined in units of p.e.

The detector calibration procedure is equal in both Phases. The detailed procedure for the Phase 2 detectors can be found in the master's thesis compiled by a former student [62]. In the following, the calibration process is presented using the Phase 3 modules and data. A list with the results of this section is available in Appendix B in Table B.1.

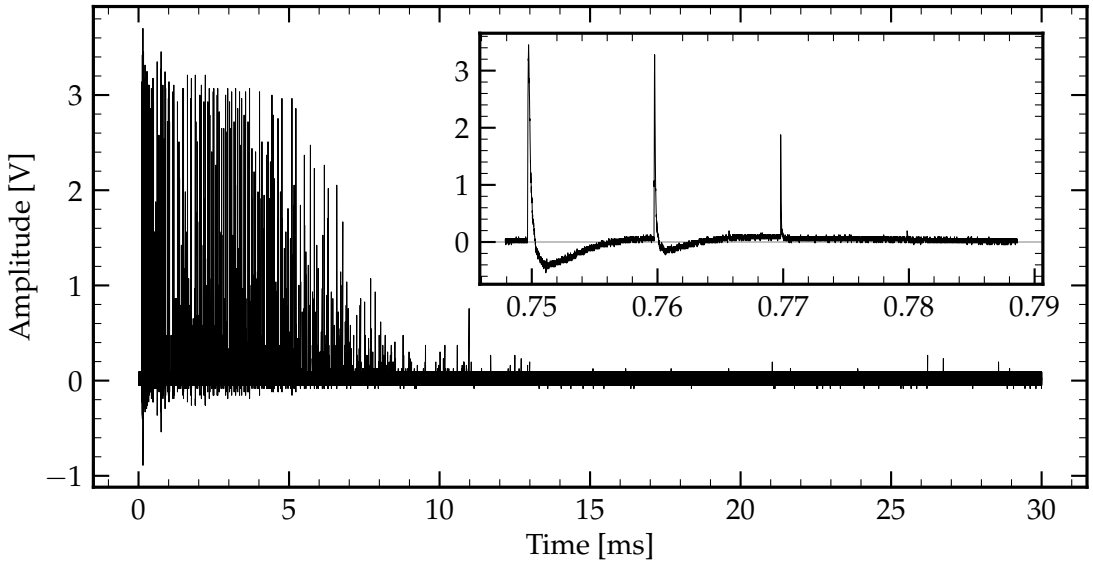

Figure 5.10: A typical raw injection waveform captured with a vertical range of ±500 mV and in low gain mode. For better visibility of the baseline shift, a narrow line in the inset marks $y = 0$ V. The units of the x and y axis of the inset are equal to the outer axes labels.

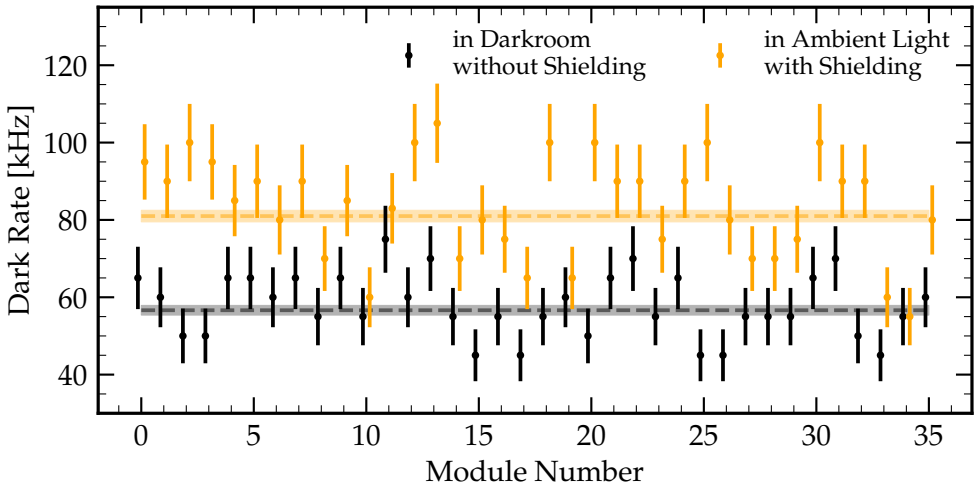

Figure 5.11: Dark rate per module in two different environments. The horizontal lines show the weighted mean in the color of the corresponding measurement.

DARK RATE MEASUREMENT As discussed in earlier, thermal excitations in the pixels of the SiPM generate fake photon hits of single or multiple p.e. In addition to this noise, ambient light can reach the active part of the module through imperfections in the light shielding. For the final Phase 3 modules, both effects add up to an increased dark rate. In order to disentangle these effects, two measurements of the dark rate are performed. In the first measurement, the dark rate of each module is measured in a light tight environment[1] before being wrapped in light absorbing aluminum foil. In the second measurement, the dark rate is measured in an environment with ambient light but all modules are prepared light tight. Both measurements are performed in a temperature controlled environment at 20 °C. The device used for this measurement is an *Agilent 53230A* universal frequency counter. This device counts voltage excitations above a certain threshold which is set to be smaller than the 1 p.e. amplitude. The integration time is 10 s.

Fig. 5.11 displays the measurement results. The dark rate measurement in a light tight environment is in agreement with the dark rate stated by the manufacturer [64]. The weighted mean yields an average dark rate of (56.65 ± 1.25) kHz. For the measurement with light tight packaging and in ambient light the weighted mean is increased by around 43 % and yields (81.00 ± 1.50) kHz. This increase can be explained with the high complexity of shielding single photons. However, the defined maximal dark rate of around 100 kHz was not reached in the most cases.

LIGHT YIELD The *light yield* is a characteristic detector parameter. It is unique for each module and represents the most probable detector response in p.e. The light yield is estimated by measuring the signal response of a *minimum ionizing particle (MIP)* penetrating the module. MIPs deposit on average a known amount of energy in the penetrated material. Cosmic muons offer a reliable natural source of MIPs and are therefore used in this setup.

For the measurement, a minimum of three modules are organized as a stack with the active components on top of each other as shown in Fig. 5.12. The uppermost and lowermost modules are combined to a coincidence trigger. Two simultaneous signals above a predefined threshold in both trigger modules indicate the passage of a MIP through the middle module. In this way, more than 2000 MIP signals per sensor have been recorded. The resulting distribution of energy loss by ionization in thin layers is described by a Landau distribution [76]. Normalizing each MIP signal by the SiPM gain[2] yields the data in the unit of p.e. A Gaussian fit around the most probable value

1 The modules are put in a climate chamber with an additional light-absorbing blanked covering the climate chamber. In addition, all curtains are closed and the windows to the corridor are covered. There is no light switched on for the time of the measurement. However, shielding single photons turns out to be a very challenging task.

2 The gain of each SiPM is determined under the same conditions using the DAQ software as described later in Section 6.2.1. An exemplary plot of the gain determination is found in Fig. B.1 (left).

of the distribution yields the module specific light yield[3]. The fit results are shown in Fig. 5.13. The systematic errors are assumed to result from variations in the packaging process of the tiles in the reflective foil and the positioning of the tile with respect to the SiPM. It is estimate to $err_{sys} = 2$ and constant for all modules. The weighted mean of (21.14 ± 0.39) p.e. was taken as input parameter for the fast reconstruction following in Section 6.2.

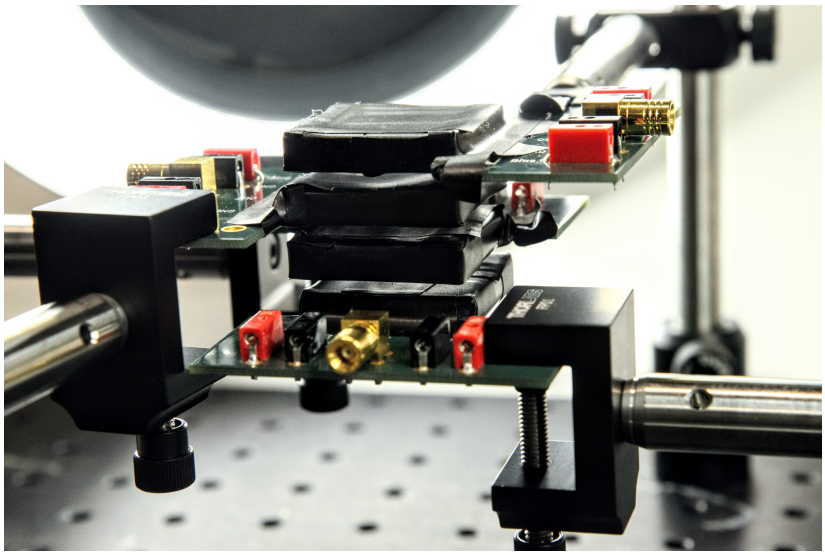

Figure 5.12: Exemplary calibration setup with Phase 1 sensors.

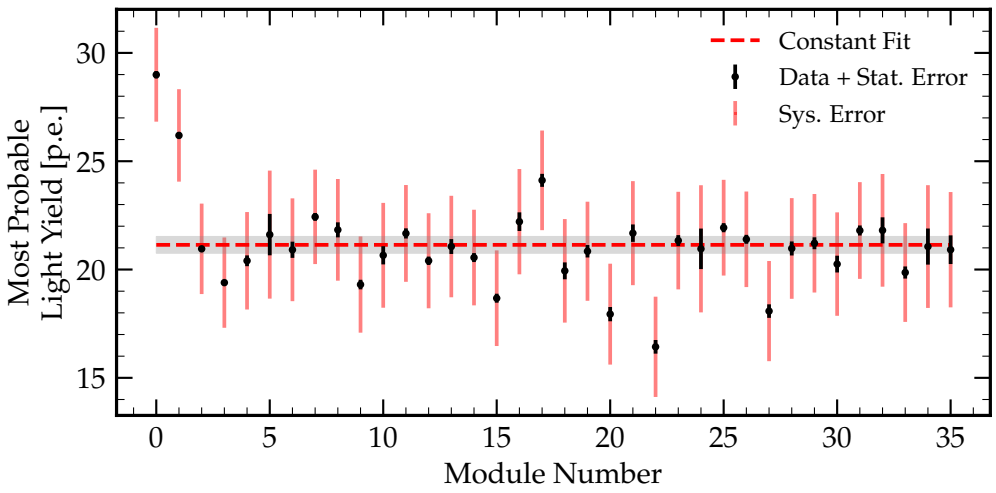

Figure 5.13: Most probable MIP responses of the Phase 3 detectors. The weighted mean is shown as a horizontal line at (21.14 ± 0.39) p.e.

3 An exemplary plot is illustrated in Appendix B in Fig. B.1 (right).

6

DATA ACQUISITION

The Claws DAQ combines the strengths of the hardware components with a fast waveform reconstruction. It provides an online display with detailed injection background information from the IP for Belle 2 and SuperKEKB shifters. In addition, it redundantly stores the recorded data on a local RAID and synchronizes it on a regular basis to different computing sites.

In this chapter, first the data acquisition system is presented with its soft- and hardware components. Afterwards, the algorithms of the *fast reconstruction* are illustrated and a benchmark of the DAQ is presented. In the last section, a selected set of the online displays are shown.

6.1 DATA ACQUISITION SYSTEM

This sections provides detailed information about the DAQ software and hardware. In addition, the integration into the experiment's slow control and the Claws data storage is presented. The DAQ software explained in the following was explicitly developed for the second phase of the SuperKEKB commissioning. Its usage continued in Phase 3 with minor modifications.

REQUIREMENTS SPECIFICATION The requirements for a functional Phase 2 DAQ system can be summarized to the following key areas:

- *Integration of oscilloscopes and power supply*
  Automatized steering of all devices. The need for human interference at the experimental side should be minimized.
- *Fast update rate of the online display*
  The key feature of a real-time feedback should be preserved. An update time of not more than 10 s is targeted.
- *Integration into the Epics slow control environment*
  Making the analyzed data available within the experimental infrastructure and enable an externally issued emergency shutdown.
- *Reliable and fast data storage*
  Optional saving of the raw and analyzed data in a fast and redundant manner.

- *Continuous responsiveness of the main interface*
  Allowing a smooth handling of the software, e.g. reloading configuration files without re-initializing the entire software.

Unfortunately, the DAQ used in Phase 1 did not fulfill the requirements sufficiently. In Phase 1, the programming language of choice was the graphical programming language *Labview* [77]. Inefficient memory management limited the amount of data acquired in one record and resulted in large update time and a low duty cycle, even for short waveforms. For this reason, the usage in the second phase of commissioning with twice as many channels was not possible without a fundamental redesign of the Labview-based Phase 1 DAQ software.

SOFTWARE & SDK OVERVIEW In order to meet the identified goals, the programming language C++ in the 2014 standard was chosen as the main programming language. Explicit memory management, a strong set of methods in the standard library (STL), various well developed external libraries, a native *software development kit* (SDK) for the oscilloscopes, and, of course, a broad and helpful online community made C++ an excellent choice. Other languages used are Python 3 for e.g. post-reconstruction data processing and GNU bash mostly for data storage tasks.

In more than 8500 lines of bare code, this project makes mostly use of the following internal and external libraries: C++ STL for e.g. multi core processing, BOOST C++ Libraries v1.58 [78] for the realization of a state machine and input/output (IO) of the configuration files, the ROOT Data Analysis Framework v6.10 [79] for saving raw and online data in compressed ROOT-TFiles, the Picotech PS6000 Library [80] for a custom and resource saving communication with the oscilloscopes, the Spdlog [81] library to enable thread-safe logging, and EPICS v3.14.12 [82, 83] to integrate the software into the slow control infrastructure of the Belle 2 experiment.

WORKFLOW Fig. 6.1 gives an overview of the workflow of the Phase 2 DAQ software. The software starts in the *IDLE* state shown centrally in the upper part of the figure. After start, the *init* command should be the first call initializing and checking all resources and loading the correct configuration files. The *start* command instantiates a new thread outsourcing the work. This way the main interface stays responsive for future calls. This thread runs two nested loops: the outer *run loop* and the inner *sub-run loop*. The run loop stays alive until the *stop* command is issued by a user via the slow control or command line input. Once the data taking started, every run loop iteration begins a new *run* and starts with the calibration of the sensors. After the calibration the sub-run loop begins. Each sub-run is one data record triggered by the injection trigger signal or auto-trigger. After a trigger issued the record and transfer of the data from the oscilloscopes into the memory of the computer, one thread per four channels speeds up the resource consuming analysis of the data.

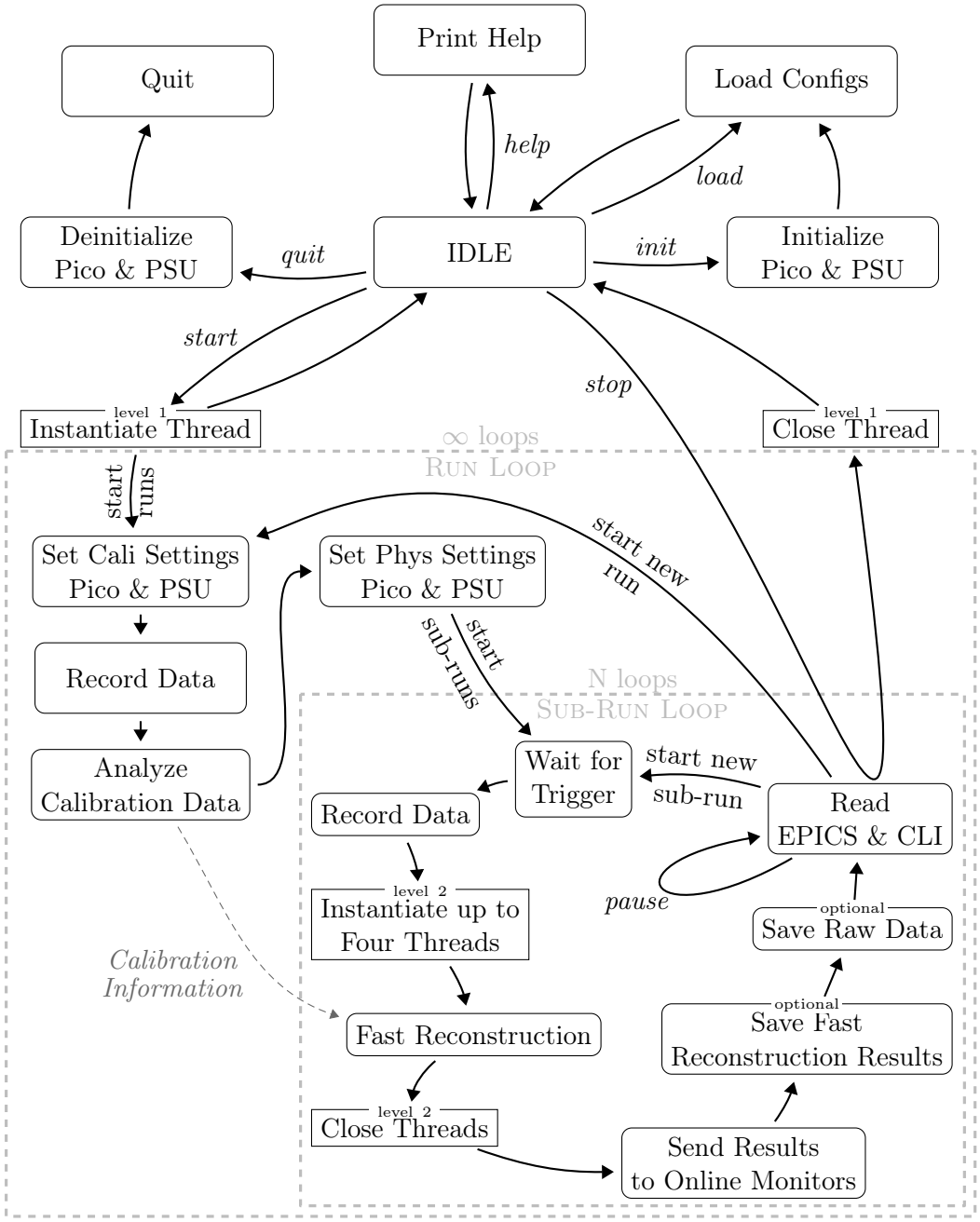

Figure 6.1: Workflow schematics of the Phase 2 data acquisition software. The program starts in the *IDLE* state shown centrally in the top part. There are four kinds of paths: *(a)* The arrows with attached text in italics are paths issued by an external command input. *(b)* Arrows with sloped text are automated decisions by the algorithm following previous defined conditions. *(c)* Arrows without any text show the next state after the current state is finished. **d)** Gray dashed arrows with gray text in italics show an information transfer.

In the next step, the results are broadcasted on the network. Saving raw and fast reconstructed data is optional in order to increase the duty cycle of the system. If there are no commands by the user in the queue and the number of sub-run iterations is not reached yet, a new sub run is started. Depending on the run mode, a typical number of sub-run loops is between 50 and 200.

NETWORK & SLOW CONTROL INTEGRATION As all BEAST detectors, CLAWS uses EPICS to share analyzed data and other information via the slow control network used by Belle 2 and SuperKEKB. EPICS allows writing and reading variables of various data types via network. For this purpose, the DAQ uses the low level EPICS library for broadcasting fast reconstructed data (see Section 6.2) and other information like the *current state* of the DAQ and reading steering variables such as *start/stop*, *save raw data/save online data/not saving* and *emergency shutdown*. All CLAWS related variables are hosted by an EPICS server on the same machine using the high-level EPICS integration of PCASpy [83]. Each variable uses the prefix *BEAST:CLAWS:* as detector identification. All published variables can be accessed anywhere in the network and, for example, visualized using third party software.

DATA STORAGE & PERSISTENCE Storing the recorded data safely enables the option for a detailed and more specific offline analysis. The Phase 2 software allows for saving two different kinds of data: The results of the fast reconstruction and calibration data and/or the raw data as recorded by the oscilloscopes. The required storage capacity for 16 channels per sub run varies between 50 kB and 900 MB for fast reconstructed and raw data, respectively. In Phase 2, a total 5.3 TB of data is stored.

Aiming at a high level of data persistence, all data is saved in a redundant manner using a level 5 software RAID. Three hard disk with 3 TB each are combined to one logical volume of 6 TB using the Unix software *mdadm*. The advantage of using a RAID5 system is data redundancy[1] and an accelerated reading speed when accessing data.

The locally stored data was regularly synchronized using the Unix software *rsync* to the ceph storage of the MPP and to the KEK computing storage at KEKCC. This synchronization process was started each night at 2 a.m. JST when the general internet traffic is expected to be low at the respective sites. Further compression of the data was not needed since ROOT's TFiles include native compression.

6.2 FAST RECONSTRUCTION

The goal of the fast reconstruction is to provide meaningful processed data of the current beam conditions to the accelerator working group and to the Belle 2 shifters

1 If one drive fails, the data on that drive can be recalculated from distributed parity information on the other drives. No data loss happens.

as fast as possible. The fast reconstruction consists of two steps: A detector calibration analysis and the subsequent reconstruction of the raw waveforms. The first step corrects fluctuations in the gain of a SiPM due to temperature changes by analyzing dedicated calibration data at the beginning of each run. The determined calibration values are used until the start of the next run. Each new sub run triggers the fast reconstruction as illustrated in the workflow schematics in Fig. 6.1.

In the following, the analysis strategies for the calibration and for the reconstruction are described in detail. After that, the benchmark results of the processing speed of the fast reconstruction are shown.

6.2.1 *Calibration*

The calibration at the beginning of each run aims at determining the gain and, therefore, correct possible temperature fluctuations in the experimental volume. In order to reach this, the trigger is adjusted to trigger on 1 p.e. signals. The detectors are set to high gain mode and the oscilloscopes are set to a vertical range of $\pm 50\,\mathrm{mV}$. That way one thousand 1 p.e. signals per channel are recorded. Fig. 6.2 (left) illustrates such a 1 p.e. signal.

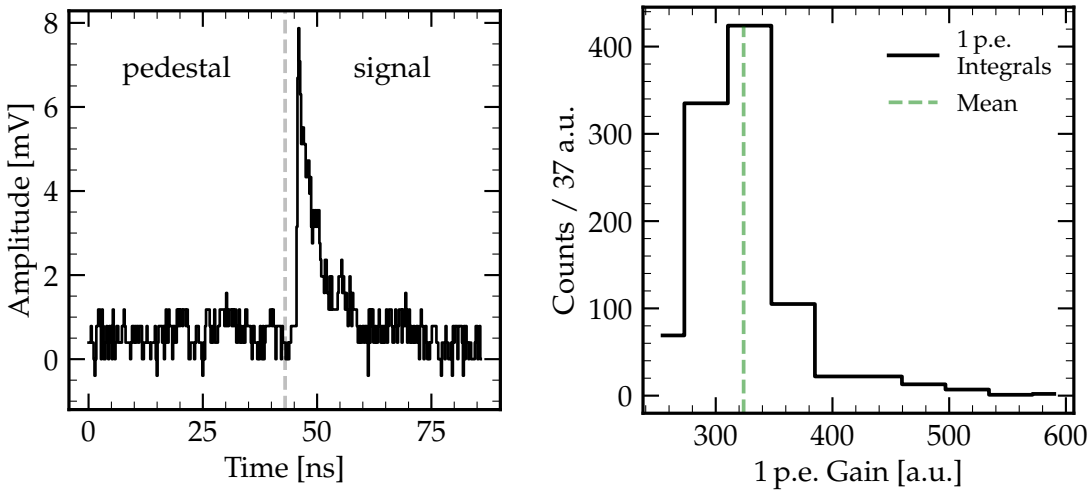

Figure 6.2: *(left)* Example waveform of a typical 1 p.e. signal recorded in calibration mode. *(right)* Histogram of the pedestal corrected integral of one thousand 1 p.e. signals.

To enable a fast acquisition, the oscilloscope's internal memory is split in 1000 segments each holding just enough space for one 1 p.e. calibration waveform. After all segments are filled, the data transfer via USB3 into the local memory of the computer begins. This PicoScope internal feature called *rapid block mode* [84] accelerates the recording and transfer procedure by a factor 1000 [84] in comparison to the usual *block mode*[2]. Using this feature, the time between two recordings shrinks down to

2 One waveform after another gets recorded and is immediately transferred to the computer, no matter if the oscilloscope's internal memory has free space left or not.

$\mathcal{O}(1\,\mu s)$, increasing the duty cycle of the system. Once the calibration data acquisition is completed, one recorded waveform per channel is available in a large array of integers in the unit of ADC. The time difference between consecutive bins is given by the sampling frequency. For Phase 2 and most of Phase 3 the sampling frequency per channel was adjusted to 1.25 GHz equal to a sampling time of 800 ps.

Fig. 6.2 (left) illustrates the special record settings for the 1 p.e. signals: The gray dashed vertical line splits the waveform in two equally sized parts. The first half is used for pedestal correction and the second contains the 1 p.e. signal. Using this additional information, the pedestal subtracted integral of the 1 p.e. signal is obtained by subtracting the integral of the first half from the integral of the second half. The gain is then calculated by

$$G = \frac{1}{N} \sum_{i=1}^{N} (I_{i;S} - I_{i;P}) \tag{6.1}$$

with $I_{i;\,P}$ and $I_{i;\,S}$ being the integral of the pedestal, respectively signal, half of the i-th waveform as shown in Fig. 6.2 (left). N is the total number of 1 p.e. waveforms recorded. Fig. 6.2 (right) shows the gain mean value in green together with a histogram of the same data. The shown mean is a good approximation of the most probable value of the underlying distribution while being not as computational intensive as a fit. In addition, calculating a mean value is more robust when working with volatile data compared to fitting.

CALIBRATION PROCEDURE ADJUSTMENT In Phase 2, the close vicinity of CLAWS to the IP led to an increased radiation damage over the time of the experiment. After a few weeks of run time, the radiation damage increased the dark rate of the SiPMs substantially as Fig. 6.3 (top) illustrates. Throughout the time of the experiment, the dark rate increased continuously to around 200 MHz. Despite the short record time of $<$100 ns, multiple 1 p.e. signals have been captured overlapping each other. Fig. 6.3 (middle) shows the relative gain as extracted by the calibration procedure. The graph follows the trend of the dark rate plot above. With an increasing dark rate the introduced calibration procedure yields strongly fluctuating calibration values. The ability to trigger on single 1 p.e. signals becomes unlikely with an increased radiation damage. For the first month of run time, the calibration procedure produces rather similar 1 p.e. calibration gain values. But after that, the gain increases to up to a factor 18 larger than at the beginning of Phase 2. Fig. 6.3 (bottom) depicts the relative amplitude of the 1 p.e. signals. The amplitude shows large errors at the beginning in March which decreases over the time of Phase 2 due to the increased sample size thanks to the high dark rate. This plot indicates that even with an increasing radiation damage the shape of the 1 p.e. signals does not change. Later in Chapter 7 we will see that also the most probable MIP response stays constant within around 10 % over the course of Phase 2.

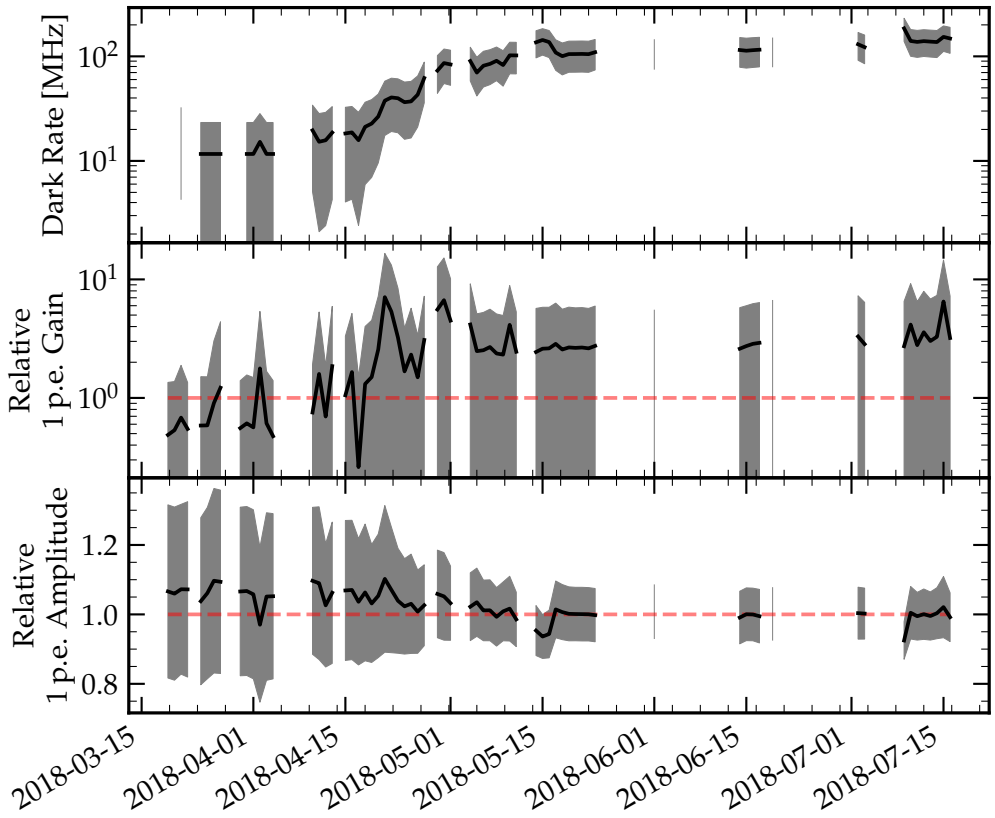

Figure 6.3: Calibration related plots. The x-axis is shared by all plots and shows the active run time of Phase 2. Each plot shows the average value per day over all sensors in black. The gray area represents the error. *(top)* shows the mean dark rate. *(middle)* shows the relative gain as determined by the calibration. The data is normalized by the weighted mean $\mu_{\text{weighted}} = -110\,930$ ADC s. *(bottom)* illustrates the relative amplitude of single 1 p.e. signals. The data is normalized by the weighted mean $\mu_{\text{weighted}} = 2766$ ADC. The horizontal dashed lines in the amplitude and gain plot serve as eye guidance for the data fluctuation. All plots use raw calibration data.

However, the strong fluctuations at the beginning and end of April lead to a change of the detector calibration. The vertex detector cooling system *IBBelle* kept the temperature in the volume sufficiently stable that the run-wise calibration was omitted. Instead, the calibration values from earlier times are read-in via text file into the DAQ software.

6.2.2 *Waveform Reconstruction*

The *waveform reconstruction algorithm* aims at reconstructing the particle energy and arrival time of the single signals in a raw waveform. The waveform returned by this algorithm is of the same length and sample frequency as the original waveform.

The algorithm starts after a physics event is recorded and copied into the local memory of the work station. The reconstruction algorithm which will be explained in the following is applied channel-wise. In order to minimize the computation time,

one dedicated analysis thread per four channels is created. A further increase of the number of working threads did not improve the overall performance since the creation of new threads using the C++ STL *thread library* does cost some milliseconds of computation time. The following algorithm is written in C++ and part of the DAQ. In this section, the waveform reconstruction is presented in two steps: First, the signals are identified in the raw waveform. In the second step, the energy content of each signal is determined and the waveform is reconstructed.

SIGNAL IDENTIFICATION The signal identification is a machine learning algorithm which is trained to find signals in a raw CLAWS waveform. Its behavior is controlled by five parameters: *scanning step size*, *signal threshold*, *minimum signal length*, *pre-threshold*, and *tail length*. The signal threshold parameter is given in the unit ADC while all others are given in samples. These parameters are loaded either after the initialization step or when new settings are loaded. Different run mode settings have different analysis parameter values. For example, when running in high gain mode other values are required in comparison to runs in low gain mode. In the latter case, e.g. SiPM intrinsic dark rate is not observable with the low vertical resolution.

In the first step, the waveform is scanned for potential signals. This is done by checking if a bin is above the *signal threshold* which is the minimum required amplitude. For reasons of efficiency, not all bins are evaluated but bins in steps of the *scanning step size* as shown in Fig. 6.4 (left). For Phase 2 and 3, a scanning step size of 10 was chosen minimizing the processing work to only 10 % of the full waveform. Increasing this value further is not recommended, since the chance of missing out potential signals increases, too. As Fig. 6.4 (left) shows, the narrow part of a signal above the *signal threshold* must be hit. The threshold value is given in steps of 256 and ranges from 0 to 65024 since it is applied after offset correction. The positive identification of a bin above the signal threshold starts the search for the last bin above the threshold which is done bin by bin. The *minimum signal length* parameter defines the required minimum length of a signal above threshold. This serves as a safety margin excluding potential dark rate signals. However, if running in low gain mode, this parameter could be set to 0.

As soon as the signal part above the threshold is identified, the full signal can be constructed. Fig. 6.4 (right) helps understanding the construction of the full signal. The *signal start* is defined starting at the last scanning step below threshold and shifted to the left by the *pre-threshold* parameter. This ensures the inclusion of the full signal rise time. Values for this parameter ranged between 5 and 10 bins. The *signal end* is defined as the last bin above the signal threshold plus a shift to the right by the *tail length* parameter. Experience showed that values around 200 fit for most of the signals independent of their amplitude. The full signal is defined to start from the first *pre-threshold* bin until the end of the *tail*.

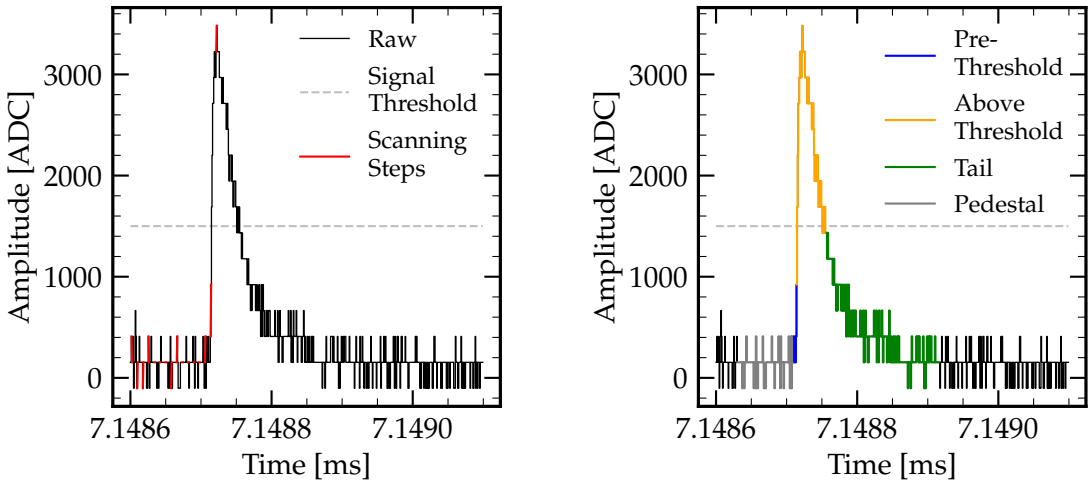

Figure 6.4: Both plots show the same example of a MIP signal. They illustrate the different steps and interim results of the signal identification in a raw CLAWS waveform.

RECONSTRUCTING THE WAVEFORM In order to reconstruct the raw waveform, arrival time and energy of each found signal in the waveform must be determined. The arrival time of a signal is defined at its *signal start* value and the energy content in MIPs is calculated in two steps and uses the previous estimated calibration values.

In the first step, the integral of the signal is calculated with pedestal correction:

$$I_{\mathrm{S;\,norm}} = (I_{\mathrm{S}} - l_{\mathrm{S}} \cdot \bar{p}) \cdot f_{\mathrm{preamp}} \cdot \frac{r}{50\,\mathrm{mV}} \tag{6.2}$$

with the integral of the signal I_{S}, the signal length l_{S} in samples, the pre-amplification factor $f_{\mathrm{preamp}} \in \{1, -8.9\}$, and the vertical input range of the oscilloscope r in volts. The mean pedestal per sample $\bar{p}$ is estimated using the pedestal part in front of the signal as indicated in Fig. 6.4 (right).

In the second step, the normalized integral is divided by the SiPM gain G and the MIP response R_{MIP} following the procedures described in Sections 5.5 and 6.2.1, respectively. This yields the MIP content $E_{\mathrm{S;\,MIP}}$ per signal:

$$E_{\mathrm{S;\,MIP}} = \frac{I_{\mathrm{S;\,norm}}}{G \cdot R_{\mathrm{MIP}}}. \tag{6.3}$$

The final step combines all intermediate results. An array with the same size of the original waveform is filled with the signal energies calculated with Eq. (6.3) at *signal start*. All other array entries are set to zero. A subsequent binning is optional and reduces the amount of data to be saved or send via network. An example of a raw waveform and its *reconstructed waveform* with an 8 µs ($\approx 0.8 \cdot T_{rev}$) binning is shown in Fig. 6.5. The chosen binning factor of 1000 holds up a sufficient amount of timing information while reducing the amount of data to a tolerable level for the fast distribution to the online displays. Important to note, the y-axis of the raw waveform on the top is in the unit of ADC and the y-axis of the reconstructed waveform on the

bottom is in the unit of kMIP per 8 µs. The comparison of the single signals in the raw and reconstructed waveform illustrates that the energy content of a signal is not defined by the absolute amplitude but is proportional to its integral. A good visual estimate of the energy content of large signals is archived by focusing on the signal's undershoot. The reconstructed signals with a large energy content do have a visible undershoot in the raw waveform above.

Other useful quantities such as the *particle rate* or the *cumulative sum* are derived from the reconstructed waveform. For example, the *particle rate* in the unit $\mathrm{Hz/cm^2}$ is calculated with

$$R = \frac{I_{wf}}{l_{wf} \cdot A} \tag{6.4}$$

using the integral of the reconstructed waveform I_{wf}, the length of the waveform in seconds l_{wf}, and the active area A of the channel in square centimeters. It is shown in Fig. 6.5 (bottom) in the top middle. The *cumulative sum* is drawn as a gray dashed line in Fig. 6.5 (bottom). Its y-axis label on the right is given in percent and signifies the fraction of particles observed versus the record time. In this example, we can read that, e.g., around 65 % of the particles in this waveform are observed within the first millisecond.

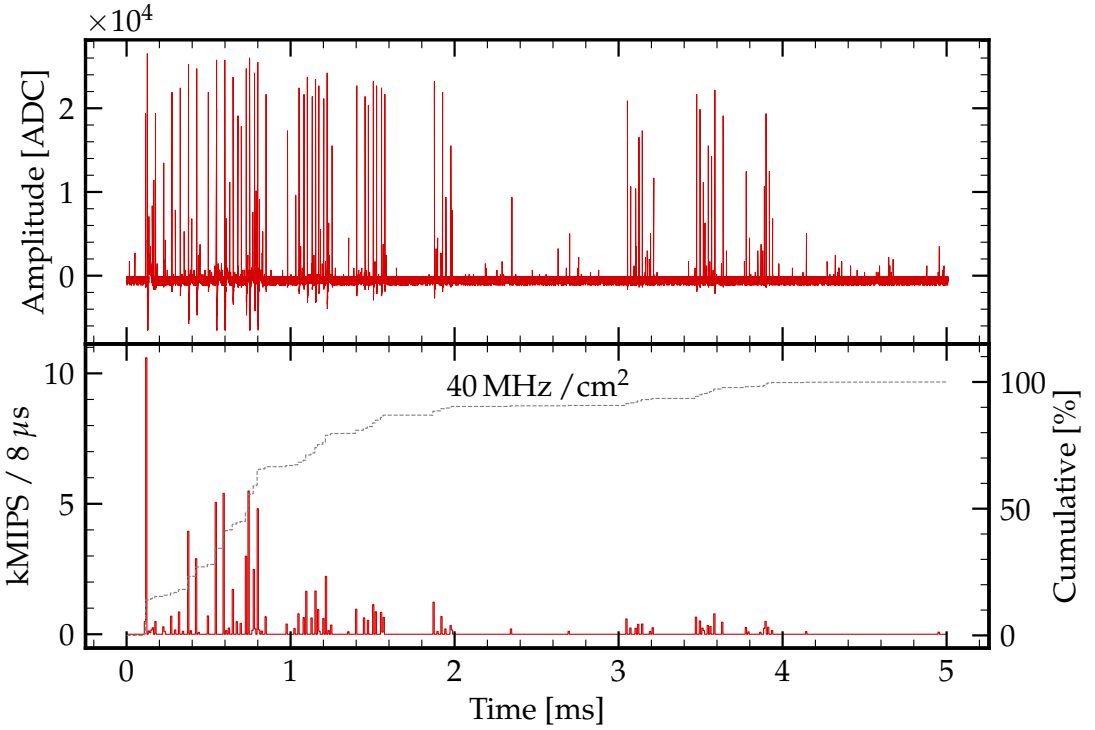

Figure 6.5: Example waveform illustrating the fast reconstruction results. The data shows a LER injection from April 29th 2018 with run number 510532-0078 recorded with channel Top Backward C. *(top)* Offset corrected raw waveform. *(bottom)* Reconstructed waveform with supplementing information. The number in the top shows the particle rate. The dashed line illustrates the cumulative sum. The factor $\times 10^4$ belongs to the top plot only.

STORAGE & SECONDARY USAGE OF FAST RECONSTRUCTION RESULTS The results obtained in the *fast reconstruction* can optionally be stored on hard disk. For each channel and sub run, the reconstructed waveform, its MIP content, its cumulative and the mean 1 p.e. gain are stored in a ROOT file. In addition, accelerator parameters such as the beam gates statuses, beam currents and others have been added in the course of Phase 2. The saving of the collider information together with the *fast reconstruction* results allow to find data with specific conditions more rapidly and grants the possibility of an offline analysis of the *fast reconstruction* data.

The Python3 package CLAWS *Analysis Toolkit (CAT)* [85] was developed by my colleague Thomas Kraetzschmar and me for the analysis of the *fast reconstruction* data. CAT is a collection of functions for querying the data by various attributes and allows, for example, applying basic analysis techniques such as creating an average of waveforms of every channel for a defined time range or creating an autocorrelation plot. This analysis kit helped summarizing the CLAWS data and produced various plots for several run meetings.

6.3 ONLINE MONITORS

On March 19th 2018, the second phase of the SuperKEKB commissioning started 18 month after the end of Phase 1. It was the very first time for the SuperKEKB working group to guide particles through the final focusing magnets and the interaction region in the middle of the Belle 2 detector. For the reason of safety, all of the Belle 2 sub-detectors have been switched off. Concerns of degrading detector saturation and especially detector damage from off-track electrons was high. The only information about the conditions at the IP inside of the Belle 2 detector was offered by the BEAST detectors and combined to an online monitor.

Such a fast feedback of the conditions at the interaction region is a crucial component for achieving a stable circulating beam while keeping the particle flux low for Belle 2. Misguided particle bunches can have a dramatic impact when crossing sensitive detector parts. Having detailed real-time knowledge about the radiation level and particle flux in the interaction region does help avoiding such undesirable incidents. But even after stable beams have been accomplished in both rings, the background level was too high for a save Belle 2 operation. For the first two month of Phase 2, the BEAST online monitors have been the exclusive information source to mitigate the background in the interaction region.

6.3.1 *Implementation*

The framework in which the real-time feedback is implemented is called EPICS. It is a distributed control system featuring a large number of connected devices. EPICS

allows to read and write values in various data types with millisecond precision. These so called *process variables (PVs)* are hosted on different servers within the network. For data visualization, the *Control System Studio (CSS)* [86] is used on the client computer to combine and plot PVs from several hosts. Using these two frameworks, data sets from BEAST detectors, SuperKEKB beam monitoring hardware, and later also Belle 2 detectors have been combined to visualize the background conditions of the interaction region.

6.3.2 *Exemplary Plots*

The online displays underwent constant advancements such as including more data and improving the information accessibility. However, some central plots relevant throughout Phase 2 are illustrated in Fig. 6.6 as part of the online monitors of the *Beast Commissioning Group (BCG)*. All shown plots update at a rate of around 1 Hz. *(A)* shows the dose rate observed by the Diamond detector while *(B)* visualizes the particle rate from CLAWS, Fangs and the Plume detectors versus time of day. *(C)* illustrates the neutron rate measured by the two detector system He3 and TPC. Illustration *(D)* displays two CLAWS reconstructed waveforms from backward and forward oriented channels. The x-axis shows 5 ms ($\approx$ 500 Turns) past the injection trigger arrival and the y-axis represents the energy content in MIP/8 µs. *(D)* shows the average rate after particle injection observed by the Plume detector. Its y-axis returns the pixel rate and the x-axis shows 4 ms of the injection beginning with the injection trigger arrival.

In the plots *(A)* & *(B)* one can observe injections into the main rings at around 12:53, 13:45, 14:56, and the begin of new injections at around 15:02. The high amplitude obstacles in the dose rates and the increased particle rates are clear indications for injections. The background coming from circulating particle bunches is visible as horizontal line with a slightly negative slope. Steps, as for example in *(B)* at around 14:00 and 14:25, are the result of different collimator settings. The plot *(C)* illustrates the neutron rate versus day time observed by the He3 and TPC detectors. The contrast between injection and non-injections is also noticeable but not as obvious as in *(A)* & *(B)*. Illustration *(D)* shows the evolution of the injection induced background in more detail. One can observe that the background does not occur uniformly over time, but with larger peaks within the first few hundred µs. In addition, synchrotron and betatron oscillations let the background fluctuate with slowly decreasing amplitudes beyond the recorded time window. The red horizontal line signifies an estimated equivalent of the 3 % PXD occupancy serving as an upper limit for the particle rate the PXD can cope with. *(E)* shows a similar trend for the injection induced background as shown above by CLAWS.

Fig. 6.7 shows the BCG booth in the SuperKEKB control room. The four screens on the right around *(A)* are the BCG online monitors. The screenshots from Fig. 6.6

are shown on the upper left monitor. For the first one and a half month of Phase 2, a wall-mounted screen *(B)* in the SuperKEKB control room displayed exclusively the CLAWS reconstructed waveforms highlighting the importance of reducing the injection induced background for a save operation of the VXD detectors.

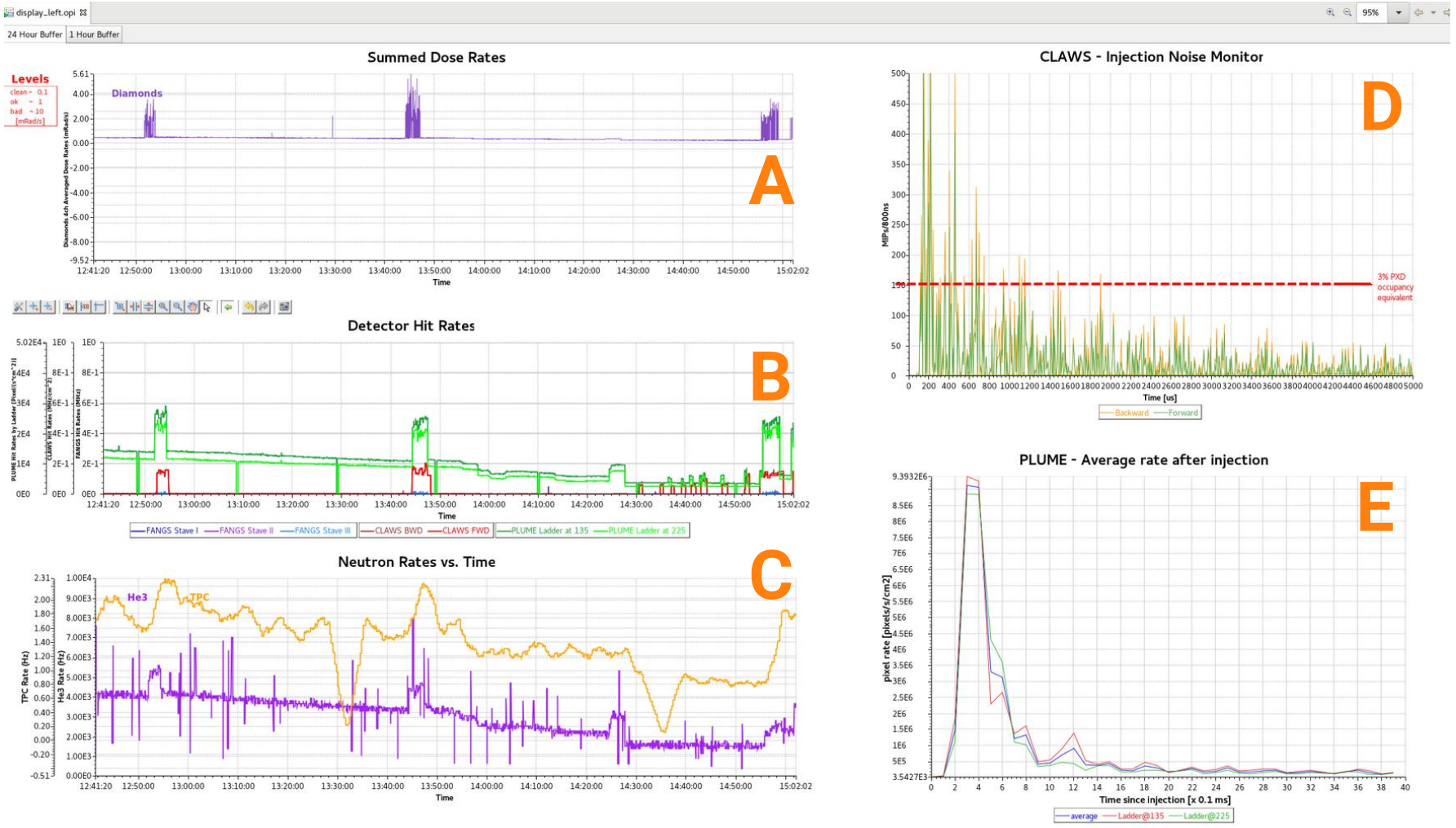

Figure 6.6: Screenshot of central components of the BCG Online Display. *(A)* Dose rates from the PIN and Diamond detectors versus day time. At that time, the PIN detector was not operational. *(B)* Particle rate versus day time from the detectors Claws, Fangs & Plume. *(C)* Neutron rate observed by the TPC & He3 detectors. *(D)* Claws reconstructed waveform. *(E)* Average rate after injection observed by Plume. Taken on April 23 2018.

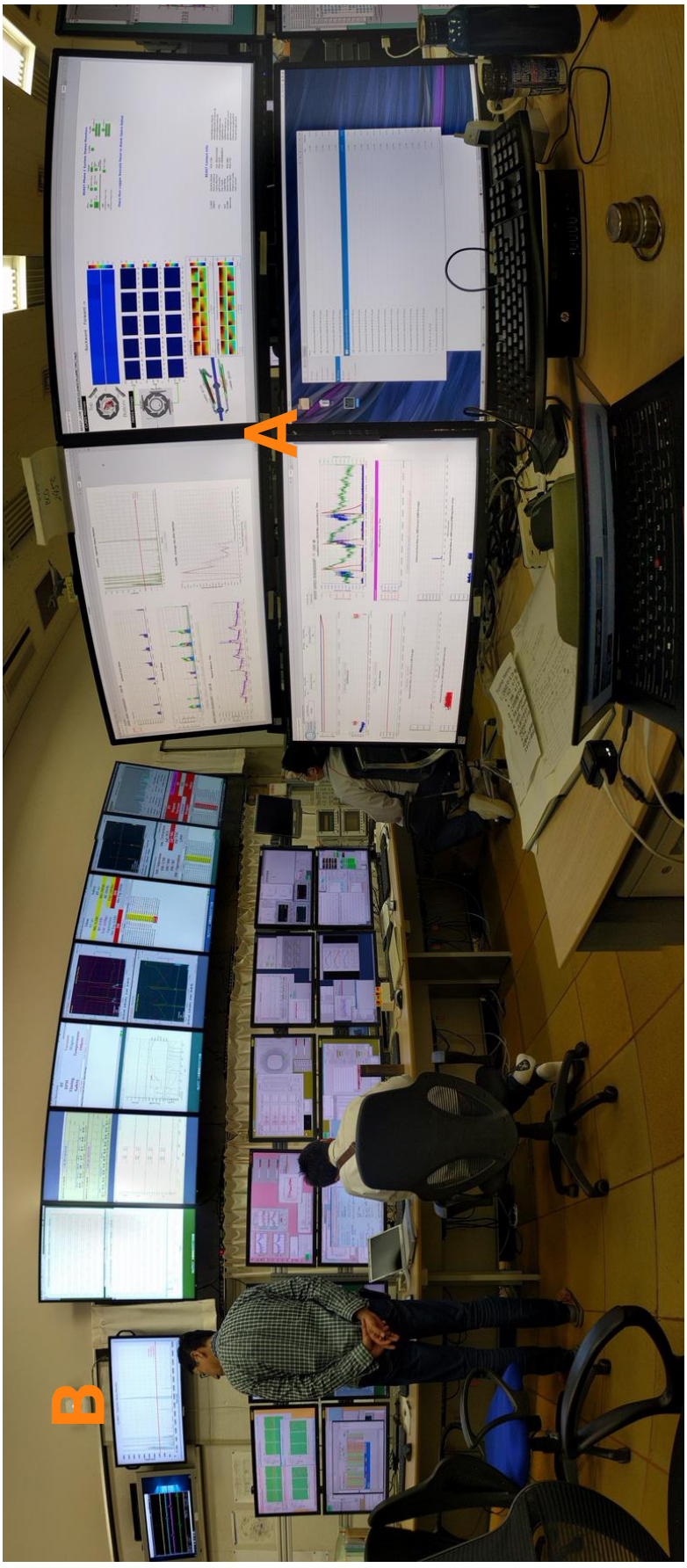

Figure 6.7: Photo of the BCG booth in the SuperKEKB control room. Taken on April 24 2018.

6.4 BENCHMARKING THE REALTIME CAPABILITIES

A fast update rate of more than 0.1 Hz is one of the design values of the DAQ system. The processing speed of the fast reconstruction is capable of fulfilling the required update rate. However, to determine the update rate of the online displays the full sub run cycle needs to be considered. This includes recording the waveforms on the oscilloscopes and copying it to the computer, applying the fast reconstruction, transmission of the results to the online monitors, and optionally saving of the raw and/or the fast reconstructed data. In the following, the processing speed of these steps will be evaluated in detail.

Table 6.1 displays the mean processing time and its standard deviation and file size in dependence of the acquired waveform length and the save raw data mode. In addition, the last column shows the number recorded injections. The parameters with the largest impacts on the processing time of one sub run cycle is the length of the acquired waveform and the *save raw data* option as shown in Table 6.1. The saving of the fast reconstruction results was always switched on since the file sizes are small. Without saving the raw waveforms, the sub run processing times of waveforms with a length up to 30 ms is below 2 s. Almost 87 % of the recorded injections in Phase 2 have been of 5 ms length and around 8 % of these are available as raw data. The processing times increase by factors between 3.8 and 29 as soon as the raw data is saved additionally. The large memory need of the raw data files in combination with the slow writing speed of the hard disks increase the overall processing time to 3.8 s and more.

Save Raw Data	Waveform Length [ms]	Processing Time		File Size	Recorded Injections	
		Mean [s]	Std Dev [s]		Absolute	Fraction
False	2.4	1.02	0.26	63 kB	119 952	10.03 %
	5	0.95	0.22	75 kB	948 037	79.25 %
	10	1.00	0.02	110 kB	4783	0.40 %
	20	nan	nan	98 kB	1	0.00 ‰
	30	1.78	0.42	133 kB	130	0.01 %
True	2.4	3.76	0.97	21 MB	33 665	2.81 %
	5	5.57	0.98	45 MB	84 708	7.08 %
	10	9.08	1.20	91 MB	1988	0.17 %
	20	22.49	15.73	182 MB	2978	0.25 %
	30	51.22	92.76	270 MB	55	0.05 ‰
	100	64.33	2.08	881 MB	5	0.00 ‰
Total	1.58 h			5.37 TB	1 196 302	

Table 6.1: Summary of the processing times and saved file sizes of one sub run in Phase 2. The saving of fast analysis results was always turned on while raw data saving was switched on for dedicated runs only. The mean and standard deviation of the processing time relate to one full sub run (c.f. *sub-run Loop* in Fig. 6.1). The timings of the fastest 95 % of the data is given. The file sizes are the mean of 30 or less files, depending on the availability.

Part III

DATA ANALYSES

This third thesis part was fully established in the scope of this thesis and comprises of the analyses of two separate data sources acquired in the second commissioning phase of the SuperKEKB collider. The first analysis uses the raw data for precise timing measurements in Chapter 7. The second analysis makes use of the much larger data set of the fast reconstruction in Chapter 8 and allows studying the continuous top-up injections in terms of the duration and its probable reasons.

7

RAW DATA ANALYSIS: TIMING, HIT ENERGY SPECTRA & TIME STRUCTURE

In Phase 2, more than 98.5 % of the total disk space occupied by CLAWS data is raw data. Only the remaining 1.5 % is fast reconstructed data. In contrast to the fast reconstructed data, the sampling time of 800 ps of the raw data enables a precise time related analysis of the injection induced background. The fast sub-nanosecond sampling time permits to study single bunches which have a time distance of $T_{\text{bunch}} = 3.930\,\text{ns}$. The preprocessing of the raw data follows the same steps as illustrated in the fast reconstruction in Section 6.2.2. However, the important difference is that the computing time of the reconstruction is not a limiting factor anymore. There is no need for simplifying assumptions to speed up the processing. Instead, the single signals in a waveform can be analyzed in all of their detail and the sampling time is preserved.

The following chapter begins with the preprocessing of the raw data. This includes the pedestal correction, the signal identification within the waveforms, a time calibration, an improved LER and HER separation and, finally, an energy calibration. The first analysis section presents a time resolved analysis allowing a direct analysis of single bunches around the injection bunch. Afterwards, a detailed study demonstrates the hit energy spectra and their distribution during one revolution in the main rings. In addition, CLAWS capability of detecting irregularities from single particles bunches is shown. The last analysis section illustrates waveforms from raw data reconstructed which are averaged over several weeks at the end of Phase 2. Furthermore, CLAWS capabilities of recording long waveforms observing the injection background development is presented.

7.1 PREPROCESSING

Before a detailed analysis of the raw data can begin, the detector has to be calibrated in time and energy. This section begins with a pedestal correction which is followed by the identification of single signals inside a raw waveform. Afterwards, a time correction is applied to correct a sampling time drift of the oscilloscopes. Then, the source of the injection background, LER or HER, is determined with a high reliability. In the last step the data is calibrated in energy in the unit of MIP, and the most probable detector response is studied over the course of Phase 2.

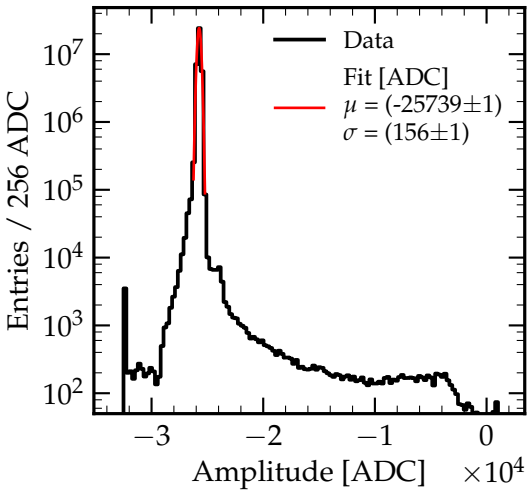

Figure 7.1: Pedestal estimation with a histogram of a raw waveform. The fit uses a Gaussian distribution and has been applied using SciPy's *curve_fit* method [87]. The data features channel Top Backward B from run 516338-0009.

7.1.1 *Pedestal Correction*

In Phase 2, the data was recorded with an offset to increase the dynamic range of the oscilloscopes. On top of the adjusted offset a pedestal of unknown size is present. For this reason an offset and pedestal correction is applied as the first step and is referred to as pedestal correction. The pedestal correction uses the fact that the large majority of signals appears in multiples of the revolution time and, therefore, most of the recorded waveform does not contain any signal. Consequently, the most common ADC value can be identified by the global maximum in a histogram of the raw waveform as shown in Fig. 7.1. In order to extract the mode of the underlying data, a Gaussian fit ± 3 bins around the mode of the histogram is applied. Subsequently, the raw waveform is shifted by the determined mean of the Gaussian which represents the pedestal level of the waveform. This procedure is applied per waveform.

7.1.2 *Signal Identification*

The signal identification is an algorithm which is trained to find single signals in a raw waveform. In contrast to a similar algorithm introduced in the *fast reconstruction* in Section 6.2.2, this algorithm does not use simplifying assumptions and, therefore, is not optimized for a fast execution. The methods which will be shown in the following are applied separately for each channel.

The procedure is able to find the begin and end of single signals of various amplitudes as illustrated in Fig. 7.2. The *signal tag* emphasizes the five signals found in this fraction of a raw waveform. As the last step, for each signal various observables are determined. For example, the amplitude, the integral corrected by the local

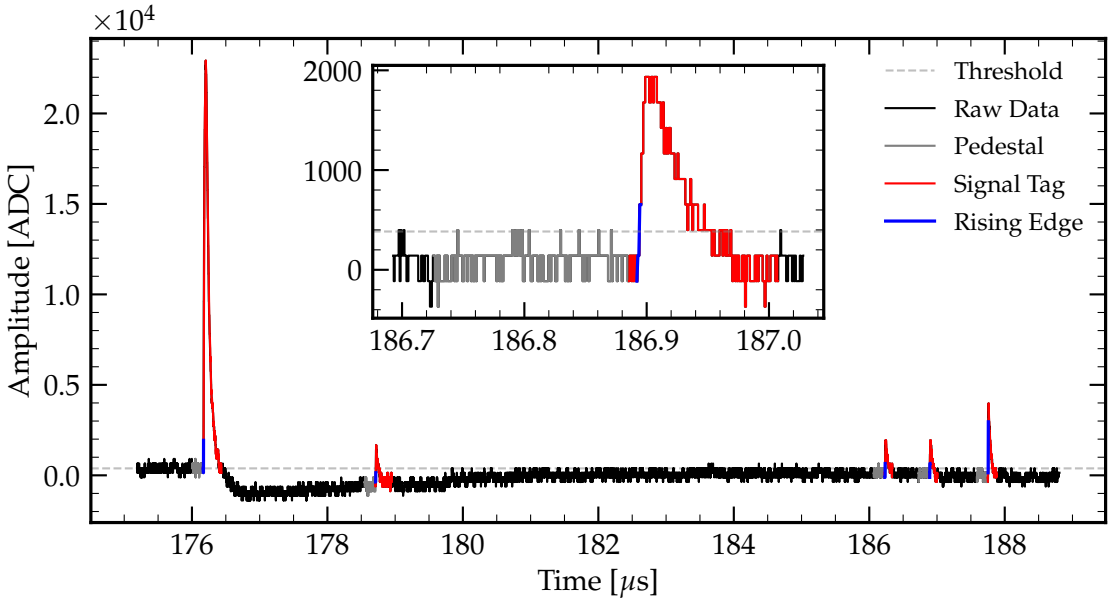

Figure 7.2: Signal identification example in a pedestal corrected raw waveform. The plot shows a cutout of a raw waveform illustrating important components of the signal identification. The data features channel Top Backward B from run 516338-0009. The axes labels of the inner plot are equal to the outer plot.

pedestal, the signal timing at a constant fraction of the amplitude and more. All relevant parameters are introduced when needed.

Fig. 7.2 illustrates the different parts of a signal in a raw waveform as recognized by the algorithm: the horizontal *Threshold* to preselect bins of interest, the characteristic *Rising Edge* each signal begins with, the *Signal Tag* which combines the intermediate steps to the finally recognized signal, and a local *Pedestal* in front of each signal which is needed to correct for short term fluctuations of the signals within the waveform. Each step is explained in more detail in the following:

1. **Find all samples above *threshold*.** The threshold is defined as

$$\text{thres} = \text{ped}_\text{g} + 1.5 \cdot s_\text{v} \tag{7.1}$$

   with ped_g as the global pedestal determined previously in Section 7.1 and $s_\text{v} = 256$ is the vertical step size in which the raw data received by the oscilloscopes is quantized. The factor of 1.5 is motivated to cover at least two sigma of the global pedestal fit as shown in Fig. 7.1. There is not much noise expected for values above. All consecutive samples with a minimum length of three samples above the threshold are directed to the next step.

2. **Find the characteristic steep *rising edge* each signal begins with.** For each array of samples above the threshold, the algorithm searches for one or more rising edges with a steep rise of more than $2.8 \cdot s_\text{v}$ within not more than seven samples. The factor of 2.8 is experimentally derived and turned out to yield

optimal results. Its non-integer value originates from the pedestals with vary from waveform to waveform. If a rising edge is found, the *signal start* is defined to be seven samples before the begin of the rising edge. Moving the begin of a signal by seven samples to earlier times ensures to include the full rising edge in the signal. With the start of the signal now identified, the analysis proceeds to the next step.

3. **Find the *signal end***. The signal end is defined as the sample whose moving average is smaller than half a vertical bin above the local pedestal. The exact condition is given as

$$\frac{1}{2n}\sum_{i=j-n}^{j+n} c_i \quad < \quad ped_l + \frac{1}{2}\cdot s_v \tag{7.2}$$

with $n = 5$ and c_i the amplitude of the i-th sample. The local pedestal value of the signal ped_l is defined as the mean of the *200* samples prior to the *signal start*. The new definition of a local pedestal ensures that the full signal is tagged in the case of pedestal fluctuations as illustrated around 178.75 µs in Fig. 7.2.

7.1.3 *Signal Timing & Detector Time Resolution*

The determination of the correct timing of a signal in a waveform is accompanied with two main complications. First, the analog signals are broadened in the signal lines due to dispersion. The CLAWS setup has especially long cables of around 35 m from the detector to the readout electronics where the signals are digitized. This results in a reduction of the time resolution due to signal dispersion. Second, the oscilloscope has a finite rise time which results in an amplitude dependent rise time from the signal's baseline to its maximum. Combining this effect with the usage of a fixed amplitude threshold results in an effect called *time walk*. A large amplitude signal crosses the fixed threshold earlier than a small amplitude signal. Fig. 7.3 illustrates the procedure to compensate the time walk effect: The timing of a signal t_{sig} is determined on the steep rising edge at a threshold which is defined as a *constant fraction* of the amplitude. In the shown example, the timing of the signal at 15 % of the amplitude is 1.6 ns earlier compared to the timing at 50 %. This time difference increases further with the signal's amplitude. However, a fixed constant fraction value of e.g. 15 % over all signal amplitudes gives reasonable results as shown later in the *Detector Time Resolution* paragraph in this section. But, previous to that a sampling time drift correction issued by the oscilloscopes is presented.

SAMPLING TIME DRIFT CORRECTION Most of the waveforms recorded in Phase 2 are of 5 ms length. This corresponds to 6 250 000 continuously recorded samples at a

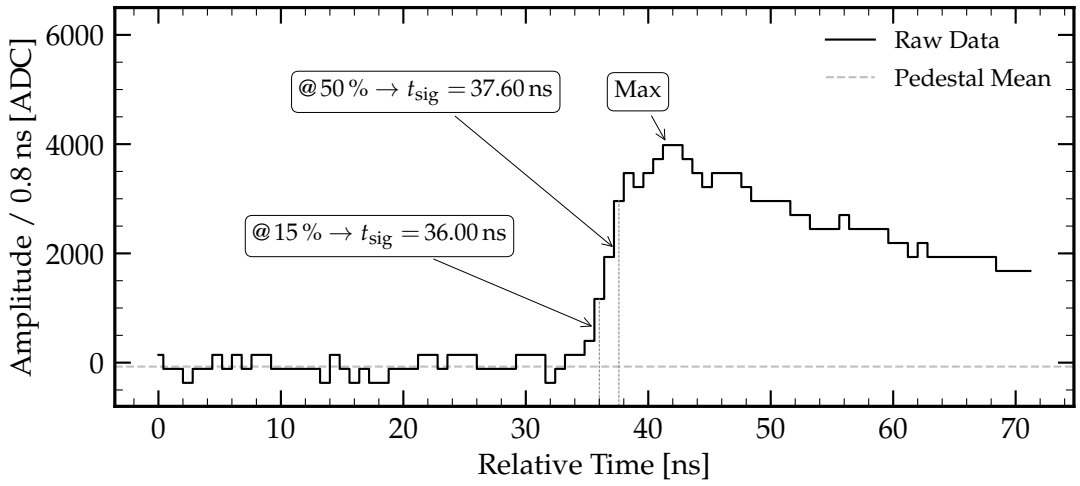

Figure 7.3: Signal timing determination in a waveform using different constant fractions of the maximum amplitude as threshold. The signal is taken from run 516338-0009 channel Top Backward B around $t = 187.75\,\mu s$.

sampling rate of 1.25 GHz. The manufacturer of the oscilloscopes states a time base accuracy of ± 2 ppm corresponding to a drift of $\pm 2\,ns/ms$. In order to analyse single particle bunches over hundreds of revolutions around one of the main rings, the time resolution must be better than the bunch spacing time of $T_{bunch} = 3.930\,ns$. Therefore an analysis of the oscilloscope specific time drift is performed to correct the timing of signals within a waveform. The procedure is described in the following.

The basic idea of the time drift correction is a comparison of the oscilloscope's internal clock to a more precise clock. The revolution time of the collider serves as an excellent clock and the noisy injection bunches offer a repeating signal which is used for the correction. Therefore, we introduce a new parameter t_{turn} referred to as *time in turn*. It is defined for each signal in a waveform as the signal arrival time modulo the revolution time of the collider:

$$t_{turn} = t_{sig} \bmod T_{rev} \tag{7.3}$$

with t_{sig} as the signal arrival time in a raw waveform and $T_{rev} = 10.0614\,\mu s$.

Fig. 7.4 (left) illustrates a scatter plot of the signal arrival time of all signals found in a single waveform versus their time in turn. The horizontal black line of data points around 5 µs are the injection induced signals while the other data points emerge from circulating bunches and appear to be randomly distributed. Horizontal data-point-free gaps are visible around time in turn values of 1.75 µs, 4.25 µs, 7 µs and 9.25 µs. Their origins may have various reasons. Possible sources are empty RF buckets as beam abort gaps, the current bunch filling scheme or, for the less prominent ones, a low bunch charge. Unfortunately, information such as the fill pattern was not available for this analysis.

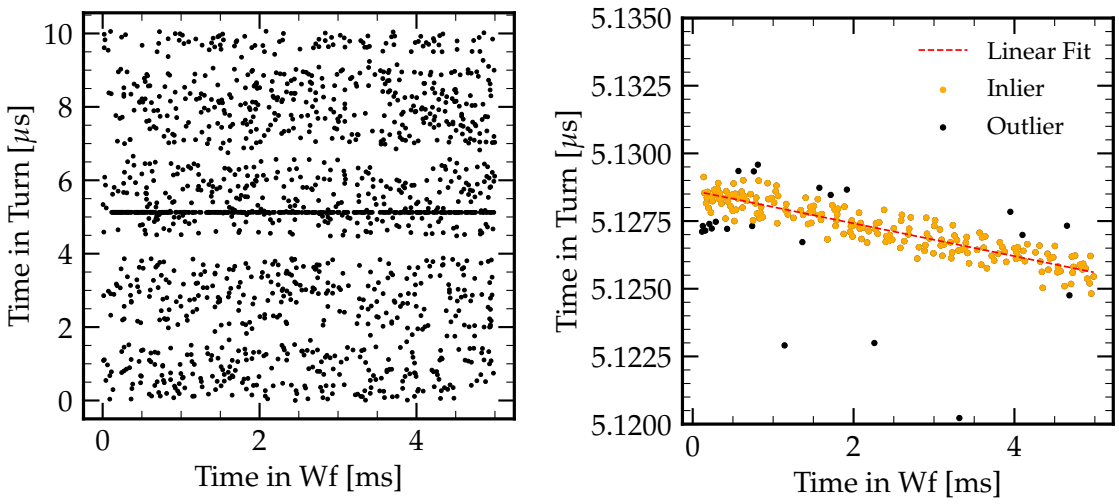

Figure 7.4: Time drift correction plots. The two plots show the same waveform (run 516368-0143) of channel Top Forward A. *(left)* depicts a scatter plot of the raw data. *(right)* shows a scatter plot of the data after the selection process and a linear fit of the form $f(x) = m \cdot x + b$ over a very narrow interval in the time in turn. The fit result is $m = (-0.605 \pm 0.019)\,\mathrm{ns/ms}$ and $b = (5.129 \pm 0.000)\,\mu\mathrm{s}$.

Without systematic effects the horizontal line of injection induced data points has no slope at all. However, the sampling time drift exists and appears as the slope of the injection induced data points as shown in Fig. 7.4 (right). But before discussing the results we have a look on the procedure of getting these.

In order to apply a robust linear fit only relevant data points should be taken into account. For this reason two cuts are applied on the data. The first one limits the time in turn variable to $5.000\,\mu\mathrm{s} < t_{\mathrm{turn}} < 5.275\,\mu\mathrm{s}$. This cut is reasonable, since all waveforms are synchronized by the injection trigger and, therefore, the horizontal line of injection induced data points appears always around time in turn values within these limits. The second cut is performed on the maximum amplitude of the signal $max_{\mathrm{sig}} > 1300\,\mathrm{ADC}$. This is the equivalent of 20 mV since injection induced signals are expected to have a much larger amplitude than those induced by circulating bunches. The two cuts reduce the number of outliers to a high degree, already. Nonetheless, there are sufficiently many remaining outliers disturbing the fit. For this reason, the *Random Sample Consensus (Ransac)* [88] algorithm is used to further remove non-relevant data points. Ransac is an iterative algorithm for the robust estimation of parameters from a subset of inliers from the complete data set [88]. Fig. 7.4 (right) illustrates the results of the applied cuts and the predictions of the Ransac algorithm together with the final fit on a smaller vertical scale. The same plot without zoom showing the complete data set after the application of the cuts is available in Fig. C.1. The slope of the linear function given with $f(x) = m \cdot x + b$ represents the sampling time drift in nanoseconds per continuously recorded millisecond. The linear fit result of $m = (-0.605 \pm 0.019)\,\mathrm{ns/ms}$ is within the accuracy given by the manufacturer.

This procedure is performed for each oscilloscope for more than 360 000 runs and filled into a histogram. Fig. 7.5 presents the distributions of the sampling drift time per oscilloscope. A further separation into the single channels is not needed since each oscilloscope has one global clock shared by all channels. Plots featuring the drift time per channel are available in Appendix C in Fig. C.3. The two oscilloscopes Bottom Backward and Top Forward show a very similar distribution around $-0.6\,\mathrm{ns/ms}$ while the Bottom Forward distribution is slightly shifted to more negative sampling time drifts. The distribution of the oscilloscope Top Forward shows the smallest absolute drift. In absolute values the results of the Gaussian likelihood maximization are $\mu_{\mathrm{BB}} = -0.597\,\mathrm{ns/ms}$ and $\sigma_{\mathrm{BB}} = 0.073\,\mathrm{ns/ms}$ for Bottom Backward, $\mu_{\mathrm{BF}} = -0.677\,\mathrm{ns/ms}$ and $\sigma_{\mathrm{BF}} = 0.069\,\mathrm{ns/ms}$ for Bottom Forward, $\mu_{\mathrm{TB}} = -0.251\,\mathrm{ns/ms}$ and $\sigma_{\mathrm{TB}} = 0.088\,\mathrm{ns/ms}$ for Top Backward, and $\mu_{\mathrm{TF}} = -0.594\,\mathrm{ns/ms}$ and $\sigma_{\mathrm{TF}} = 0.074\,\mathrm{ns/ms}$ for the Top Forward oscilloscope. Plots of the same data including the fit and detailed results are available in Appendix C in Fig. C.2.

The results show that for each oscilloscope the observed sampling time accuracy is within the range stated by the manufacturer. Finally, all signals are corrected depending on the recording oscilloscope and location in the waveform.

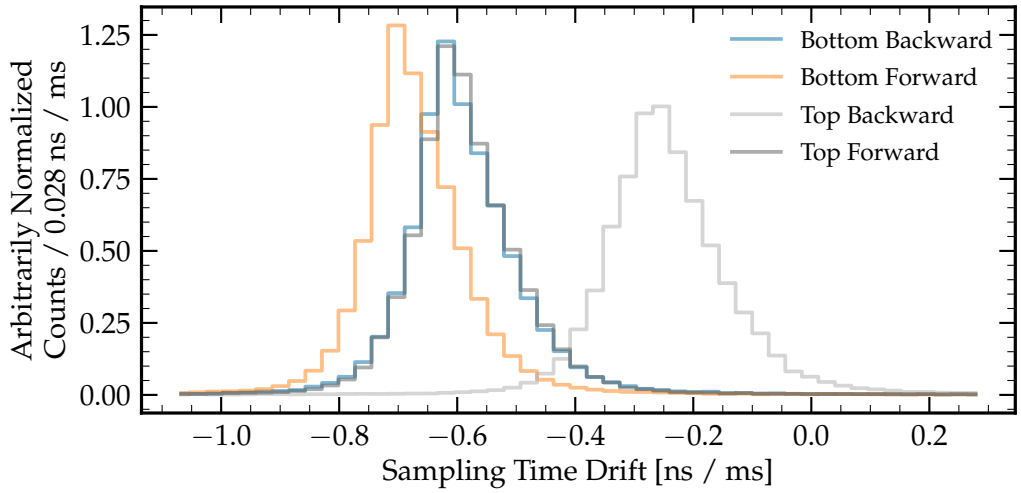

Figure 7.5: Sampling time drift correction histograms for all oscilloscopes. Plot resolving each channel per oscilloscope are illustrated in Appendix C in Fig. C.3.

DETECTOR TIME RESOLUTION The detector time resolution is a system specific resolution of the entire CLAWS system. It includes all parts of the system, beginning with the signal creation in the SiPMs over the active dock box a few meters away from the detector ladders and over the 35 m cables to the digitizer in the electronics hut outside of the radiation area. In the CLAWS detector, the signal observation is a stochastic process: MIPs deposit energy in the scintillator tile which is ultimately transformed to photons and subsequently detected or in other words *counted* by the SiPM. For such a process, the formula describing the energy dependent time resolution is taken from [89] and given by

$$\sigma = \sqrt{\left(\frac{A}{\sqrt{E}}\right)^2 + \left(\frac{B}{E}\right)^2 + C^2}, \tag{7.4}$$

with A as the stochastic term contributing with the inverse square root of the number of observed photons which is equivalent to the energy deposition. B is the noise contribution which scales with the inverse of the energy to the resolution. The constant term C includes, for example, influences of inhomogeneities in the detector material and contributes energy-independent to the resolution.

Fig. 7.6 illustrates the energy-dependent time resolution of the full CLAWS Phase 2 system. For each data point, the residual time between the recorded time in turn and the ideal time in turn given by the linear fit (c.f. Fig. 7.4) of all signals within a defined energy range are put into a histogram. Subsequently a Gaussian fit is used to extract the resolution. The single histograms including the fit for each energy range is given in Figs. C.9 to C.18. Fig. 7.6 (left) focuses on low energies of up to 30 MIP with a fit of Eq. (7.4). The drawn data points are well described by the model as the small errors indicate. At signal energies of 10 MIP the time resolution is at around 350 ps and improves with increasing energies to (317 ± 4) ps at 30 MIP.

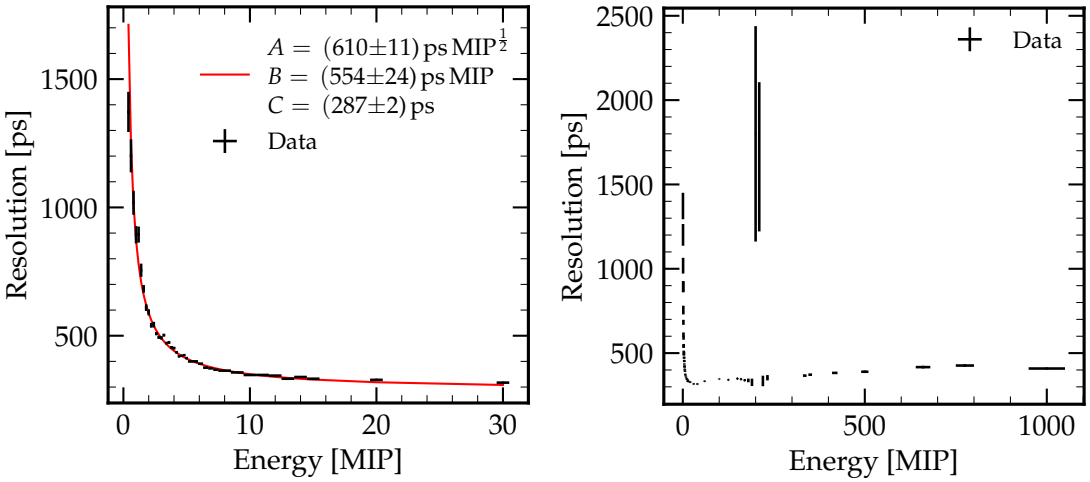

Figure 7.6: Energy dependent time resolution of the Phase 2 detector. The data includes all 16 channels of the Phase 2 detector. *(left)* Low energy resolution with data fit of Eq. (7.4). *(right)* Resolution for all energies.

Fig. 7.6 (right) illustrates the detector time resolution for all energies. At energies beyond 30 MIP the time resolution worsens to around 400 ps for energies up to 1000 MIP with two outliers at around 200 MIP. The worsening of the resolution is explained by saturation effects of the SiPM and other readout electronics. For example, 1 MIP corresponds to around 27 simultaneous exited pixels on a single SiPM. At 40 MIP this makes 1080 or 40.5 % excited pixels of one SiPM. In other words, not every photon which hits a pixel excites it since the pixel was just excited. From this hit energy level on, however, there are sufficient photons emitted by the scintillator material that a reasonable amount of photons survive to excited the just relaxed pixels once more. This behavior results in elongated signals distorting the signal shape and affects therefore also the signal timing. The reason for the two outliers is a different one, though: The mean of the residual time histogram wanders around zero (c.f. Figs. C.9 to C.18 in Appendix C). At around 200 MIP, there seems to be a binary response resulting in two Gaussian distributions, one with a positive and the other with a negative mean. The single Gaussian fit on that double Gaussian distribution results in the observable low resolution. Finding the exact reason for the described response is beyond this thesis. However, this interesting behavior is illustrated in Appendix C in Fig. C.19.

In summary, despite the dispersion of the analog signals in the long transmission line from the detector modules to the DAQ, the Claws systems shows a remarkable time resolution for energies up to 30 MIP and still a good resolution beyond that energy. Therefore, Claws system has demonstrated its sub-nanosecond timing capabilities with real experiment data.

7.1.4 *LER & HER Injection Separation*

One of the goals of this analysis chapter is to study the injection induced behavior for each of the two rings separately. Therefore, a good classification of HER and LER injections is the basis for a reliable analysis. Unfortunately, the database archiving the meta data broke down in mid May and lost all of its data. The new database replacing the broken system is operational since May 25, 2018. All meta data prior to that date is absent. In addition, the quality of the meta data is suboptimal. One reason for this is the lagging update rate of the EPICS PVs indicating in which main ring particle injections happened. This way *non-injections* have been labeled as *injections* from HER or LER and vice versa. However, since in Phase 2 injections in one or both main rings usually extend over a time period of several tens of seconds, the wrong assignment of injection and non-injection labels are relevant for only a few events. Another labeling issue affecting much more events occurred during alternating injections into the LER and HER rings. During such injections schemes, waveforms have been labeled as both LER and HER injection.

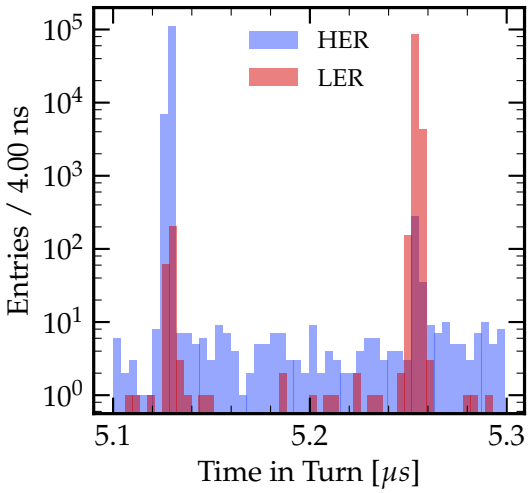

Figure 7.7: Status quo of the LER and HER injection classification. The x-axis range is chosen to include the LER and HER peaks.

Fig. 7.7 illustrates a histogram of the time in turn of the injection bunch at $t = 0$ in the waveform which is given by the constant part of the linear fit of the previous section. The color-coding corresponds to the meta data information and signifies into which ring was injected. Each peak shows a significant affiliation to one of the main rings, but also highlights a low number of mixed tags. The observed time difference between the two peaks mirrors the different arrival times of the injected bunches at the IP with respect to the injection trigger signal. This is reasonable since each ring has its own injection line between the linac and main ring.

Fig. 7.8 depicts the data around the peaks of Fig. 7.7 with a finer binning and one plot for each peak, LER (left) and HER (right). With respect to the injection trigger signal, the HER injection bunch arrives around 125 ns earlier at the IP than the injection bunch of the LER. Both rings show a similar uncertainty of $\sigma_{\text{LER}} = (0.81 \pm 0.02)$ ns for LER and $\sigma_{\text{HER}} = (0.72 \pm 0.01)$ ns for HER. These results do not only show that the classification of the source of the injection background can be estimated absolute. For the remaining part of this chapter, these results are used to classify LER and HER injections with a high reliability. All runs with an injection bunch arrival time within $b = \mu \pm 3 \cdot \sigma$ are defined as injection waveform of the corresponding main ring.

7.1.5 *Energy Calibration*

For the energy calibration we are interested in the most probable detector response of a single MIP. But in contrast to the detector calibration as presented in Section 5.5, electrons and positrons escaping from the beam are used as MIPs.

The energy of a signal is given by its integral from *signal start* until *signal end* as identified in Section 7.1.2. Fig. 7.9 shows two histograms of the same data in different representations. Each histogram is filled with all signals found in injection

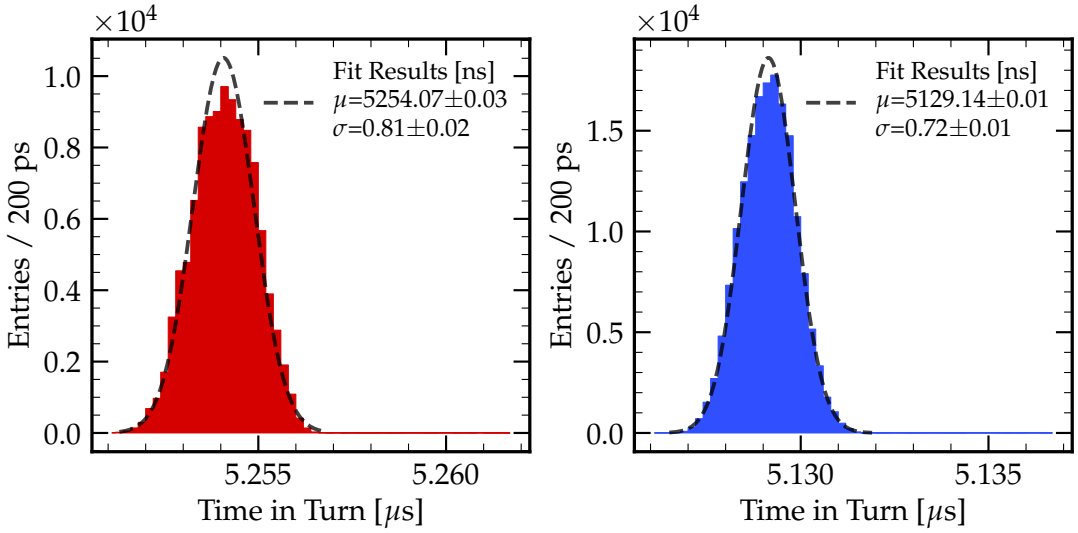

Figure 7.8: LER and HER injection classification fits on the *(left)* and *(right)*, respectively. The fits use a Gaussian distribution and have been applied using SciPy's *curve_fit* method [87].

and non-injection waveforms in the Phase 2 raw data. In total 1 648 133 007 signals have been identified.

Fig. 7.9 (left) illustrates a histogram of the raw integrals with a linear axis scale and focus on lower energies. The data follows a convolution of a Landau and a Gaussian distribution. The application of a Landau Gaussian convolution fit following the entire distribution was not successful. As an approximation, a Gaussian fit around the highest bin determines the mode of the underlying distribution. The fit result of $\mathrm{MPV} = (622.43 \pm 0.80)$ ADC s. is defined as the most probable detector response of a MIP and used as the energy normalization factor.

Fig. 7.9 (right) depicts the same data normalized to the hit rate per active detector area on the vertical scale and to the most probable hit response determined in Fig. 7.9 (left). The log-log scale emphasizes the long high energetic beam tail. The kink around 50 MIP originates from the finite amplitude single signals can reach due to a SiPM saturation. For signals with energies higher than that the signals grow mostly in length which distorts the underlying distribution. However, the vast majority of the signals are of energies less than 50 MIP and the Claws system is specialized on the timing and not on the absolute energy scale.

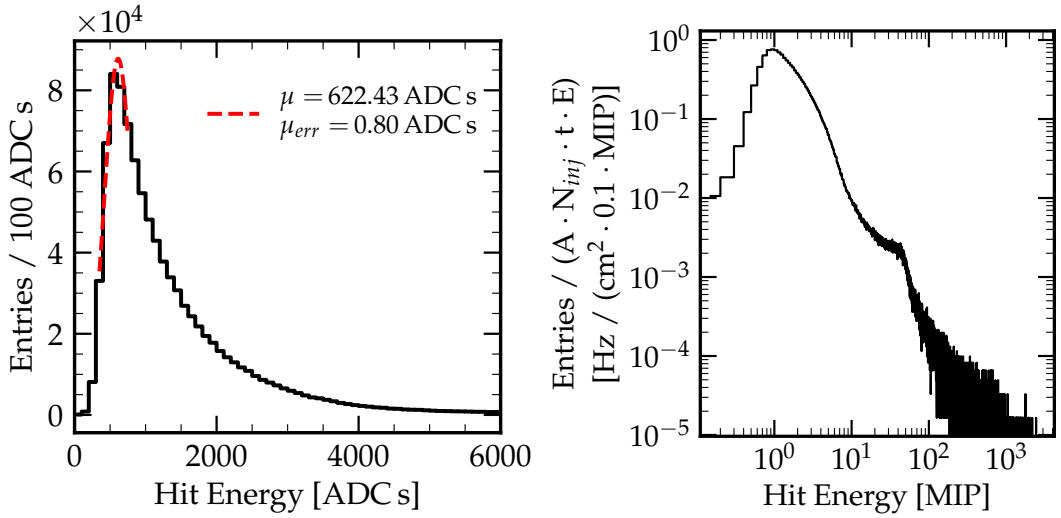

Figure 7.9: Energy calibration plots with a sub-sample of one million randomly chosen signals. Both plots show the same data in different representations. *(left)* Zoom on low energies. The Gaussian fit result is obtained using SciPy's *curve_fit* method [87]. The fit range is defined as ± 2 bins around the highest bin. *(Right)* illustrates the data in a log-log plot and with a x-axis normalized to the mode obtained in (left).

TIME STABILITY OF THE MIP RESPONSE In addition to the most probable MIP response over all of Phase 2, the MIP response stability over the course of Phase 2 enables finding hints of a possible radiation damage of the scintillator tiles or other effects.

Fig. 7.10 illustrates the most probable MIP response in time steps of two weeks over the course of Phase 2. All data points are normalized to the most probable value obtained in Fig. 7.9 (left). The data points scatter rather stable from $-3\,\%$ to $+5.5\,\%$ around the global value. However, important to note are the small vertical errors. As in the previous global fit, each data point is determined by a Gaussian fit around the mode of the Landau distribution. The vertical error bars represent the statistical uncertainty on the mean only. An additional systematic error must be taken into account. It results from the usage of a simplified approach which is able to detect larger drifts that would indicate significant degradation of the detectors. The data does not give any hints of large fluctuations of the most probable MIP response over the time of Phase 2. Besides the observation of radiation damage in the SiPMs which increased the dark rate substantially, the scintillator tiles do not show any obvious degrading.

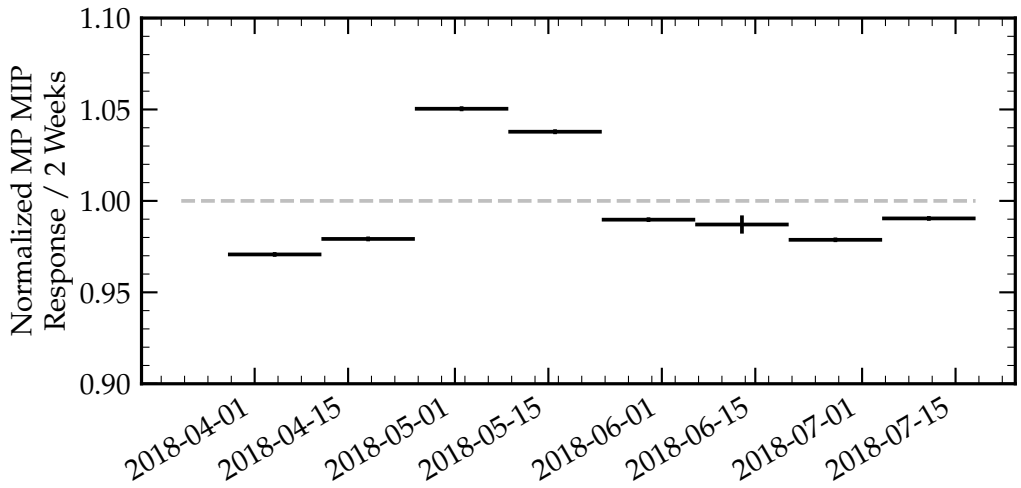

Figure 7.10: Most probable MIP response over the course of Phase 2. The dedicated fits for all time ranges are available in Appendix C in Figs. C.6 and C.7.

7.2 TIME RESOLVED ANALYSIS AROUND INJECTION BUNCH

Fig. 7.11 illustrates the time structure around the injection bunch of dedicated HER injections on July 13, 2018. Each peak originates from a circulating bunch. The peak-to-peak distance equals the bunch spacing of 12 ns which is also indicated by the red vertical lines around the injection bunch at $t = 0$. The timing used in this histogram is the mean of the signal timing t_{sig} at 15 % and 50 % of the signal's amplitude as exemplary shown in Fig. 7.3 in Section 7.1.3. Filling the histogram only with the signal timings at 15 % or 50 % of the signal's maximum leads to late or early arrivals. Fig. C.8 illustrates the original timings.

This time resolved analysis plot around the injection bunch illustrates the increased background level during the passage of the injection bunch only. The bunches adjacent to the injection bunch do not show any significant negative influence of the high background injection bunch. The energy cut demanding signals with 1.5 MIP or larger does not constrain the statements made, since the vast majority of the injection induced signals are of much higher energy as illustrated in the next section. Therefore, when discussing the injection background in the following we can assume that the injection background emerges from only one single bunch and not from multiple bunches.

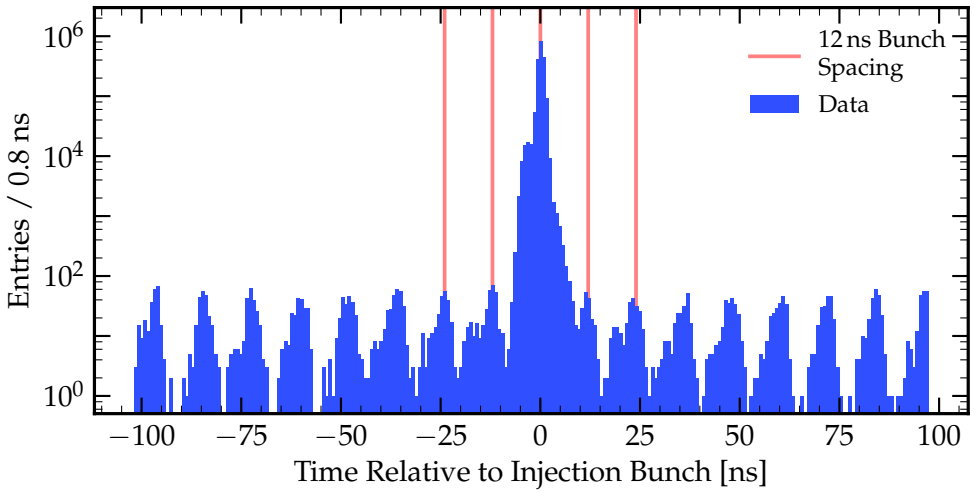

Figure 7.11: Bunch structure around the injection bunch. The vertical red lines indicate the bunch spacing of 12 ns around the injection bunch. The plot shows signals with an energy larger than 1.5 MIP only.

7.3 HIT ENERGY SPECTRA

The energy calibration of the raw data in Section 7.1.5 takes all of the raw data into account and, therefore, does not differentiate between the two main rings and mixes injections and non-injections. This section presents a time resolved hit energy spectrum over the course of a revolution and a separate hit energy spectrum for each ring differentiating injection and non-injection times during a revolution in the collider. In the following, the similarities and differences of the hit energies of the two main rings are presented in the *Common Discussion*. Afterwards, additional common and ring specific phenomena observed in the time resolved hit energy distribution are discussed in the *LER and HER Comparison*, *SiPM Afterpulses* and *Other High Energetic Structures* paragraphs. This analysis uses all raw data recorded with the injection information after May 25, 2018.

COMMON DISCUSSION Fig. 7.12 (top) and (bottom) illustrate the time resolved hit energy spectrum for the LER and HER, respectively. The 2D histograms show the time in turn on the vertical with a bin width of 102 ns and the hit energy on the horizontal axis with a bin width of 0.1 MIP. The prominent horizontal lines in Fig. 7.12 (top) and (bottom) around 5 µs contain hits emerging from the injection bunch while the remaining time bins represent regular circulating bunches. The projections of the injection and non-injection times of one revolution are illustrated in Fig. 7.12 (middle). The corresponding non-injection lines are the average of all non-injection times while the injection graphs represent the projection of the time bin containing the high background injection bunch around 5 µs. The vertical axis of Fig. 7.12 (middle) is given in entries per detector area and time.

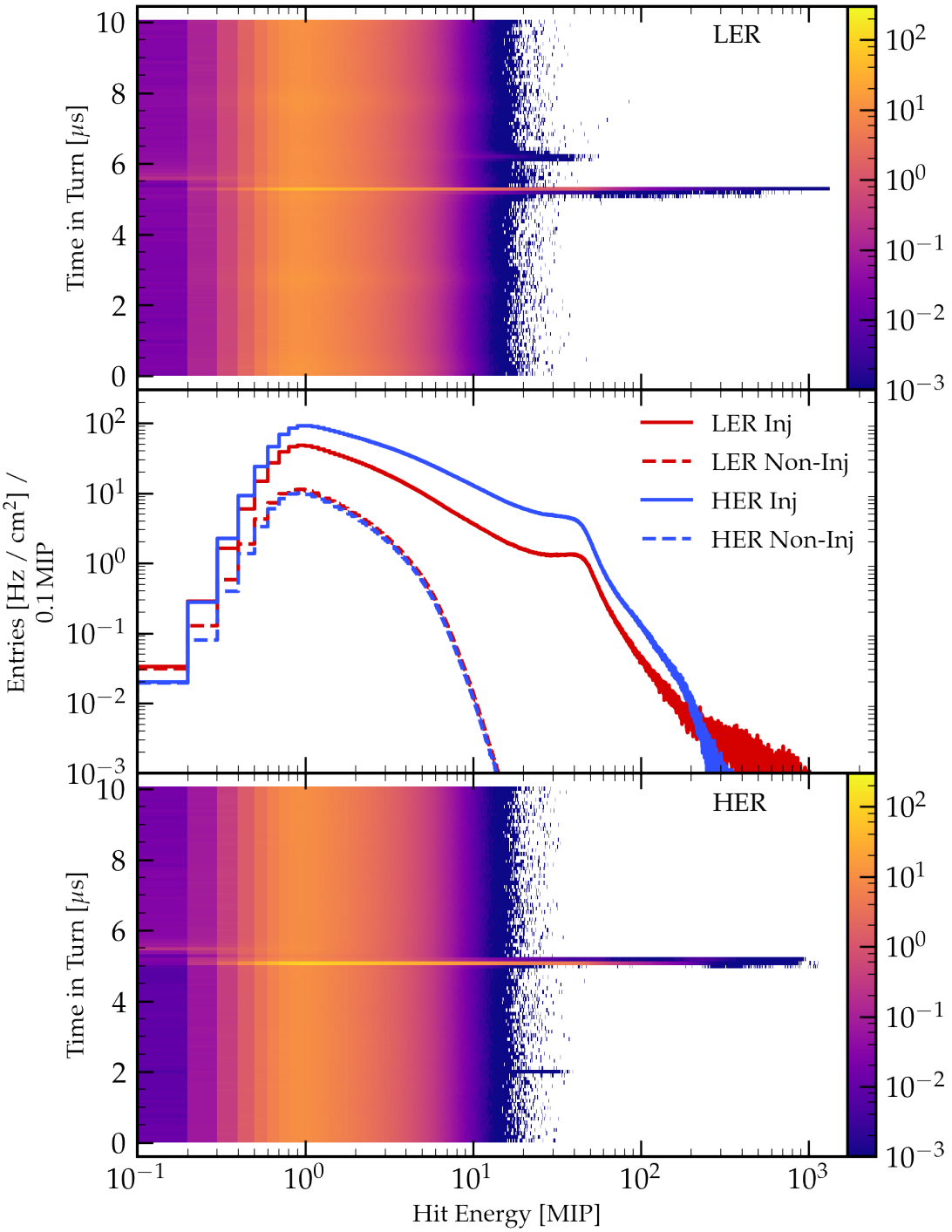

Figure 7.12: Hit energy spectra. *(top)* and *(bottom)* Time resolved hit energy spectrum of the LER and HER, respectively. *(middle)* Projection of the top and bottom plot with marginalized time in turn variable separated by injection and non-injection times of a revolution. The unit of the color bars are equal to the vertical axis of the middle plot.

The large majority of high energetic hits of >10 MIP originates from the noisy injection bunches. Their energies reach up to 1000 MIP and more. The origin of the spread of the high energetic hits over multiple time bins, as visible in Fig. 7.12 (top) and (bottom), is the ambiguity of the signal timing in the waveform as illustrated earlier in Section 7.2. For this plot, the signal timing is determined as the mean of the 15 % and 50 % constant fraction of the signal's amplitude. But not only the high energy tail is characteristic for the noisy injection bunch, also low energy hits of >1 MIP are observed up to a factor 4 more often compared to the regular circulating bunches as Fig. 7.12 (middle) shows.

LER AND HER COMPARISON The differences of the two main rings are best visible in Fig. 7.12 (middle). The HER injection bunches (*HER Inj*) cause a higher rate in the CLAWS sensors compared to the injection bunches in the LER (*LER Inj*). For hit energies from 1 MIP to 100 MIP the HER rate is with around 100 Hz/cm^2 a factor 4 higher than the respective rate from the LER. Starting at energies of >100 MIP the LER and HER injection rates converge before the order switches at an energy of around 300 MIP and the LER rate becomes larger than the HER rate. At rates of 1 mHz/cm^2 hits emerging from the injection bunches reach energies from 300 MIP to 600 MIP in the HER and 300 MIP to 1000 MIP in the LER.

For the hits emerging from non-injection bunches (*LER/HER Non-Inj*) the LER and HER show almost equal rates over all energies as illustrated in Fig. 7.12 (middle). Hits with an energy of 1 MIP appear in both rings at a rate of 10 Hz/cm^2. The slightly higher rate of the LER non-injection bunches results from on average higher beam currents in the LER compared to the HER during the time of the data taking.

SIPM AFTERPULSES Both time resolved hit energy distributions show a considerable excess around 0.3 µs past the injection induced peak for hit energies of <0.3 MIP. These are caused by SiPM intrinsic afterpulses following the high intensity injection signals. Fig. 7.13 shows the time distributions of low energetic hits for LER and HER. The first narrow peak of each distribution represents the injection bunch and the second broader peak illustrates the SiPM afterpulses. There are two main reasons for these excesses to be afterpulses. The first indication is the appearance of these low energy excesses following the high intensity injection bunches. As written in Section 5.2, afterpulses are caused by trapped charge carriers of a previous avalanche in the SiPM and are observed as delayed signals. The high intensity hits of the injection bunch excite a substantial amount of pixels of the SiPMs of which a small fraction produces afterpulses. Second, the very similar time difference between injection peak and the excess of around 330 ns for both LER and HER data. This similar distance is explained by the algorithm determining the single signals in the waveforms as described in Section 7.1.2. The idea of that excess being the result of reflections from other detectors or scaffolds has a low probability of being true: The time distance of

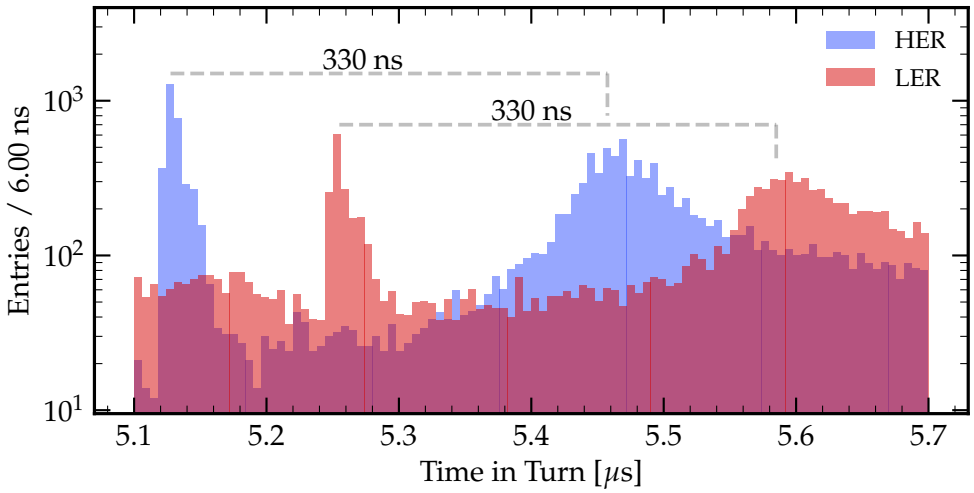

Figure 7.13: Low energy hits following the injection bunch. The data shows hits with an energy of <0.3 MIP only.

the two peaks corresponds to around 99 m[1] spatial distance resulting in a need of a reflecting obstacle around 50 m away from the IP in both FWD and BWD directions. The fact that there are lots of heavy metal parts and detectors inside of Belle 2 but none especially obvious at the give distances outside of Belle 2 reduces the probability of this theory being true by a lot.

Excluding these low energetic and not collider related signals from the analysis turned out to be difficult. Distinguishing them from the other signals is barely possible. However, their impact on the hit energy spectrum is not significant as observable in Fig. 7.12 (middle). For this reason no measures are applied against this effect.

OTHER HIGH ENERGETIC STRUCTURES More noteworthy features in the time resolved hit energy plots are signal structures of a non-injection bunch origin with an energy of >10 MIP. Such features are observed in both rings. The LER plot (Fig. 7.12 (top)) provides such an event slightly above $t_{\text{turn}} = 6\,\mu\text{s}$ and the HER plot (Fig. 7.12 (bottom)) at $t_{\text{turn}} \approx 2\,\mu\text{s}$. The origin of the structure in the HER is a single noisy bunch which appears for several turns in run 516356-0090 on July 14, 2018, at 11:56:23 JST. Unfortunately it was not possible finding the origin of this noisy bunch.

In contrast, the structure observed in the LER is much more present. It starts at low energies of <10 MIP and stretches to higher energies of up to 60 MIP. Fig. 7.14 (left) illustrates the timing of the excess signals and the injection bunch in a waveform. The structure appears only once per waveform at $(157.072 \pm 0.051)\,\mu\text{s}$ which is equal to $(897 \pm 51)\,\text{ns}$ after the fifth pass-by of the injection bunch at the IP. The large uncertainty results from the broad distribution of the excess signals. For energies of >30 MIP the signals have been observed in 93 non-consecutive runs. Fig. 7.14 (right) presents the distribution of these hits in the waveform versus the date and time of

1 For particles travelling at the speed of light.

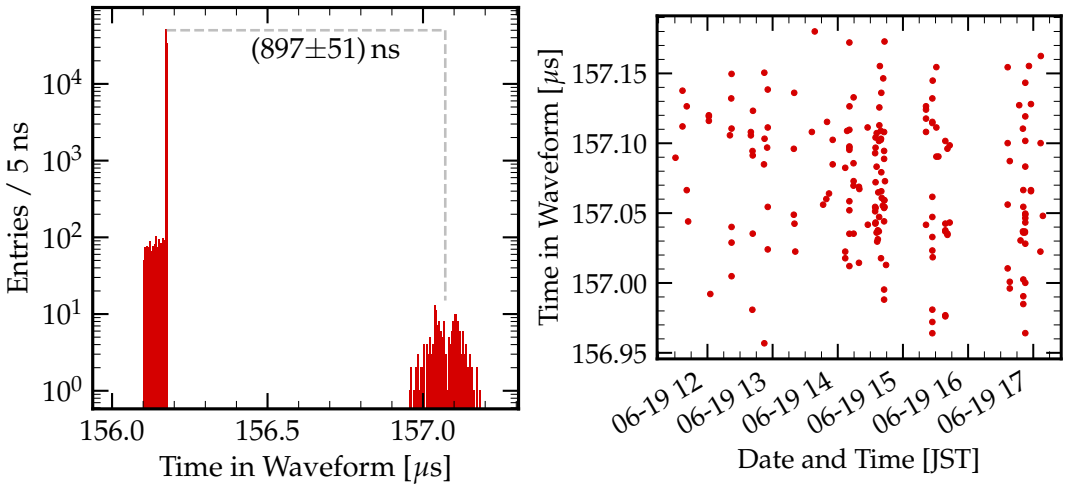

Figure 7.14: LER hit spectrum high energy excess at around $t_{\text{turn}} = 6\,\mu\text{s}$. The shown data are signals with an energy of >30 MIP. *(left)* Signal timings of the injection bunch on left and of the excess on the right. The number on the top is the time difference between the two distributions. The corresponding fits are available in Fig. C.5. *(right)* Date and Time distribution of the excess occurrences in the waveform.

their occurrences. The shown high energetic hits with >30 MIP have been observed over a time range of more than 5 h on June 19, 2018.

The origin of this excess is unknown. Nonetheless, using the observed time structure one can formulate a reasonable, but yet not verified, explanation which includes the positron damping ring: The time difference of the excess signals to the last pass-by of the injection bunch is within its uncertainty two times the revolution time of the LER damping ring with $T_{\text{rev; DR}} = 135\,\text{m}/c = 450.3\,\text{ns}$. This could be a hint of a late injection with a delay of

$$t_{\text{delay}} = 4 \cdot T_{\text{rev}} + 2 \cdot T_{\text{rev; DR}} = 41.146\,\mu\text{s} \tag{7.5}$$

with the collider revolution time T_{rev}. However, the wide spread of the excess is untypical for injections and would require additional malfunctions of the injection system. Unfortunately, it was not possible to identify the true origin of this excess in the scope of this thesis. But, the usage of CLAWS as a beam monitoring system provides a great tool to follow up on on that later.

7.4 TIME DEVELOPMENT & RECURRING PATTERNS OF THE INJECTION INDUCED BACKGROUND

As shown earlier in the *Fast Reconstruction* in Section 6.2 the time and energy calibrated signal information can be used to create reconstructed injection waveforms. In this section the reconstructed waveforms are averaged per main ring over all recorded runs between May 25, 2018, and the end of Phase 2. The waveform timing relative

to the injection trigger results in an exact overlay of the injection-induced bunches. This implies that in the overlaying process the non-injection bunches do not always match their bunch ID. For example, in the first injection the bunch with number X while in the second injection the bunch with number Y with $X \neq Y$ is topped-up. The overlaying process is aligned with respect to the injection trigger making sure that always the injection bunches overlay. For this reason, the averaged reconstructed waveforms are properly suited for a frequency analysis of the injection-induced signals.

First, the average reconstructed waveforms for each ring in two different length of 5 ms and 20 ms are analyzed with respect to the appearance of injection-induced signals. Later the 5 ms waveforms are studied in terms of their fast varying signals with two distinct analysis methods complementing each other: an autocorrelation and a discrete fourier transform.

7.4.1 *Time Development of Averaged Reconstructed Waveforms*

Fig. 7.15 depicts the average of 9004 and 11 611 reconstructed waveforms of the LER (top) and HER (bottom), respectively. The saturated colors below at the bottom of each plot represents signals emerging from the stable circulating bunches and is further emphasized by the median of the waveform represented by the grey dashed line. The faint colors above represent signals originating of the injection bunch which arrives at the IP the first time at around 0.12 ms. The rebinning by a factor of 100 to a bin width of 80 ns is applied to improve the visualization.

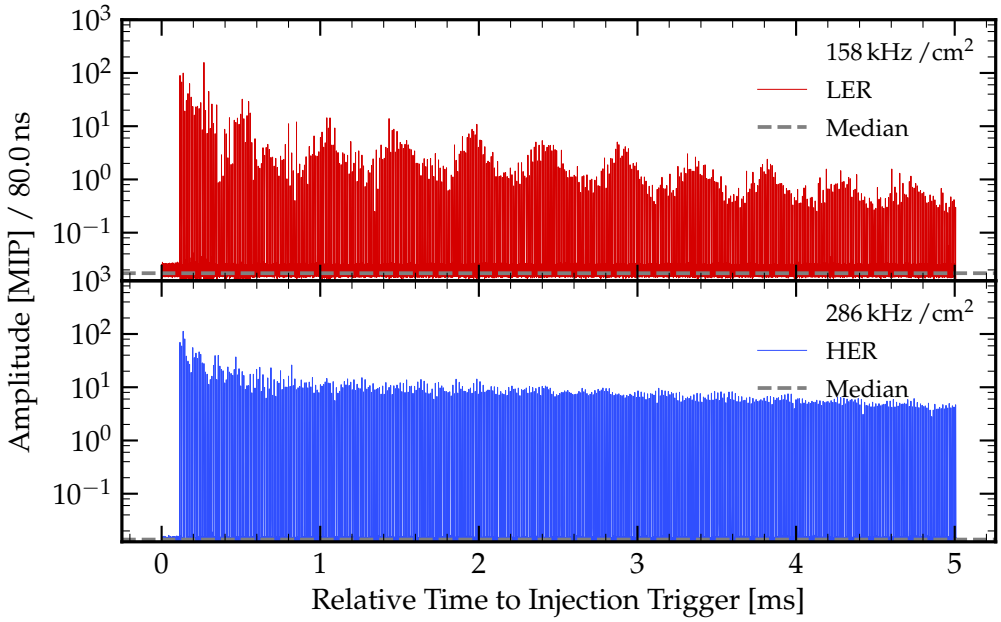

Figure 7.15: LER (top) and HER (bottom) averaged injection waveforms with a logarithmic vertical scale. The dashed grey line illustrates the median of the waveform.

The averaged reconstructed LER injection in Fig. 7.15 (top) demonstrates the intense injection induced signals starting with an amplitude of around $1 \cdot 10^2$ MIP at the beginning of the waveform and shows an oscillating pattern which results in changes of the amplitude by one order of magnitude with a period of approximately 0.5 ms. These oscillations are known as synchrotron oscillations and studied later in this section. The signal background from the circulating bunches stays rather constant of the shown time period. The bare background level without the injection induced signals is observable at the very beginning of the waveform until around 120 ns.

The HER averaged reconstructed waveform depicted in Fig. 7.15 (bottom) shows a dissimilar behavior. The injection induced signals start with an amplitude close to $1 \cdot 10^2$ MIP slightly lower than the LER, but decreases less over the course of the waveform. At the end of the data record at 5 ms, these amplitudes are with around 4 MIP a factor of 10 higher compared to the corresponding LER signals. In addition, no synchrotron oscillations are observed. The background level originating from the circulating bunches is constant, similar to the LER waveform.

For both LER and HER injection waveforms the observed time range of 5 ms is insufficient to observe the full reduction of the injection induced signals down to the level of the regular circulating bunches. For this reason a view at an extended record time is needed.

EXTENDED RECORD OF INJECTION WAVEFORMS Fig. 7.16 illustrates the average of 1464 and 1821 reconstructed waveforms of 20 ms length of the LER (top) and HER (bottom), respectively. Similar to Fig. 7.15 the waveforms are rebinned by a factor of 100.

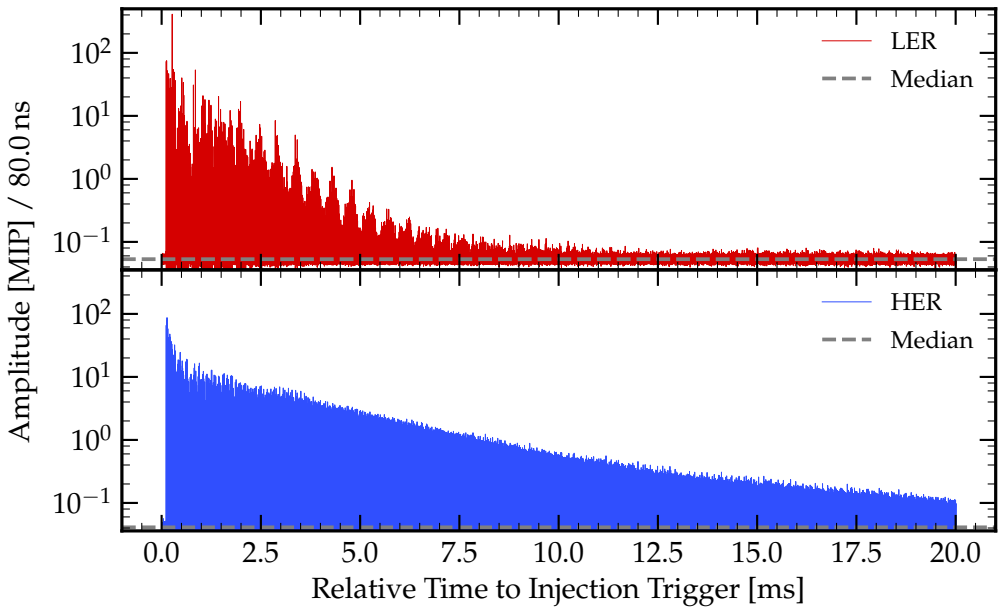

Figure 7.16: LER (top) and HER (bottom) averaged injection waveforms with a logarithmic vertical scale. The dashed grey line illustrates the median of the waveform.

Unsurprisingly the 20 ms average reconstructed waveforms of the LER and HER show a very similar behavior as their 5 ms long counterparts. For this reason the focus lies on the duration of the observable injection induced signals. The amplitude difference of the signals emerging from the circulating bunches among the 5 ms waveforms and their 20 ms counterpart results from a different average beam current at the time of the record of the data with an additional effect introduced by the larger bin sizes.

Both waveforms show mostly exponentially[2] decreasing amplitudes for the injection induced signals. Yet, the two main rings show a different behavior. For the LER waveform in Fig. 7.16 (top) it is observed that after around 11 ms to 12 ms the injection induced signals are mostly not exceeding the amplitudes of the circulating bunches anymore. However, small amplitude signals larger than the signal emerging from the circulating bunches appear until the end of the waveform. In contrast, the injection induced signals in HER waveform below do exceed the signals emerging from the circulating bunches by around a factor of 2 even at the end of the 20 ms waveform.

In conclusion the signals emerging from injection bunches decrease exponentially in amplitude. However, the behavior differs for the two rings. While the injection induced signals in the LER perform oscillations which will be analyzed in the next section in more detail, the HER signals do not show any oscillations. In addition, the LER injection induced signals vanish to large extent until 11 ms to 12 ms while in the HER these signals are observable until the end of the waveform at 20 ms with an amplitude around a factor of 2 larger than the signals of the circulating bunches. Therefore, the absolute cooling time of the HER must be $>$20 ms. The injection rate at time of the waveform record was always $\leq$12.5 Hz signifying that the injection induced signals should not have influenced each other. Nonetheless, in order to work with the design injection rate of 25 Hz into each individual ring the cooling time in the HER should improve in order to keep the injection induced background level low. However, another point one has to keep in mind is that the signals emerging from the injection bunches only appear in multiples of the revolution time which means that the high intensity signals only appear for a very narrow time range as described in detail in Section 7.2.

2 Thanks to the logarithmic vertical axis the exponential nature appears linear.

7.4.2 *Fast Varying Signals*

In both rings fast varying backgrounds are of high importance. In the following the averaged and reconstructed injection waveform of each ring as depicted in Fig. 7.15 is studied using an autocorrelation analysis and a fast fourier transformation analyzing its time dependent sub-structures. These techniques allow finding the frequencies of the betatron and synchrotron oscillations which are unique for each of the main rings. But before the analysis is presented a brief introduction of the two analysis techniques is given. Afterwards, the found frequencies and time distances of repeating patterns are studied separately for each of the main rings.

AUTOCORRELATION ANALYSIS An autocorrelation describes the correlation of a function with a delayed copy of itself. It is a tool to find repeating patterns in the function as a function of the time lag. For our discrete data sets the SciPy autocorrelation implementation *scipy.signal.correlate* with *mode='full'* [87] is used. Assuming that an autocorrelation is a less common method of analysis, we go into the details of the implementation of the algorithm:

$$z[k] = \sum_{l=0}^{||x||-1} x_l x^*_{l-k+N-1} \tag{7.6}$$

with $k \in [0, 1, ..., 2||x|| - 2]$ where $||x||$ is the length of x and $N = ||x||$. The returned function is a spectrum in the time domain of the distances between the signals weighted by the product of their corresponding magnitudes. The sensitivity of the autocorrelation ranges from the sampling time of 0.8 ns to the full waveform length of 5 ms. However, our interest focuses on possible repeating patterns of the injection bunch which produce signals in multiples of the revolution time. For this reason, the range of the horizontal axis extends from one revolution to $5\,\text{ms}/T_{\text{rev}} \approx 500$ revolutions.

DISCRET FOURIER TRANSFORM A fourier transform decomposes a time domain signal into its frequency components. The *discrete fourier transformation (DFT)* is a special case and converts a finite sequence of equally spaced samples in the time domain into a sequence of equally spaced samples in the frequency domain. The returned function has the same length as the input function. The range and resolution of the discrete frequency spectrum depends on the sampling frequency and the sample count of the discrete time domain signal. The average reconstructed waveforms have a total length of $N_s = 6\,260\,000$ at a sampling frequency of $F_s = 1.25\,\text{GHz}$ or $1/0.8\,\text{ns}$. In order to avoid aliasing, the largest detectable frequency is defined by the *Nyquist frequency*

$$f_{\mathrm{Ny}} = \frac{F_{\mathrm{s}}}{2} = 612.5\,\mathrm{MHz}. \tag{7.7}$$

Consequently, the observable frequency spectra range from 0 Hz to $f_{\mathrm{Ny}} = 612.5\,\mathrm{MHz}$ with a resolution of $\Delta f = f_{\mathrm{Ny}}/N_{\mathrm{s}} = 200\,\mathrm{Hz}$. The first bin at $f = 0\,\mathrm{Hz}$ reflects the DC component of the signal and is omitted in the discussion. [90]

The used technical implementation of the DFT is taken from the *scipy.fft* method collection [87]. Since the amplitudes of the DFT are relative magnitudes, all values are normalized by the highest amplitude.

This method of analysis, however, has some limitations when applied to the reconstructed waveform data. First, the signals in the reconstructed waveforms are not slowly growing to the maximum such as sinoids but delta functions. Second, the injection induced signals are measured only once per revolution which corresponds to a frequency of around 100 kHz. That implies that the *Nyquist frequency* of the injection induced signals is equal to $\frac{100}{2}$ kHz. This means that frequencies higher than that can in theory lead to aliasing. Due to these reasons, the results obtained by this method should be interpreted with caution. However, the following results establish concrete measurements of several quantities related to the time evolution of injection induced signals.

LER Fig. 7.17 illustrates a DFT (top) and an autocorrelation (bottom) of the averaged reconstructed LER waveform as shown earlier in this section. The first peak in the DFT at 2.2 kHz corresponds to a repeating pattern of every 45.177 revolutions in the main ring or a synchrotron tune of $|0.0221|$ which agrees within 3.9 % with the design value of 0.0213. This low frequency pattern is attributed to synchrotron oscillations of the injection bunches and is also observed in the averaged reconstructed LER waveform as well as in the autocorrelation in Fig. 7.17 (bottom). However, in the latter the first oscillation maximum of 1/2.2 kHz is suppressed. This behavior might be explained with a reduced contribution of synchrotron oscillation induced particle loss to the injection induced background in the first 45 revolutions. The next considerable peak in the DFT is at 99.44 kHz and corresponds to a repeating signal every 10.06 µs which is in agreement with the revolution time of $T_{\mathrm{rev}} = 10.0614\,\mu\mathrm{s}$. The remaining spectrum at higher frequencies is determined by multiples of the previous observed structures.

The autocorrelation plot in Fig. 7.17 (bottom) reveals a repeating structure every 13 and 15 revolutions. This corresponds with a reasonable probability to a betatron oscillation rate with a decimal place slightly above a half-integer, e.g. the design value for the LER of 45.5 oscillations per turn. A value between $13^{-1} = 0.077$ or $15^{-1} = 0.067$ above, results in appearing structures every 13 to 15 revolutions. This and other similar features have been observed in the first commissioning phase in 2016, too, and are excellently presented in [48] and [51]. However, these oscillations

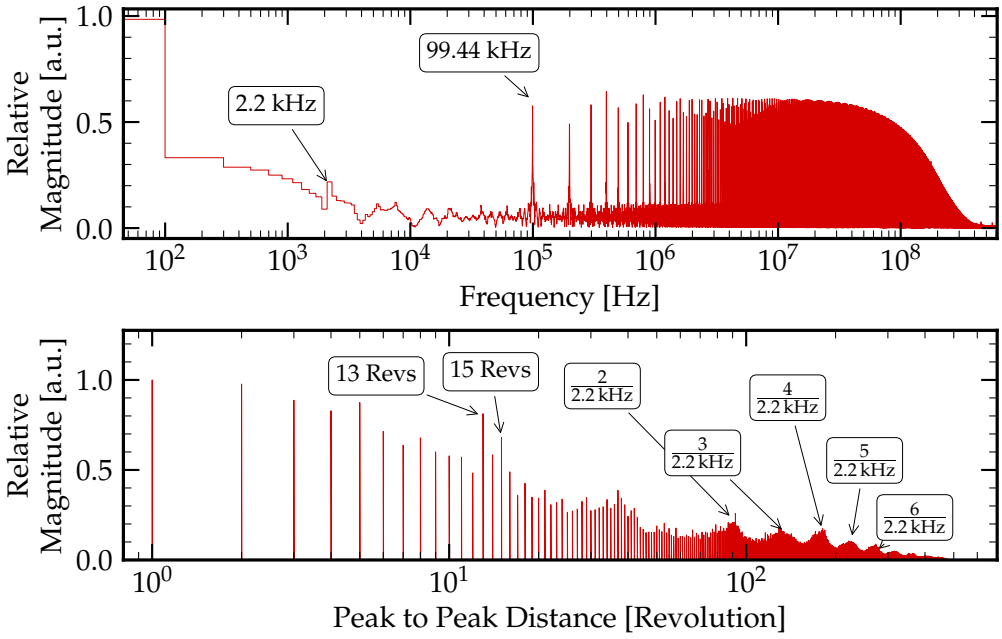

Figure 7.17: LER DFT (top) and autocorrelation (bottom) plot of the averaged reconstructed waveform. The highlighted frequencies and distances are determined using the center of the highest bin. Please note that the five annotations in *bottom* on the right are in the unit of second and must be divided by $t_{\text{turn}} = 10.0614\,\mu\text{s}$ to fit the unit of bunch revolutions in the main ring.

are not obviously visible in the averaged reconstructed waveform nor in the DFT and should therefore treated with care. The remaining highlighted oscillations in this plot are discussed in the previous paragraph.

HER The DFT and autocorrelation plots of the average reconstructed HER waveform are depicted in Fig. 7.18 (left) and (bottom), respectively. A little but reasonable local maximum at a frequency of 8.99 kHz is observed in the DFT. This frequency corresponds to a peak to peak distance of 11 revolutions which fits to the slight excess in the autocorrelation function below. This pattern is similar to the one observed in the LER and corresponds most probably to betatron oscillation rate slightly above half-integer. Nonetheless, both peaks do not stand out their surrounding continuum by a lot nor are these oscillations obviously observable in the average reconstructed HER waveform. For this reason, these results should be treated with care.

The second considerable peak in DFT plot is similar to the LER main ring at 99.44 kHz and corresponds again to the bunch revolution frequency. The remaining spectrum at higher frequencies is determined by multiples of the previous observed structures and also applies to the autocorrelation plot on Fig. 7.18 (bottom).

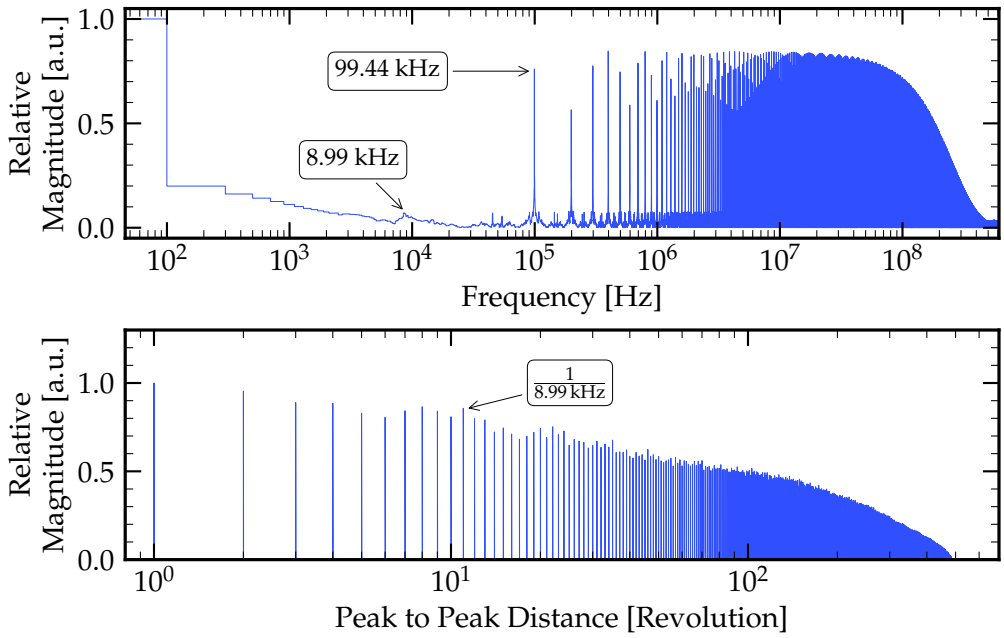

Figure 7.18: HER DFT *(top)* and autocorrelation *(bottom)* plot of the averaged reconstructed waveform. The illustrated frequencies and distances are determined using the center of the highest bin. Please note that the annotation in *(bottom)* is in the unit of second and must be divided by $t_{\text{turn}} = 10.0614\,\mu\text{s}$ to fit the unit of bunch revolutions in the main ring.

7.5 SUMMARY

This *raw data analysis* chapter begins with the preprocessing of the raw data in order to create a reliable basis for the subsequent injection waveform analysis. The preprocessing part begins with a pedestal subtraction and is followed by the signal identification of all signals in a waveform. Afterwards, the sampling time correction unveiled an oscilloscope specific sampling time drift between $-0.677\,\mathrm{ns/ms}$ to $-0.251\,\mathrm{ns/ms}$ for continuously recorded waveforms. After the correction of this time drift, the Claws system achieves a time resolution of up to $(317 \pm 4)\,\mathrm{ps}$ for signals with an energy of 30 MIP. The following LER and HER injection separation uses the time difference between injection trigger signal and the first observation of an injection bunch at the IP which is unique for each main ring. These information is of high importance and used again later in Section 8.1.2 since the meta data delivering such information is unsuitable. The last part of the preprocessing section is the energy calibration. It determines the most probable MIP response and also includes a study about the time evolution of the hit response over the course of Phase 2. It is observed that the hit response does fluctuate from $-3\,\%$ to $+5.5\,\%$ around the previous determined global energy calibration value.

The first analysis section investigates the bunch structure around the noisy injection bunch. The usage of two different timing definitions enables the direct view at the circulating bunches adjacent to the injection bunch. None of them shows any negative effects by their noisy neighboring bunches.

The following hit energy study presents separate hit spectra for times of an injection bunch and regular circulating bunch pass-by for each main ring. It is shown that particle hits in the Claws detectors with energies >11 MIP are mostly observed from the injection bunch and not from the regular circulating bunches. In addition, during injection the HER is up to a factor of four more noisy than the LER, but the LER reaches hit energies twice as high as observed in the HER. The data illustrates Claws' capabilities of detecting short and long term beam irregularities. Unfortunately, it was not possible to determine the source of these irregularities. However, there are indications of late injections into the LER over a time range of several hours.

The last section presents studies of the time evolution of injection induced signals in *average reconstructed waveforms*. Depending on the main ring and waveform duration between 1464 and 11 611 reconstructed injection waveforms are averaged over all channels creating the average reconstructed waveforms. These outcomes reveal a contrasting injection background behavior in the two main rings. The injection induced signals of the LER perform synchrotron oscillations with a frequency of 2.2 kHz and betatron oscillations between 13 and 15 oscillations per revolution before the high background fades out at around 11 ms. On the other hand, the injection induced signals of the HER do not show any significant synchrotron or betatron oscillations. Only an autocorrelation analysis unveils hint of betatron oscillations with at around

8.99 kHz. However, even after 20 ms the injection induced background in the HER is a factor of 2 above the background emerging of the regular circulating bunches.

8

FAST RECONSTRUCTED DATA ANALYSIS: COOLING TIME

One of CLAWS key features is the ability to record injection bunches over hundreds of revolutions in the collider rings. The observation starts around 107 µs before the first pass by at the IP and continues until the injection bunch becomes non-noisy anymore after multiple ms. After several hundred revolutions, the injection bunch has fully merged into the regular circulating bunch and follows the design path around the ring. The time it takes for the injection bunch to merge into the phase space of the circulating bunch is called *cooling time*.

A short cooling time is of high interest for the Belle 2 detector and especially important for the innermost detectors which are installed with only a few centimeters distance to the beam pipe. For example, high noise injection bunches can saturate the PXD and SVD which leads to a undefined behavior of the readout system. For this reason, the PXD is able to switch to the gated mode for a short time range [21]. In this mode all pixels are masked and, therefore, the increased particle rates coming from the injection bunches cannot saturate the PXD.

This chapter shows first the two preprocessing steps improving first the classification of injections and non-injections and second the classification of LER and HER injections using a parameter cuts and a decision tree, respectively. Afterwards, the cooling time of the two main rings is analyzed using multiple visual representations in combination with a correlation analysis.

8.1 PREPROCESSING

The cooling time analysis uses the fast reconstructed data as described in the *Waveform Reconstruction* in Section 6.2.2. This data is available for the whole data taking time of Phase 2 starting from March 19 until July 15, 2018. Over the period of Phase 2, the recorded waveform length has been varied as shown earlier in Table 6.1. To ensure comparability only the first 2.4 ms of each waveform have been taken into account. In addition to the reconstructed waveforms, injection related meta data from SuperKEKB such as the beam currents, injection trigger times for LER and HER and others is used in this analysis. Unfortunately, as already mentioned in Section 8.1.1, the availability of such meta data limited to past May 25, 2018, and its quality is low.

In the following, algorithms are developed to assign the correct injections labels to the waveforms. This is first done by an improved classification of injections and non-injections is presented and followed by the classification of LER and HER injections

using a decision tree. The results of this section are afterwards used to study the injection cooling time of each main ring independently.

8.1.1 *Injection & Non-Injection Classification*

The CLAWS system was triggered by two trigger sources. The first trigger source was the injection trigger signal which was distributed by SuperKEKB over a dedicated trigger line. These trigger types make up the vast majority of triggers received by CLAWS. A second trigger source was the auto-trigger by the oscilloscopes themselves. This auto-trigger was adjusted to fire every 30 s in order to keep the system responsive during injection-free times. Without the auto-trigger the oscilloscopes would wait until an injection trigger signal arrives. However, to distinguish between the two trigger types external data is required. The oscilloscopes themselves do not offer an inbuilt solution which allows to distinguish between these two trigger types.

For the vast majority of waveforms, non-injections and injections are easy to distinguish by eye. Fig. 8.1 shows a typical injection waveform (left) and a typical non-injection waveform (right). The injection waveform shows characteristic high amplitude signals at the beginning and recurring patterns over the observed time range. In contrast, the non-injection waveform shows very low amplitude signals uniformly distributed over the observed time range. In order to assess the quality of the injection label from the meta data, 100 labeled non-injections have been plotted and classified by eye. The result shows, that 88 % of the requested non-injection waveforms are in fact injection waveforms and only 12 % turned out to be non-injection waveforms. Contrarily, the injection label shows a purity of >99 % real injections. The low purity of the non-injection label is somewhat expected, since for the most of Phase 2 the recorded injection PV did not display the injection into one of the SuperKEKB main rings, but the injection gate of the linac which also serves the neighboring *Photon Factory* on the KEK area.

An improved classification of injection and non-injection waveforms is reached using the *maximal amplitude found in a waveform (MaxVal)*. Fig. 8.2 shows two histograms of the MaxVal parameter color-coded with the existing injection labels. Non-injections prevail low MaxVal values up to around 30 MIP. At higher values injections are predominant. The vertical dashed line at MaxVal = 25 MIP signifies a reasonable cut to improve the classification. Defining all waveforms with a MaxVal $\leq$ 25 MIP as non-injections and all higher values as injections yields a non-injection label purity[1] of around 90 % while the injection label purity stays similar at >99 %. These new defined injection and non-injection separation is applied to all data and used in the following analyses.

1 The purity is estimated using the same procedure as before: Plot 100 waveforms an classify injection and non-injection waveforms by eye.

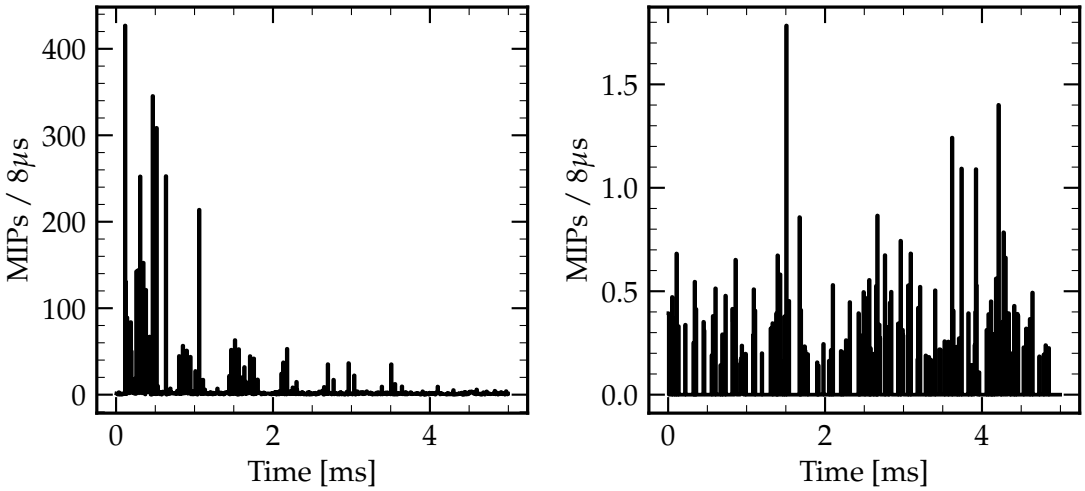

Figure 8.1: Typical injection *(left)* and non-injection *(right)* waveforms illustrating the simplicity of classifying these by eye.

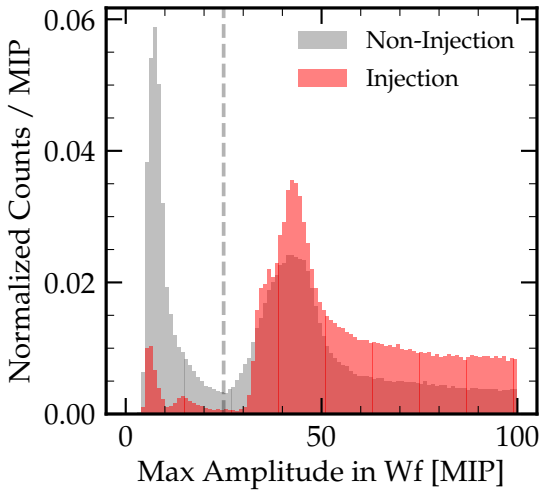

Figure 8.2: Histogram of the MaxVal (maximal amplitude found in a waveform) for injection and non-injection waveforms based on the recorded meta data labels. The vertical dashed line at MaxVal = 25 MIP defines the cut for the redefinition of injection and non-injection waveforms.

8.1.2 *LER- & HER-Injection Classification*

In the previous section, injection and non-injections are classified with high purity. In this section, we address the issue that about 60 % of all recorded injection waveforms are labeled as both LER and HER injection.

In order to separate the LER and HER injection waveforms, a *decision tree (DT)* is trained and tested for each ring on a randomly chosen data subsample of 5000 waveforms, respectively 2000 waveforms, of the data which injection source was relabeled in Section 7.1.4 based on the timing on the first signal observation after the injection trigger. The used DT implementation is the *tree.DecisionTreeClassifier* from the Sklearn Python library [88] with a maximal tree depth of four. Deeper trees did not improve the classification accuracy substantially. The trained DT is shown in Fig. 8.3. The first four columns of boxes signify data splits based on the *feature* and its *threshold* as shown in the first line. The features used by the DT are introduced below. A pairplot comparing all features is available in Fig. D.1. All described features are extracted from the same injection event and averaged over all 16 CLAWS channels.

- *MaxVal* [MIP] is the maximal amplitude found in the waveform.
- *MaxValBin* is the bin position of *MaxVal* value in the waveform.
- *C10* to *C100* are the relative bin contents of the waveform rebinned with 10 bins. E.g. *C30* returns the fraction of the total bin content observed within 480 ns to 720 ns of the waveform.
- *TimeToX* [µs] is the time until X % of the total MIP content has been observed in the waveform.

The lines below the feature line show the intermediate split results and the most right column of boxes represents the end nodes with the final DT results. If the node condition is *true* the upper path and if the condition is *false* the lower path is chosen, as indicated on the arrows. The meaning of the result lines are:

- *gini* $\in [0, 0.5]$ is a measure of the purity of the split. Gini $= 0$ signifies absolute purity while gini $= 0.5$ means equal amounts of both types. The intensity of the box color is defined by the Gini value. More saturated colors signify a high purity and therefore a small Gini value.
- *samples* represents the total amount of samples at this node.
- *value* $= [X, Y]$ indicates the absolute numbers of each type remaining at this node. Here, X represents the number of LER injections and Y the number of HER injections.
- *class* represents the currently assigned type of the node based on which type, LER or HER injection, forms the majority at this node.

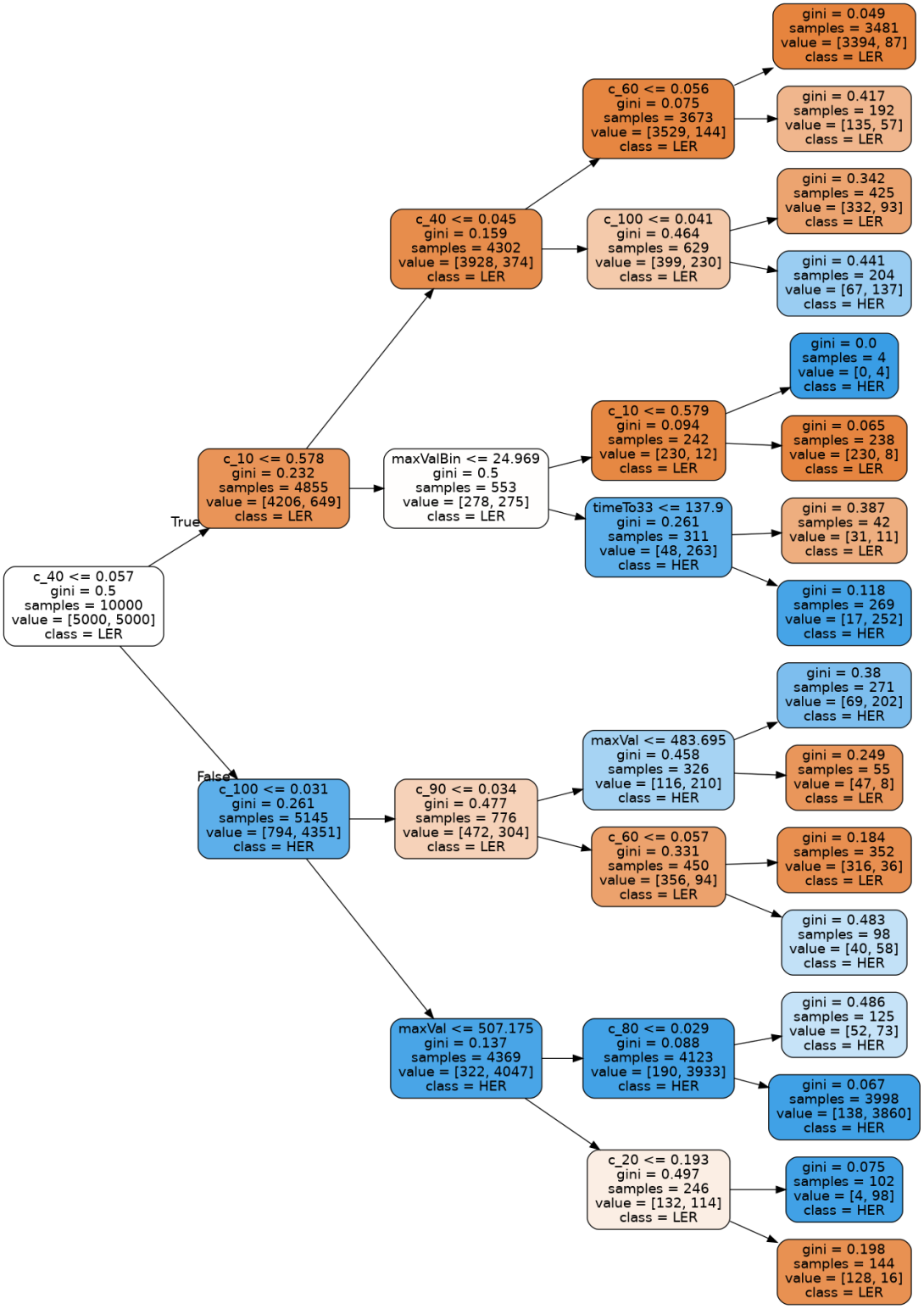

Figure 8.3: Decision tree for LER and HER-injection classification. The features here are written with lower case capital letters and the relative bin contents are written with underscore, e.g. *c_10* instead of *C10*.

DECISION TREE RESULTS The DT selected the *c_40*, *c_10*, and *c_100* as the first three nodes making them the three most significant features distinguishing a LER and HER injection. Fig. 8.4 displays KDE plots for both rings per feature. The differences in the distributions and their most probable values mirror the characteristics of each ring during particle injection.

The trained DT shows an accuracy of 91.9 % on the evaluation data. Fig. 8.5 shows the results in more detail. LER injections are correctly predicted with an accuracy of 93 % while HER injections are correctly predicted with a slightly lower accuracy of around 91 %. However, the presented outcome is assumed to be valid for data within the trained time range only. The distributions and expectation values of the features used to train the DT change over time.

However, about 60 % or 782 947 waveforms are originally labeled as both LER and HER injections. All of these waveforms are relabeled using the presented DT to infer the most probable injection background source fitting to the waveform.

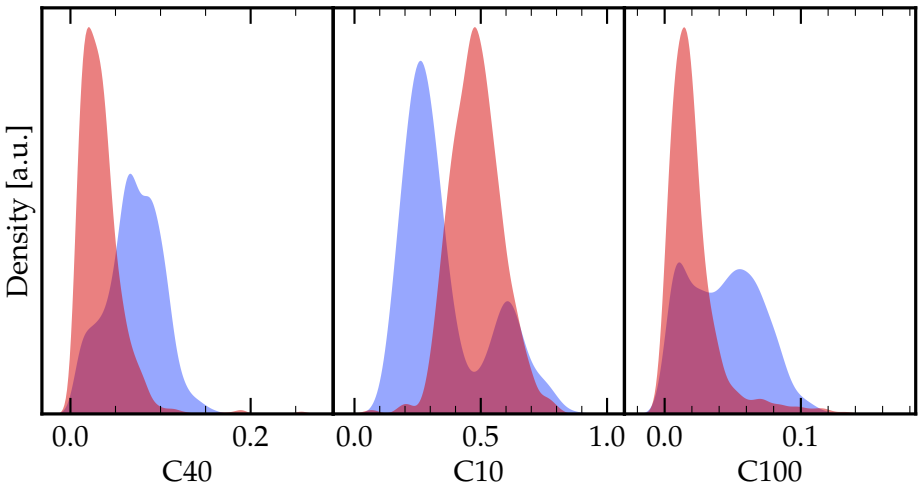

Figure 8.4: Qualitative comparison of the three most important DT features. Each plot shows a kernel density estimate (KDE) plot. The red curves represent LER and blue HER data. The KDE plots are produced with *Seaborn's kdeplot* [91].

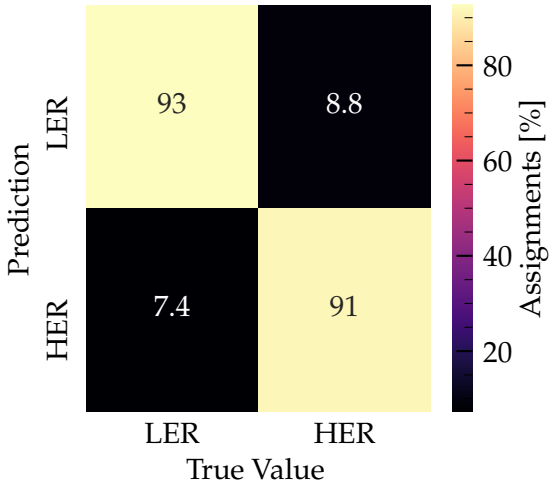

Figure 8.5: Confusion matrix of the decision tree classifying LER and HER injections. The values are given in percent.

8.2 RESULTS

Fig. 8.6 shows the cooling time over the period of Phase 2. Here, the cooling time is defined as the time until 66 % of the particle content has been observed in the waveform[2]. A *Combined* cooling time is presented from the beginning of Phase 2 until the end of May. Starting from May 25, the cooling times for LER and HER injections are separated. Each line shows the mean ± standard deviation of the central 90 % as daily average. The smallest and largest 5 % of the cooling times are neglected. These values are referred to as *Mean90* and *StdDev90*, respectively. The short gray lines above the horizontal axis show the occurrence of injection studies over the course of Phase 2.

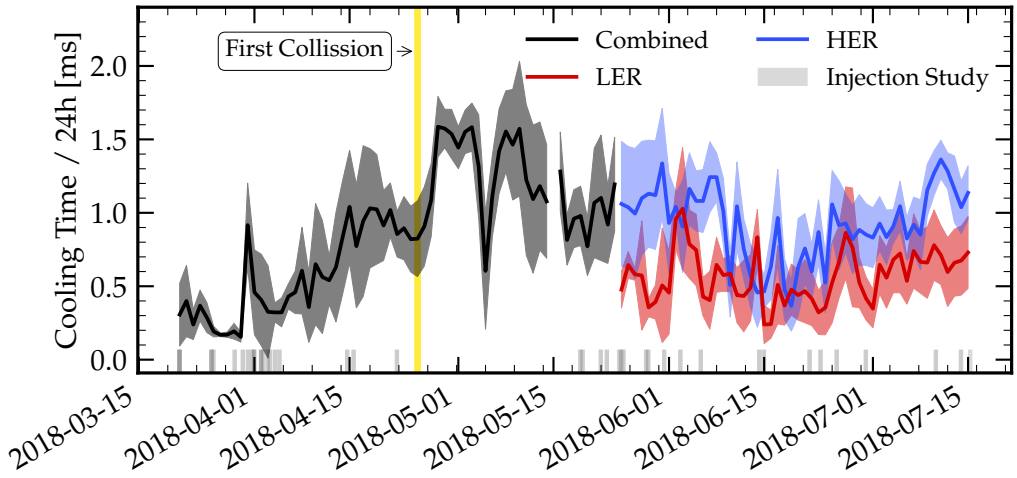

Figure 8.6: SuperKEKB cooling time in Phase 2. The cooling time is defined as time until 66 % of the particle content has been observed in the waveform. The graphs represent the Mean90 ± StdDev90 of the corresponding data source per day.

The data shows rather short cooling times at the beginning of Phase 2 which originates from very low beam currents of <15 mA in the HER only. The steep increase to up to 1 ms around March 31 is the result of a long process of reaching a stable beam in the LER. The numerous injection studies shown on the horizontal axis indicate the level of complexity of reaching this goal. After that, the cooling time increases slowly to around 1 ms. On April 25, the SuperKEKB accelerator collided the electron and positron beams for the very first time ever. Afterwards, the injection cooling time increased and reached its maximum of around 1.6 ms with a short intermediate dip down to 0.6 ms. Unfortunately, the hypothesis that increased beam currents and beam-beam effects at the IP caused the long cooling times in early May could not be proven. However, the lack of injection studies during that time suggests that the focus of the SuperKEKB staff was not explicitly on minimizing the cooling time. Starting from May 11, the cooling time decreases to around 1.2 ms before a

2 Reminder: All studied waveforms have been cut to a length of 2.4 ms.

shutdown of around 48 h stops the data taking on May 14. In the following days before the availability of the LER and HER injection labels, the cooling time fluctuates between 0.8 ms and 1.3 ms.

From May 25 onwards, the cooling times for LER and HER injections are individually calculated. The transition from the combined data set to the separate treatment of the main rings is rather continuous for the HER, but highly non-continuous for the LER. One reason for this behavior might be an over-proportional amount of HER injections prior to the transition date. However, until the end of Phase 2, the two main rings show a different behavior. While the LER cooling time mostly stays relatively flat below 1 ms, the HER cooling time shows an U-shaped pathway. The high frequency of injection studies in the second half of May and early June take effect and decrease the cooling time below 1 ms before it begins increasing more rapidly than the LER around mid June.

COOLING TIME CORRELATION ANALYSIS Fig. 8.7 shows the cooling times of LER and HER injections together with all other available injection related variables from May 25 until the end of Phase 2. The most upper plot shows the cooling time and is equal to the corresponding time range as shown in Fig. 8.6. In addition, eight more variables are plotted below. From top to bottom starting at the second plot: the fraction of data which is covered by Mean90 $\pm$ StdDev90 of the cooling time, the beam currents, the injection efficiency, the particle rate as measured by CLAWS, the injection rate, the injected charge, the betatron tunes in x and y direction, and the instant luminosity. All plots include only data at the moment of injection. As in Fig. 8.6, the plots show the Mean90 $\pm$ StdDev90 per day color-coded in red and blue for LER and HER, respectively.

The high fluctuation of the data coverage within the uncertainties in the second plot indicates large changes over the course of the day. For the shown period, the data coverage for the LER ranges mostly around 40 % to 70 %. In comparison, the HER data coverage is on average lower and fluctuates stronger between 10 % to 80 %. Drawing any conclusions about the impact of the other illustrated parameters is not trivial based on the plots only. For this reasons, the *Spearman* correlation coefficient for each parameter combination is calculated with the goal of determining high-impact parameters on the cooling time and rate during injection. The Spearman correlation is defined as

$$\mathrm{corr}(X, Y) = \frac{\mathrm{cov}(X_r, Y_r)}{\sigma_{X_r} \sigma_{Y_r}} \in [-1, 1] \,, \tag{8.1}$$

with the ranks of the variables $X_r = \mathrm{rank}(X)$ and $Y_r = \mathrm{rank}(Y)$, the covariance matrix $\mathrm{cov}(X_r, Y_r)$ of the ranks and the corresponding standard deviations σ_{X_r, Y_r}. The Spearman correlation coefficient assesses monotonic relationships and is robust against outliers. A correlation coefficient of 0 indicates no correlation, negative values

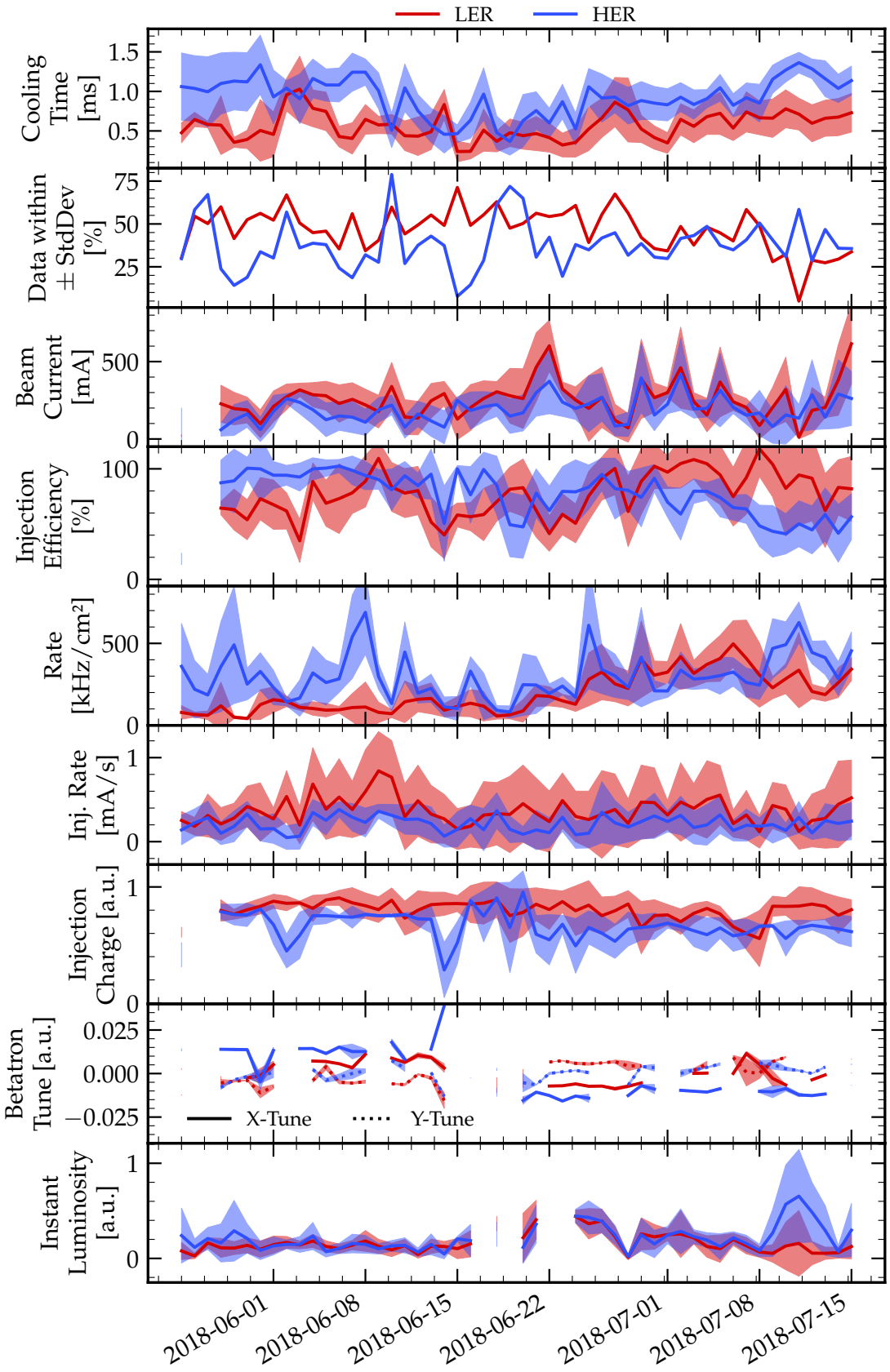

Figure 8.7: SuperKEKB cooling time versus various beam parameters at the end of Phase 2. The graphs represent the Mean90 ± StdDev90 per day. For better readability of the betatron tune plot, each data set has been subtracted by its mean value: $\bar{\beta}_{\text{x-tune; LER}} = 44.561$, $\bar{\beta}_{\text{y-tune; LER}} = 46.610$, $\bar{\beta}_{\text{x-tune; HER}} = 45.553$, $\bar{\beta}_{\text{y-tune; HER}} = 43.607$. The *Rate* is the particle rate measured by CLAWS during injection.

indicate anti-correlation and positive values indicate correlation. The higher the absolute value, the stronger the correlation between the two variables. Fig. 8.8 shows the Spearman correlation coefficients for all variables plotted in Fig. 8.7. However, assessing all correlations between all parameters is beyond the scope of this thesis. Therefore, we concentrate on the correlations with impact on the cooling time and rate observed by CLAWS during injection (*Rate* in Fig. 8.7 and Fig. 8.8).

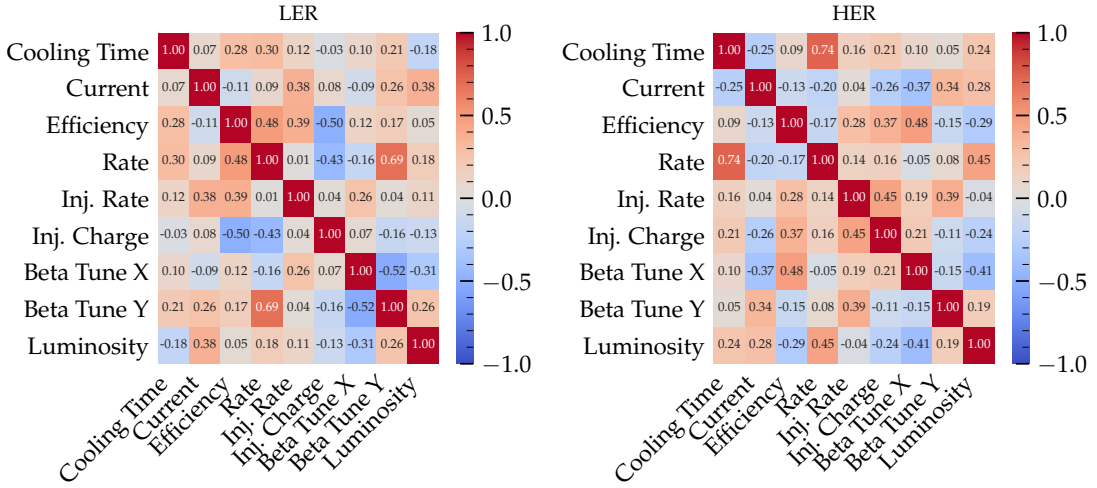

Figure 8.8: Spearman correlations of cooling time study parameters. Here the *Rate* is the particle rate measured by CLAWS during injection.

Fig. 8.8 represents the Spearman correlation coefficients of the LER (left) and HER (right). In order to assess the meaningfulness of the correlation coefficients, significance thresholds are determined simulating 1000 correlation coefficients using the bootstrap method. Here, a coefficient is defined as significant if its absolute value is equal or larger than 2σ. Two different significance levels are determined depending on the size of the data set. The betatron tune parameters with the smallest data sets are defined as significant if the correlation coefficient is $|\text{corr}| \geq 0.35$. All other parameters have a similar data set size and show a significant correlation coefficient with $|\text{corr}| \geq 0.29$. The underlying data and fits for the cut estimation are shown in Fig. D.2. Based on these significance definitions, both LER and HER cooling time correlation coefficients show significance with the rate (LER: 0.30; HER: 0.74) only.

Fig. 8.9 displays the scatter plots of the rate versus cooling time for both main rings. The linear regression lines of both plots show a clear positive correlation between rate and cooling time. However, the 95 % CIs mirror the absolute correlation coefficient. For the LER the CI is much larger compared to the CI of the HER plot. The illustrated CI even allows for a non-correlation. The HER cooling time shows a stronger correlation with the rate than the LER.

At this point we neglect the large qualitatively drawn CI of the LER in Fig. 8.9 allowing for a non-correlation between cooling time and rate. In the following, we assume that the cooling time is driven by the injection rate observed by CLAWS.

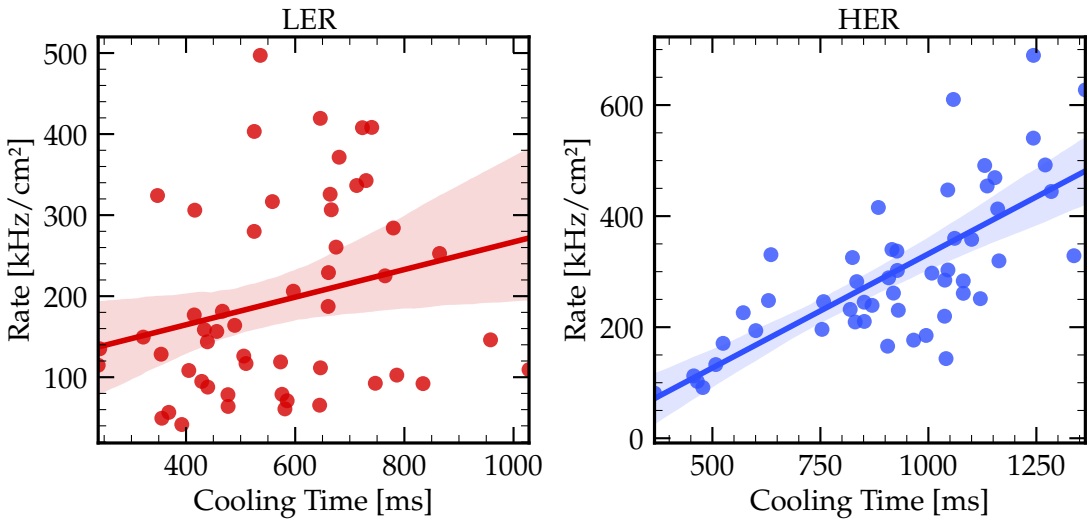

Figure 8.9: Scatter plots of cooling time study parameters showing a moderate correlation or higher versus the cooling time. The *(left)* shows LER data and the *(right)* HER data. The straight lines show a linear regression with 95 % confidence interval (CI). They are drawn as visual guide showing the qualitative trend of the data. The regression lines are drawn using *Seaborn's regplot* method [91].

THE RATE URGES THE COOLING TIME Both LER and HER cooling times and the corresponding rates at the time of injection show a positive correlation. For this reason, a more detailed view on all parameters with a significant correlation coefficient versus rate is presented in the following.

Fig. 8.10 shows the scatter plots of the mentioned parameters versus rate for each main ring. The LER injection efficiency shows a valid positive correlation. This sounds reasonable given the fact, that with a higher efficiency at injection more particles are able to escape the beam pipe to be detected. However, the same argument is not applicable for the anti-correlation between injection charge and rate. Less injected charge seems to induce a smaller rate. A possible explanation is available in the correlation coefficient of injection charge and efficiency of corr $= -0.50$. The higher the injection charge, the worse the efficiency and therefore the lower the rate and cooling time. The most bottom plot shows a strong correlation between the beta tune y parameter and the rate.

For the HER, the luminosity versus rate displays a clear positive correlation, but with a large CI. After all, one has to keep in mind, that a high luminosity is inevitable for the Belle 2 experiment and does not qualify as a parameter to decrease the injection cooling times of LER nor HER.

NOTEWORTHY CORRELATION COEFFICIENTS OF THE BEAM CURRENT In Phase 2, the beam currents of both rings have always been below 850 mA per ring. There is a long way to go reaching the design beam currents of 2.0 A, respectively 2.8 A, for LER and HER. The important role, however, of the beam current for the cooling time

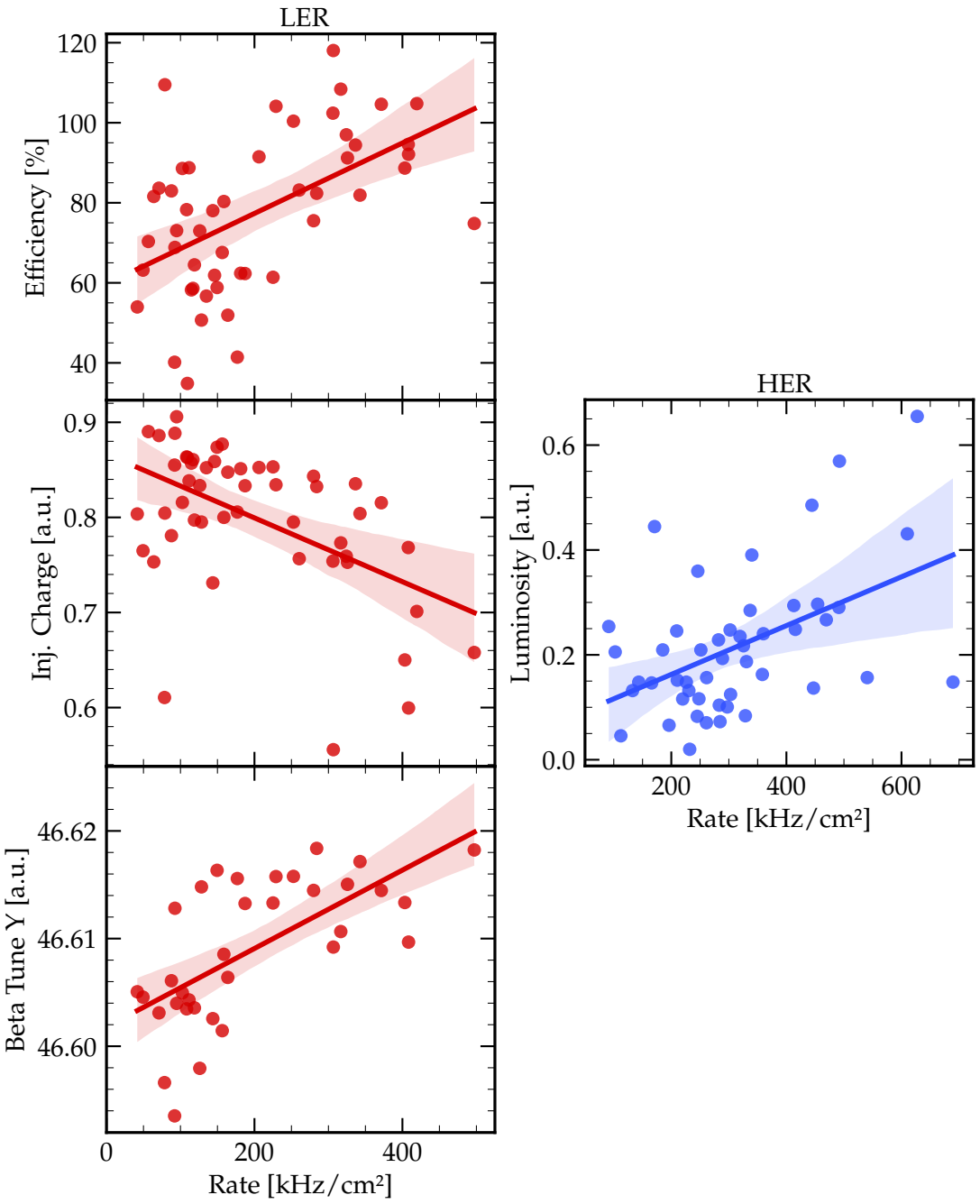

Figure 8.10: Scatter plots of cooling time study parameters showing a moderate correlation or higher versus the rate. The *(left)* shows LER data and the *(right)* HER data. The straight lines show a linear regression with 95 % confidence interval (CI). They are drawn as visual guide showing the qualitative trend of the data. The regression lines are drawn using *Seaborn's regplot* method [91].

and rate is the absent correlation with either of them. For both rings the correlation coefficient of the beam current versus rate or cooling time are with $|\text{corr}| \leq 0.25$ not significant. These non-correlations is good news since large beam currents are crucial for reaching highest instant luminosities but irrelevant for the cooling time and CLAWS injection rate.

In contrast, the beam current in the LER shows a significant correlation with the luminosity (0.38) and a high positive but not significant for the HER (0.28). This can be explained with the difficulty of finding the right steering values keeping the beams not only at a stable orbit but, in addition, having optimal parameters at the collision point in order to yield the maximal instant luminosity. The meaningfulness of the positive correlation coefficient between beam current and luminosity is explained with the proportionality between luminosity and the number of particles in each ring: $\mathcal{L} \propto N_{\text{LER}} N_{\text{HER}}$.

The LER current shows in addition a significant correlation with the injection rate (injected current into the main rings in mA/s) which is reasonable. The absent correlation for the HER current to this variable might again be explained by a lack of understanding of the beam in such an early phase of the collider usage. The HER current, on the other hand, shows a significant negative correlation (-0.37) with the beta tune y parameter.

8.3 SUMMARY

In this chapter, the cooling time evolution over the course of Phase 2 is presented and a correlation analysis of various injection parameters and their correlation among each other and especially with the cooling time and rate is demonstrated.

The basis for the presented analyses is a good separation of non-injection, LER and HER injection waveforms. There are no classification labels available from the beginning of Phase 2 at the end of March until May 25, 2018. After May 25, injection labels are available but show an insufficient classification purity. For example, querying for non-injections returns about 88 % injection waveforms. In addition, about 66 % of all injections are labeled as both LER and HER injection. For this reason, all waveforms are newly classified in Section 8.1. First, non-injections are separated from injections by applying a cut using the highest hit energy found in a waveform. This increased the purity of the non-injection label to around 90 %. Afterwards a decision tree is trained classifying LER and HER injection waveforms in the time period after May 25 using a better data set based on the analysis presented in Section 7.1.4.

In Section 8.2 a combined cooling time which does not distinguish LER and HER injections is presented until May 25. Starting from May 25, LER and HER are analyzed independently using the available injection related meta data. Using Spearmans correlation coefficients it is shown that only the particle rates during injection show

significant correlation coefficients with the cooling time in both rings. The rate, in turn, correlates significantly with different parameters depending on the main ring. The LER shows reasonable significant correlations with the injection efficiency and the betatron tune y and anti-correlation with the injection charge parameter. On the other side, the HER rate correlates with the luminosity only. The differences of the correlating parameters underlines that each ring has its own characteristics.

Another noteworthy result is the non-correlation of the beam current with the cooling time and the CLAWS rate of both rings. While the beam background coming from the circulating bunches has a linear and squared dependence of the beam current, the injection background rate and the cooling time do not show any significant influences. Over the next years the beam currents will rise to by multiple factors to their design values for the LER and HER, respectively. However, this result shows us that further increases of the cooling time or rate at the time of injection are not expected.

OUTLOOK The presented analysis shows the fundamental capabilities of CLAWS as injection monitoring system. However, this study shows only a small insight of what can be achieved. This analysis is based on only a few injection related parameters per ring. Important other injection related factors such as the energy shift of the injected bunches or the angles in horizontal and vertical direction of the septum and kicker magnets are not included here. In total 19 injection related parameters per ring have been recorded in the global database. Unfortunately, only seven of them are included in this analysis. The remaining parameters have been rejected due to a too small data set size or too many unphysical data points making the data sets unreliable.

Nonetheless, this study shows the potential of CLAWS to study the injection background in more detail. The Phase 2 data which is analyzed here is from an early stage of the experiment. At that time, a lot of services such as the archiving database have been at an early development stage making it prone to errors. Until the start of Phase 3 in early 2019, many of these issues have been improved and solved. For this reason, the data collected in the early Phase 3 starting from February 2019 until the summer shutdown offers a reasonable basis for a more comprehensive cooling time analysis.

Part IV

CONCLUDING REMARKS

9

SUMMARY, CONCLUSIONS & OUTLOOK

9.1 SUMMARY

The overall goal of this thesis was the development of a comprehensive beam monitoring system for the SuperKEKB collider with focus on the injection induced background at the Belle 2 interaction region. The main requirements are resolving single particle bunches, recording the recurring bunch signals over several revolutions, and displaying meaningful information describing the injection background situation at the IP in the Belle 2 and SuperKEKB control rooms. The update rate of the online display had to be at least 0.1 Hz. In this thesis, the development of the hard- and software of the detector system and two analyses evaluating the capabilities of the data recorded by the Claws system in Phase 2 have been discussed in detail. In the following, these two aspects are summarized.

THE CLAWS SYSTEM The detector hardware has to meet different requirements in the second and third phase of the SuperKEKB commissioning. The general detector principle of a scintillator tile read out by a SiPM remained for all phases. The Claws Phase 1 single channel modules formed the basis for the adaptation of the detector designs in the Phases 2 and 3.

Compared to Phase 1, the requirements in the second phase of the SuperKEKB commissioning changed in terms of space and intensity of the expected particle rate. For this reason, the detector geometry was redesigned to an eight channel ladder format with each an active area of $(20 \times 20 \times 3)$ mm per channel. The detector hardware was extended by a high and low gain mode increasing the dynamic range of the detector. The active dock box ensures a stable communication and signal transmission over the around 35 m of cable length between DAQ system and detector. Two Claws ladders have been mounted parallel to the beam line with a distance of 22 mm to the IP at two different angles.

In the third phase of the SuperKEKB commissioning, the requirements changed in terms of space and amount of channels. Therefore, the detector geometry changed to a single channel design with a larger size of the scintillating tile of $(30 \times 30 \times 3)$ mm. The installation effort of a single module was substantially simplified by combining all four power and support lines into a single Ethernet cable. A total of 32 modules was installed at four different locations along the beam line and four angles around the final focussing magnets.

The requirements of the DAQ software are equal for both phases and include the communication with the power supply, e.g. for powering the detector modules or switching between high and low gain mode, steering of the oscilloscopes, running a fast reconstruction on the recorded data and display the results on dedicated online monitors in the control rooms of Belle 2 and SuperKEKB. The implementation of the DAQ software was done in C++ and several external libraries have been used. The analysis software, first, recognizes single signals in the up to 100 ms long waveforms which are recorded with a sampling rate of 1.25 GHz. In the second step, the signals are calibrated to MIP using external calibration data. For each step simplified assumptions are implemented to increase the overall processing speed. In the next step, the waveforms are reconstructed and rebinned to ensure a low data load for the transmission over the network to the online monitors. The fast reconstructed data as well as the raw data can be saved redundantly as required on two different computing sites. The DAQ software is equal for the Phases 2 and 3, but the read-out hardware such as computer, oscilloscopes and power supply has been doubled in Phase 3 with respect to Phase 2.

Benchmarking the real-time capabilities of the online monitor was done using the timestamp of the fast reconstruction waveforms recorded in Phase 2. It confirms an excellent maximal update rate of $1/(1.78 \pm 0.42)\,\mathrm{s}$ for waveforms with a length of 30 ms. However, around 89 % of all recorded waveforms have been of 5 ms length or less, increasing the update rate to around 1 Hz. The performance of the Claws system is, therefore, beyond the demanded requirements. In addition, the down time of the system was limited to a single restart of the system in Phase 2.

DATA ANALYSES The analysis part is separated into two distinct analyses. The first analysis focuses on the raw data and the second one uses the fast reconstructed data as recorded by the Claws system in Phase 2.

ANALYSIS OF THE RAW DATA The analysis of the raw data recorded between May 25 and the end of Phase 2 on July 15 begins with the preprocessing including a pedestal subtraction, signal identification, and a time and energy calibration. After the identification and correction of an oscilloscope specific sampling time drift between $-0.7\,\mathrm{ns/ms}$ and $-0.3\,\mathrm{ns/ms}$ of continuously recorded data, a time resolution of $(347 \pm 2)\,\mathrm{ps}$ or better for injection induced hits of 10 MIP or higher is achieved over the full read-out chain of the Claws system. The high precision timing allowed to discriminate LER & HER injections based on their distinct arrival times at the IP with respect to the injection trigger signal. The energy calibration revealed a MIP response stability of $-3\,\%$ to $+5.5\,\%$ over the course of 3.5 month of run time.

The time resolved analysis around the injection bunch illustrates the capability of the system to resolve single bunches around the injection bunch. The result shows, that bunches adjacent to the injection bunch are not negatively influenced by the

high background injection bunches. A separate revolution time resolved hit energy spectrum of the two main rings highlights the excellent timing capabilities of the detector system. High energy hits with >10 MIP emerge almost exclusively from noisy injection bunches. While injections in the HER produce in general more background, hits emerging from injections into the LER reach higher energies of up to 1000 MIP and more. In contrast, the background rates emerging from stable circulating bunches are similar with only few differences which are attributed to the distinct beam currents over the course of Phase 2. In addition, the time resolved hit energy spectra features the system capabilities of observing single and recurring irregularities of the beam behavior precisely. In the LER, high energetic hits up to around 60 MIP have been repeatedly observed over several hours after the fifth revolution of the injection bunch. A single noisy bunch in the HER resulted in high energetic hits of around 40 MIP in a single waveform.

The time development of the injection induced signals is studied with the reconstructed injection waveforms as well as with the corresponding autocorrelation functions and discrete fourier transforms for the LER and HER. Studying the reconstructed injection waveform of the LER unveils large synchrotron oscillations corresponding to a synchrotron oscillation frequency of 2.2 kHz corresponding to a synchrotron tune of $|0.0221|$ which agrees within 3.9 % with the SuperKEKB design value. Betatron oscillations have been observed every 13 to 15 turns corresponding to a betatron tune with a decimal digit slightly larger than $1/2$ which agrees with observations from the first phase of the SuperKEKB commissioning. After around 11 ms to 12 ms the injection induced signals fade out and are not observable anymore. In contrast, the HER injection background does not show any obvious oscillation patterns. In addition, even after 20 ms the injection induced background is a factor of two larger than the signals originating from the stable circulating bunches. Injection induced signals of both main rings show an exponential decrease of the amplitudes.

ANALYSIS OF THE FAST RECONSTRUCTED DATA The fast reconstructed data was saved for each triggered waveform in Phase 2. The presented analysis uses in addition the available SuperKEKB meta data such as beam currents, injection charges, and other parameters recorded at the time of the trigger arrival. The information in which ring particles have been injected are incomplete and could not been used. The preprocessing aims at relabeling HER, LER, and non-injection waveforms. Applying a cut on the maximum amplitude found in a reconstructed waveform could improve the false positive rate of the non-injection labels from 88 % down to 10 %. For the LER and HER classification a decision tree with a depth of four was trained using the highly accurate injection label data produced in the preprocessing of the raw data analysis. A true positive rate of 93 % and 91 % for the LER & HER, respectively, is achieved.

The cooling time analysis illustrates the cooling time for the two main rings over the course of Phase 2. The impact of particle collisions on the cooling time is significant. Both cooling times show overall strong fluctuations ranging from 0.25 ms to 1.6 ms. The cooling time of both main rings shows a clear correlation with the injection background rate observed by the Claws system. Beyond this, correlations of the background rates with other LER and HER parameters have been observed. For more quantitative statements, not only more but also more reliable injection meta data would be needed.

9.2 CONCLUSION

This thesis describes in detail the development the Claws beam background monitoring system for SuperKEKB in hard- and software. In Phase 2, when particles have been guided the very first time through the Belle 2 detector, Claws was the only system visualizing the time evolution of the injection induced particle background at the IP. This detailed knowledge supported the understanding of the background conditions inside the Belle 2 detector considerably. This feature was of paramount importance especially in the first weeks when all regular Belle 2 detectors have been deliberately switched off for reason concerning the detector safety. Among all subdetectors, in particular the inner vertex detectors PXD and SVD highly benefited from the safe background environment thanks to the detailed injection background observations. The great success during this second commissioning phase lead to the request of the SuperKEKB working group if Claws could become a permanent beam monitoring system for SuperKEKB until the end of Phase 3. We complied with the request, developed a new single channel and easy to install detector module, and continued supporting the SuperKEKB working group with detailed information of the injection induced beam background behavior until the injections became sufficiently clean beyond the sensitivity of Claws.

The studies presented in this thesis demonstrate the excellent timing capabilities over extended recording times enabling detailed studies of the time evolution of the injection induced particle background. The approach of using Spearman correlations to infer a short beam cooling time based on injection related meta data shows conclusive results which motivate further studies. To unleash the full potential, using a more reliable and comprehensive data set of the injection meta data should be pursued. The capabilities of the Claws system resolving the signals emerging from single bunches in combination with the energy and intensity acceptance allow the observation of small and large scale beam irregularities with high reliability. The Claws Phase 3 system developed in the scope of this thesis creates the basis for a novel type of beam abort system which will be briefly introduced in Section 9.3.

The detector development together with the presented studies make several noteworthy contributions to advancing the understanding of injection induced background mechanisms in high luminosity lepton colliders. The observations and measurements performed by the CLAWS system provide important insights into the circulating beam and particle injection dynamics and can be used to validate simulations for the future operation of SuperKEKB reaching its final luminosity goal. The extended record time of up to 400 ms with all 32 channels enables detailed studies of the beam behavior when, for example, triggered on huge beam loss events. These studies help to improve the safety of the Belle 2 detector and general collider hardware.

9.3 OUTLOOK

The work done in this thesis is the starting point for new applications of the developed detector system. In the following, the current usage as well as a projected future project are presented.

CURRENT USAGE OF THE CLAWS PHASE 3 SYSTEM The CLAWS Phase 3 system became a permanent beam monitoring system of the SuperKEKB collider. Around Autumn 2019, the detector lost its sensitivity of observing injection induced background signals due to improvements of the particle injection process in combination with heavy metals blocking the direct view onto the beam. However, at that time huge beam loss events happened more frequently and turned out to be observable by CLAWS. Under my supervision, Ivan Popov, a master student, enhanced the DAQ system with additional hardware. He extended the system with the ability of sending trigger signals. This work will be documented in detail in [92]. The trigger fires when the combined signal of the four inner sensors exceeds a certain threshold over a defined time. The newly developed system is referred to as CLAWS *for Beam Abort* and is the second beam abort system within the Belle 2 detector. Figure 9.1 depicts the performance of the new CLAWS beam abort system with respect to the other Belle 2 internal beam abort system, the Diamond Detectors. The analyzed data was taken from October till December 2020. The CLAWS trigger settings have been applied offline on a software level and later during run time.

The summary shows that the CLAWS system would have triggered on 98.9 % of the 175 events. For 96 % or 170 events the new CLAWS beam abort system would have outperformed the Diamond abort system which relies on the integrated dose in the interaction area. On average, CLAWS would have issued the trigger around 13 µs earlier which is more than one full beam revolution. Comparing this time saving with the full post processing time of the beam abort trigger after its arrival at the SuperKEKB site of 17 µs to 30 µs, the performance improvement reaches astonishing 30 % to 43 %. In addition, the amount of false triggers (meaning that CLAWS issues

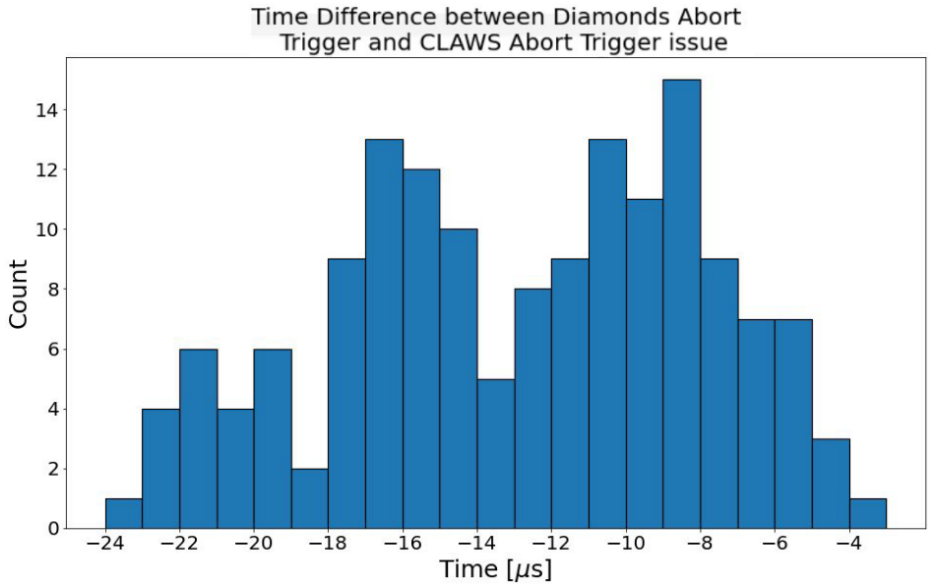

Figure 9.1: CLAWS for Beam Abort performance with respect to the existing Belle 2 internal trigger system. Taken from [93].

a trigger but the other abort system does not) is at a acceptable level and was even reduced during beam operation. The system is in operation since the end of April 2021.

An additional, yet missing, feature is a detailed offline analysis of the single beam abort events. The record of continuous waveforms with a high sampling rate of 1/800 ps over hundreds of revolutions enables a fine-grained reconstruction of the observed beam turbulences. The additional geometric information of the 32 modules which are distributed over the two final focussing magnets will support the understanding of the beam abort events in the future.

PLANNED PROJECT The high beam backgrounds as well as the huge beam loss events limit the performance of the Belle 2 experiment. In order to get a better understanding of the beam background mitigation procedures, a dedicated detector system observing the background around a collimator will be developed and installed at several collimator locations. This new system will be based on the CLAWS Phase 3 detectors and a dedicated receiver board which I developed for the advanced lab course *FOPRA Experiment 26: Silicon-based Photon Detectors in Particle Physics Experiments* [94] offered by the Future Detectors group for Bachelor and Master students of the Technische Universität München. The light-weight detector system will consist of up to four Phase 3 detector modules, a receiver board, an oscilloscope and a laptop. The dedicated power supply chip on the receiver board allows to power the detector modules by the USB outlet of a small-form-factor computer.

This system will allow to monitor the effect of e.g. different collimator settings and the overall beam background around the ring in much more detail as existing systems

can do. This will hopefully prevent a further downgrade of the ambitious luminosity goal of SuperKEKB.

Ultimately, the CLAWS system, as developed in the scope of this thesis, saves run time for physics runs and decreases the required budget for repairing work at the same time, substantially supporting the success of the Belle 2 experiment.

Part V

APPENDIX

A

EXPERIMENTAL SETUPS

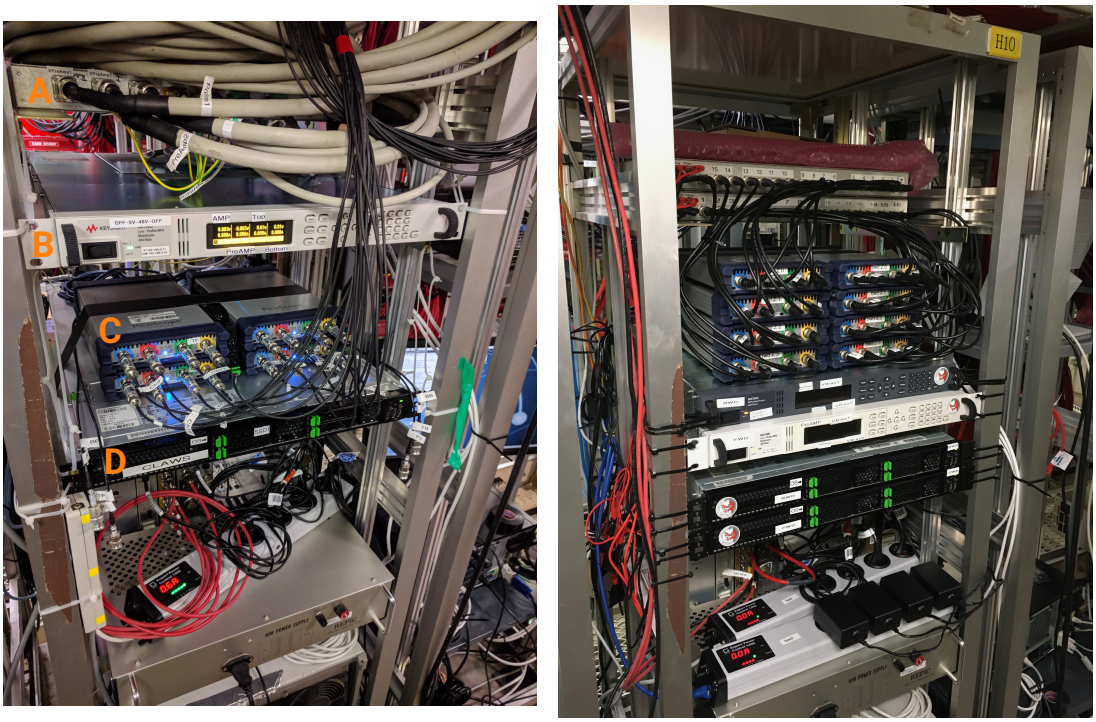

Figure A.1: Phase 2 *(left)* and 3 *(right)* DAQ hardware. The data acquisition system in the electronics hut. Reading the orange numbers on the left: The patch panel *(A)* connects to a *Keysight N6700* power supply *(B)* and the dock box providing three different voltages. Four *PicoScope 6404D* oscilloscopes *(C)* digitize the analog SiPM signals and transmit them to the custom made C++DAQ software on the working machine *(D)*.

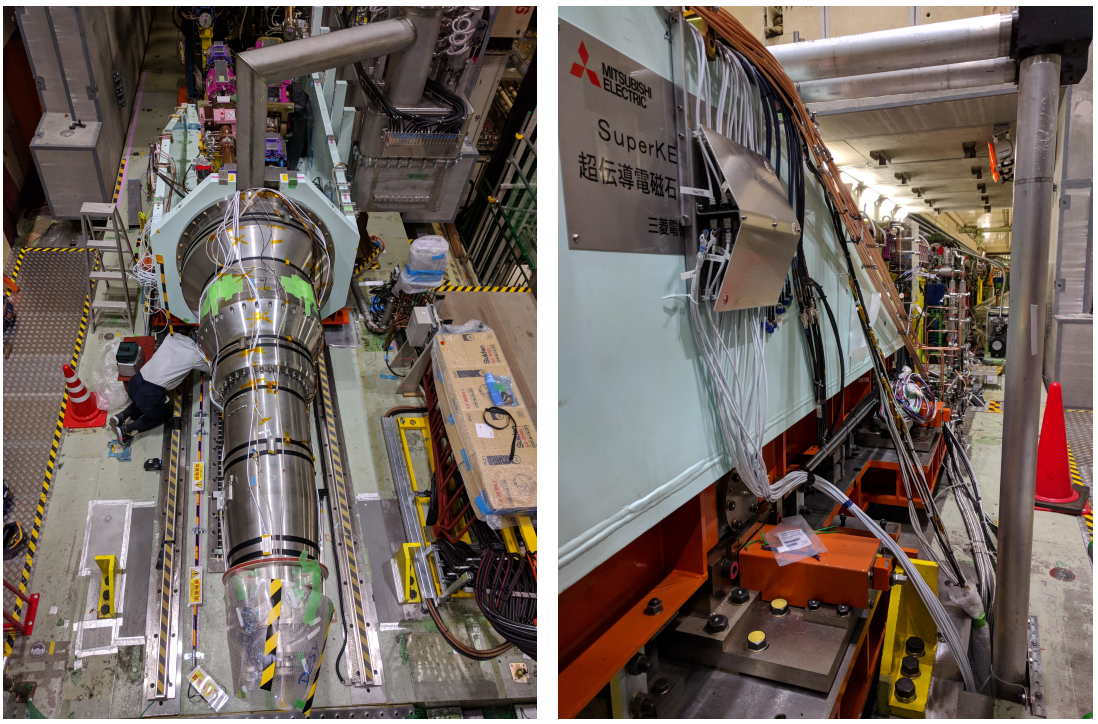

Figure A.2: *(left)* Phase 3 modules mounted on the BWD final focusing magnet. The white Ethernet cables connect to each module. Not all modules are installed. *(right)* The Phase 3 patch panel wall mounted on the final focusing scaffold in FWD direction. The white Ethernet cables are guided down one floor and are routed below the Belle 2 detector to the electronics hut.

	Phase 2	Phase 3
Measures	25.15 × 2.5 cm^2 ladder format	3 × 10.5 cm^2 single channel module
# channels per module	8	1
# of modules installed	2	32
Scintillator material	BC-408	POPOP doped polystyrene
Scintillator measures	20 × 20 × 3 mm^3	30 × 30 × 3 mm^3
Ambient light shielding	/	adhesive black aluminum foil wrapping
Most probable light yield [p.e.]	27.35 ± 0.46 [62]	21.17 ± 0.05
Locations	2nd layer PXD	16 modules per QCS
Positions	at 135° and 225° around the IP	per QCS: 4 z-positions with 4 angles
Dock box design	Active: houses 20 dB amplifiers for each channel and redistributes power and signal lines	Passive: patch panel connecting the short and long Ethernet cables from the modules and electronics hut
Amplification	Onboard: 19 dB (switchable) Dock box: see above	Onboard: 19 dB (switchable) and 12 dB Receiver Board: 12 dB

Table A.1: Comparison of CLAWS hardware components in Phase 2 & 3 of the SuperKEKB commissioning.

B

PHASE 3 CALIBRATION

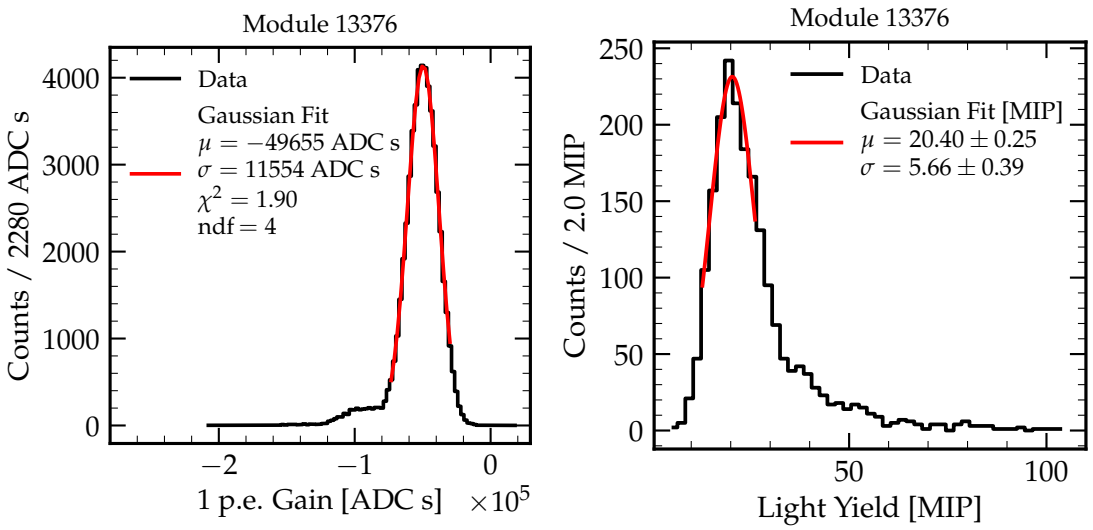

Figure B.1: Phase 3 calibration plots. *(left)* shows an example histogram of 55 000 1 p.e. integrals. The most probable value is used as gain and determined using a maximum likelihood fit. *(right)* shows a histogram of 2022 MIP responses. Each response is integrated over the length of the signal and normalized by the specific SiPM gain. A Gaussian fit around the maximum extracts the most probable light yield. For both fits the Python-SciPy package [87] was used.

Module Number	Serial No.	MP MIP Response	Dark Rate in D	Dark Rate in AL	Side	Z-Pos	Phi [°]
0	13399	28.99 ± 1.17	65	95	fwd	0	0
1	13402	26.19 ± 1.13	60	90	bwd	0	90
2	13403	20.96 ± 1.09	50	100	bwd	1	180
3	13415	19.40 ± 1.08	50	95		spare	
4	13376	20.40 ± 1.25	65	85		spare	
5	13378	21.61 ± 1.96	65	90		spare	
6	13380	20.91 ± 1.37	60	80		spare	
7	13381	22.43 ± 1.18	65	90	bwd	2	90
8	13385	21.83 ± 1.35	55	70	fwd	1	270
9	13388	19.31 ± 1.22	65	85	bwd	1	90
10	13400	20.66 ± 1.42	55	60	bwd	1	0
11	13397	21.67 ± 1.23	75	83	bwd	0	0
12	13416	20.40 ± 1.19	60	100	bwd	1	270
13	13395	21.06 ± 1.34	70	105	fwd	0	180
14	13396	20.55 ± 1.21	55	70	bwd	0	270
15	13377	18.68 ± 1.21	45	80	fwd	1	0
16	13419	22.21 ± 1.43	55	75	bwd	0	180
17	13429	24.12 ± 1.30	45	65	fwd	1	180
18	13389	19.94 ± 1.39	55	100	fwd	1	90
19	13390	20.84 ± 1.29	60	65	fwd	0	270
20	13387	17.94 ± 1.33	50	100	fwd	2	270
21	13441	21.68 ± 1.40	65	90	fwd	2	90
22	13421	16.43 ± 1.31	70	90	bwd	2	180
23	13422	21.34 ± 1.25	55	75	bwd	3	270
24	13405	20.96 ± 1.93	65	90	bwd	2	270
25	13417	21.93 ± 1.21	45	100	fwd	2	180
26	13375	21.40 ± 1.21	45	80	fwd	3	90
27	13414	18.08 ± 1.31	55	70	fwd	2	0
28	13424	20.97 ± 1.32	55	70	bwd	3	0
29	13418	21.21 ± 1.27	55	75	bwd	3	90
30	13379	20.25 ± 1.39	65	100	bwd	2	0
31	13392	21.80 ± 1.23	70	90	fwd	3	180
32	13442	21.81 ± 1.60	50	90	bwd	3	180
33	13420	19.86 ± 1.28	45	60	fwd	3	270
34	13394	21.06 ± 1.83	55	55	fwd	3	0
35	13404	20.92 ± 1.66	60	80		spare	

Table B.1: Phase 3 Module Characterization Summary. In columns of the dark rate, *in D* means "in darkness without shielding" and *in AL* means "in ambient light with shielding".

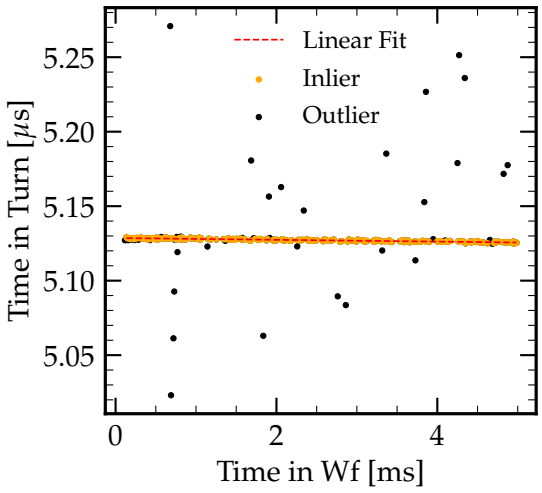

Figure C.1: Time drift correction plot. The data shows channel Top Forward A of run 516368-0143. The plot shows a scatter plot of the data after the selection process of $5.00\,\mu s \leq t_{turn} \leq 5.275\,\mu s$ and a minimum signal amplitude of 20 MIP together with a linear fit. The fit result is $m = (-0.605 \pm 0.019)\,ns/ms$ and $b = (5.129 \pm 0.000)\,\mu s$.

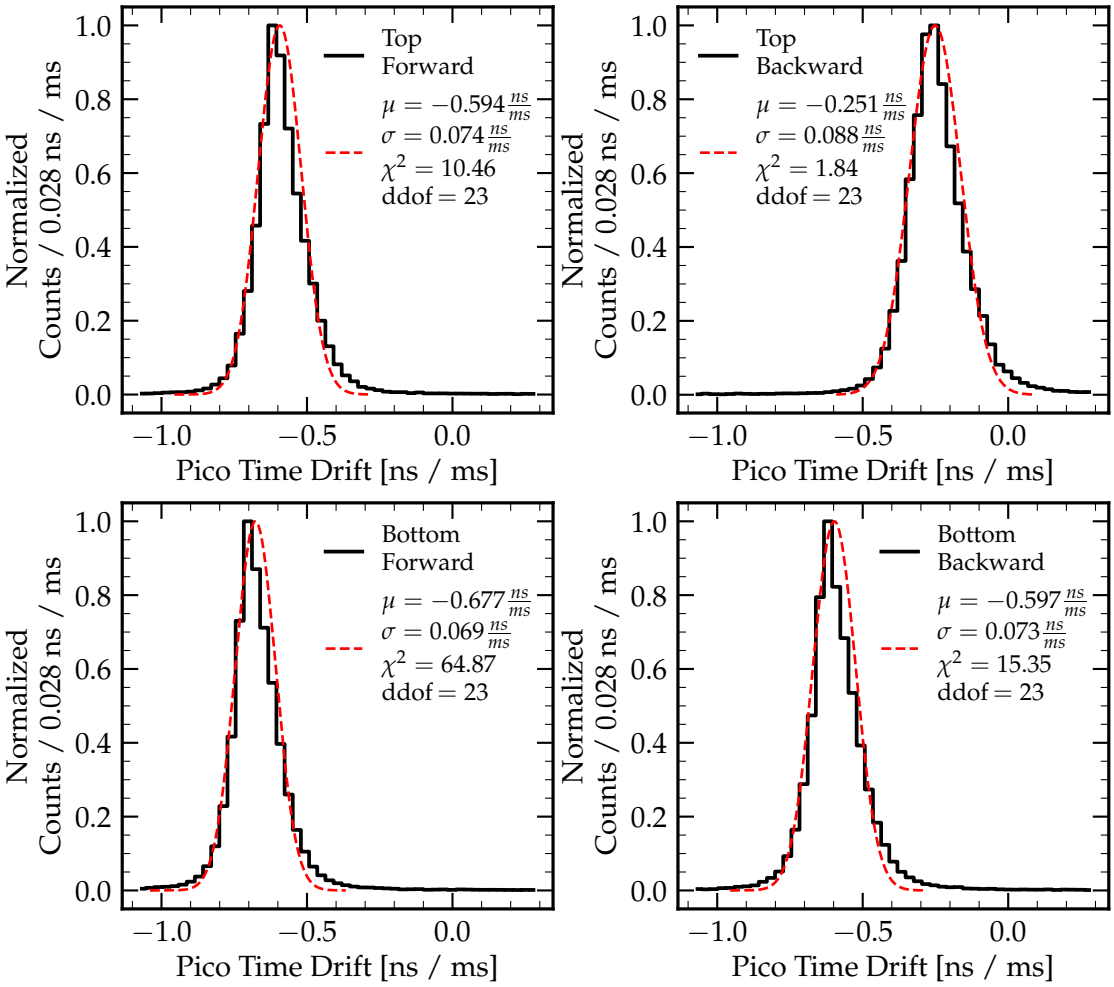

Figure C.2: Time drift correction histogram per oscilloscope. The Gaussian log-likehood fits are implemented with the Python-SciPy package [87].

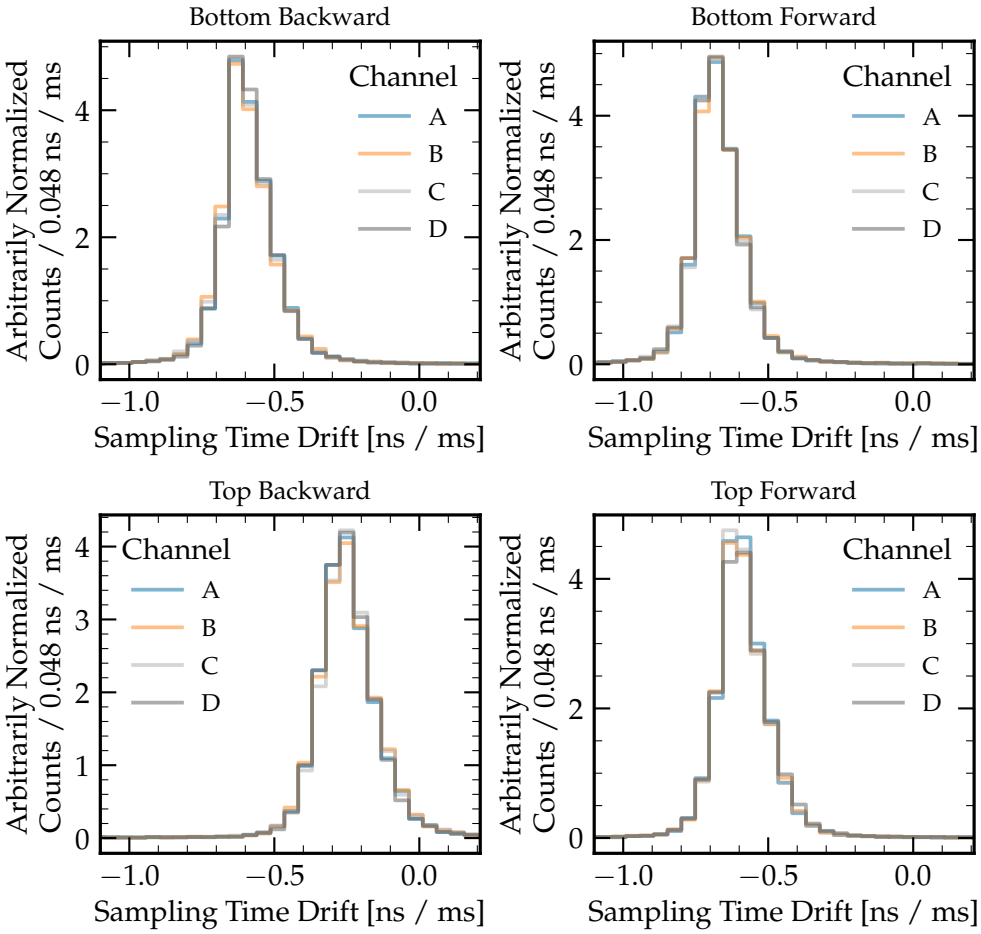

Figure C.3: Sampling time drift correction histograms per oscilloscope & channel.

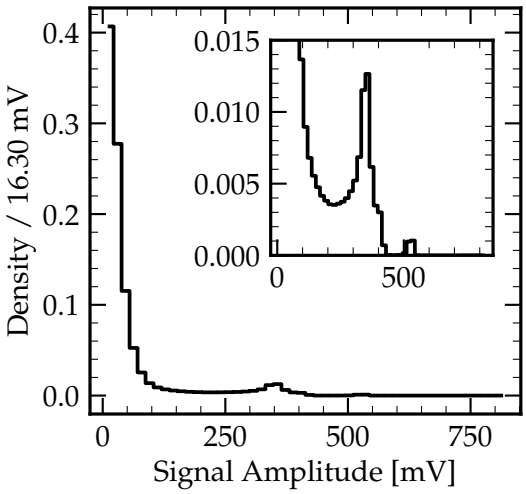

Figure C.4: Histogram of the signal amplitudes. The inset illustrates a zoom on the y axis. The axes labels of the inset are the same as of the outer plot. The excess around 350 mV origins from the saturation of the CLAWS system.

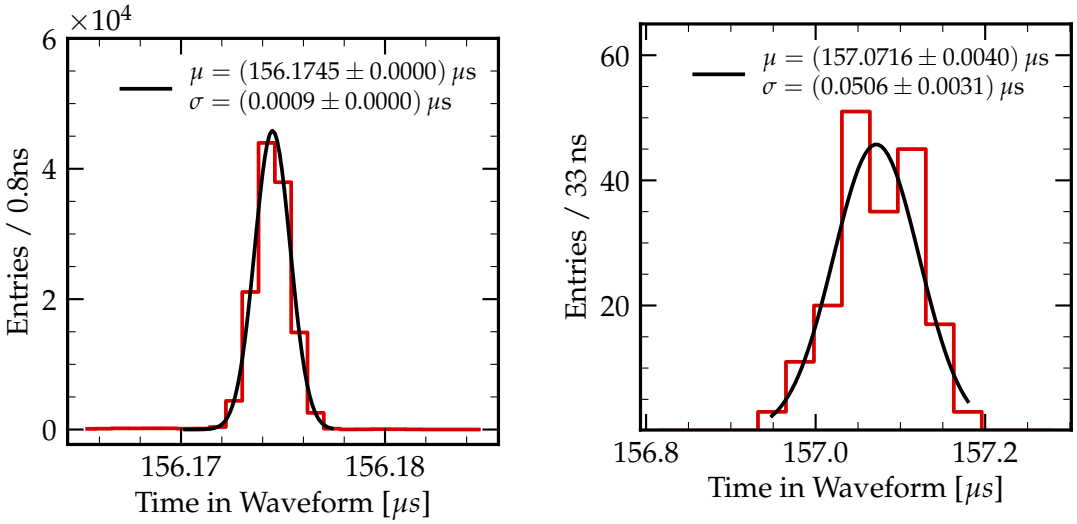

Figure C.5: Gaussian fits of the high energetic excess in the LER hit spectrum at around $t_{\text{turn}} = 6\,\mu\text{s}$. *(Left)* illustrates a Gaussian fit of the last injection bunch pass-by of previous to the excess. *(right)* Gaussian fit around the high energetic excess.

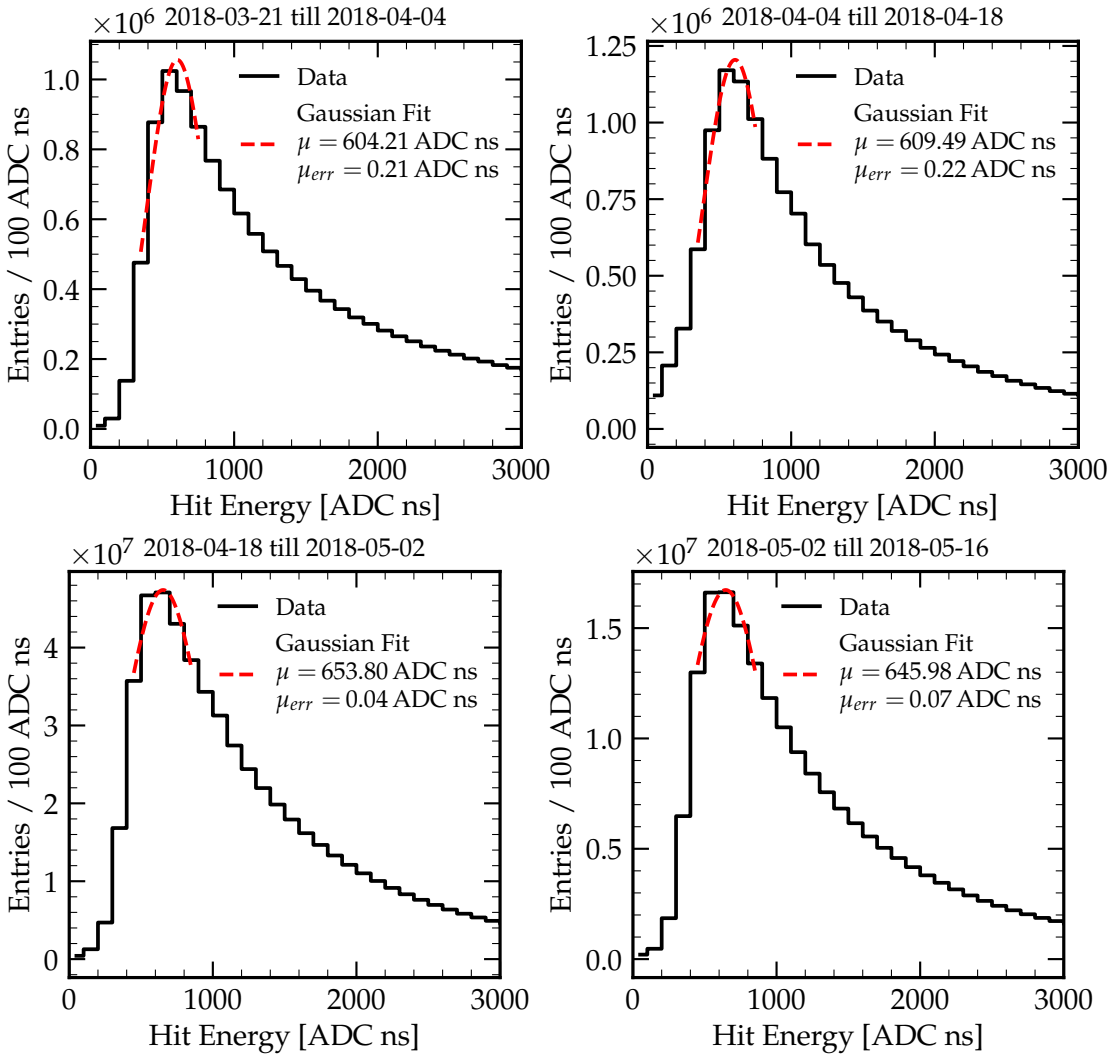

Figure C.6: Fits of the most probable detector response stability plot of the first half of Phase 2. The fit uses a Gaussian distribution and has been applied ±2 bins around the maximum using SciPy's *curve_fit* method [87].

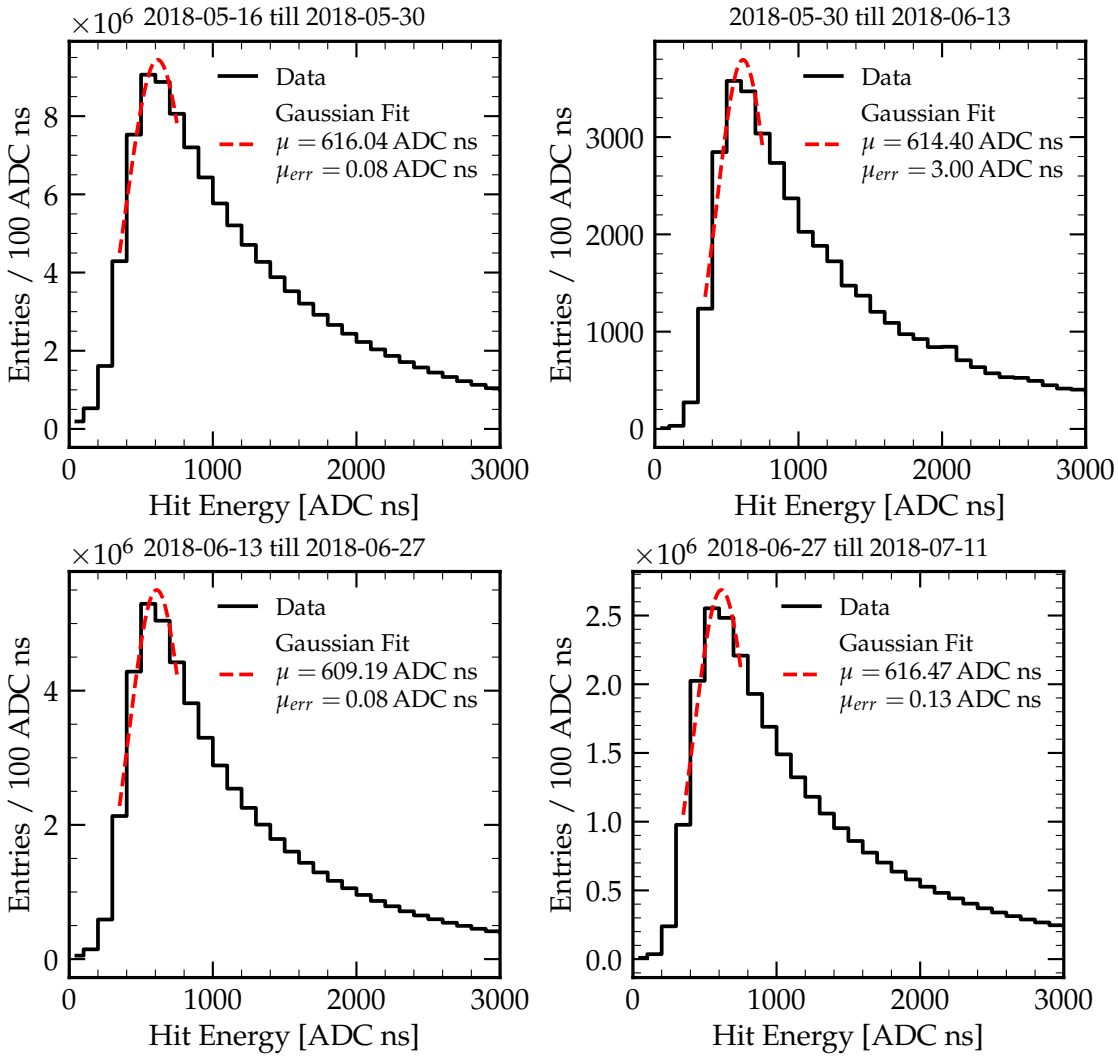

Figure C.7: Fits for the most probable detector response stability of the second half of Phase 2. The fit uses a Gaussian distribution and has been applied ±2 bins around the maximum using SciPy's *curve_fit* method [87].

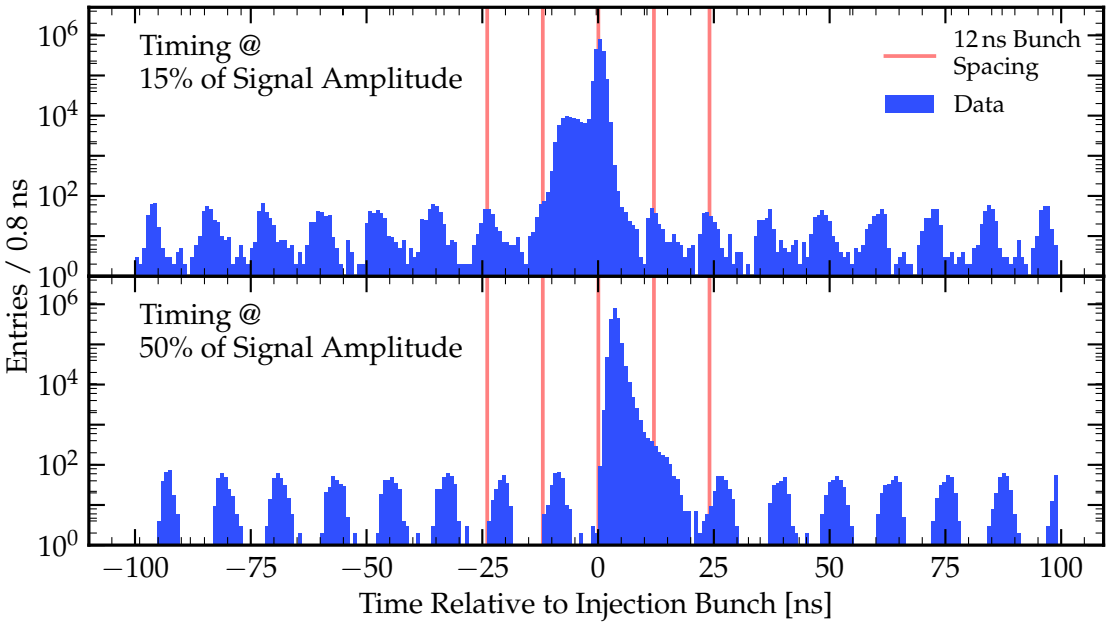

Figure C.8: Bunch structure around the injection bunch. The vertical red lines emphasize the bunch spacing of 12 ns around the injection bunch. The top plot shows the signal timing at 15 % and the bottom plot at 50 %.

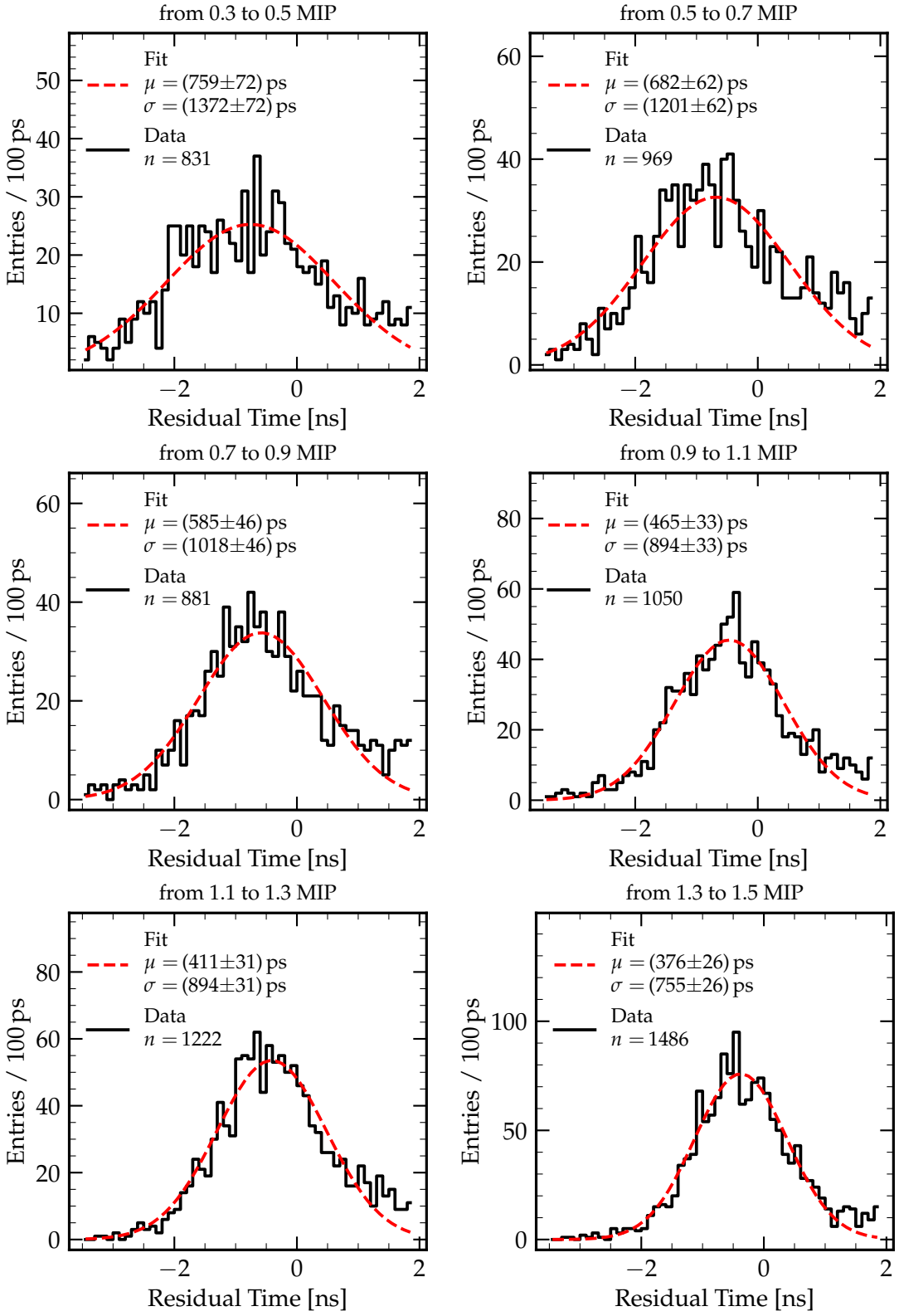

Figure C.9: Energy dependent time resolution of the Phase 2 detector. The data includes all 16 channels of the Phase 2 detector. Each fit uses a Gaussian distribution using SciPy's *curve_fit* method [87].

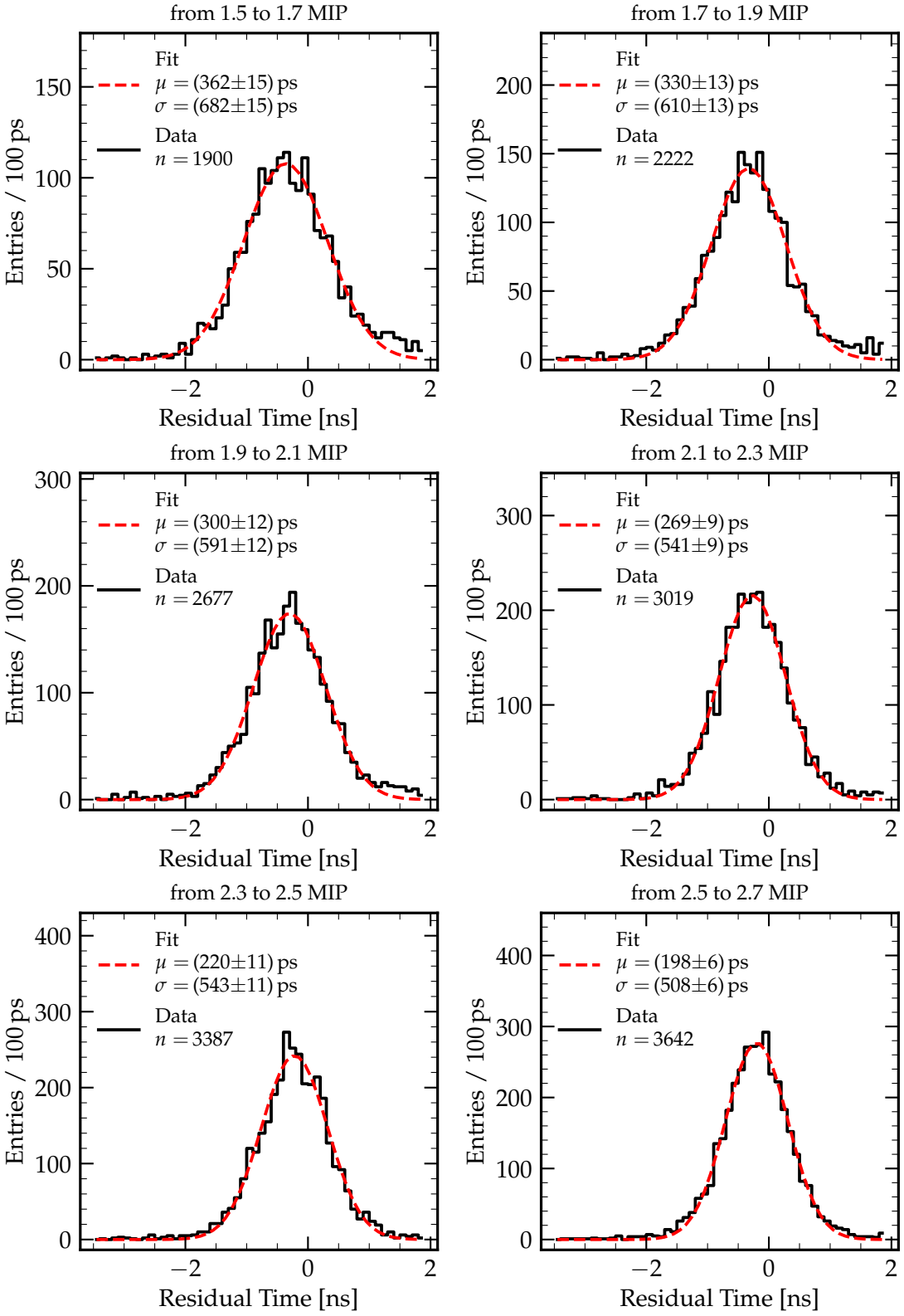

Figure C.10: Energy dependent time resolution of the Phase 2 detector. The data includes all 16 channels of the Phase 2 detector. Each fit uses a Gaussian distribution using SciPy's *curve_fit* method [87].

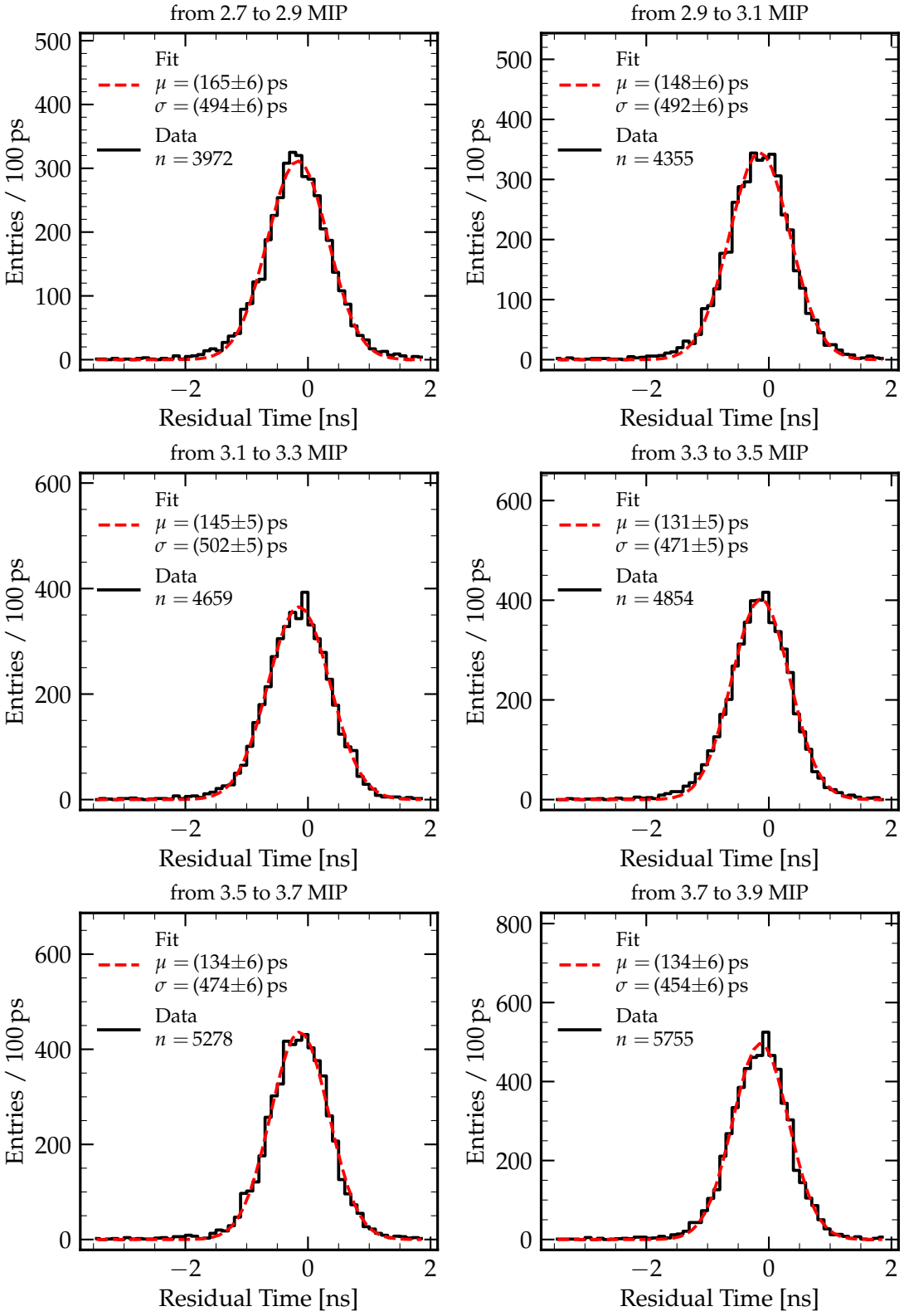

Figure C.11: Energy dependent time resolution of the Phase 2 detector. The data includes all 16 channels of the Phase 2 detector. Each fit uses a Gaussian distribution using SciPy's *curve_fit* method [87].

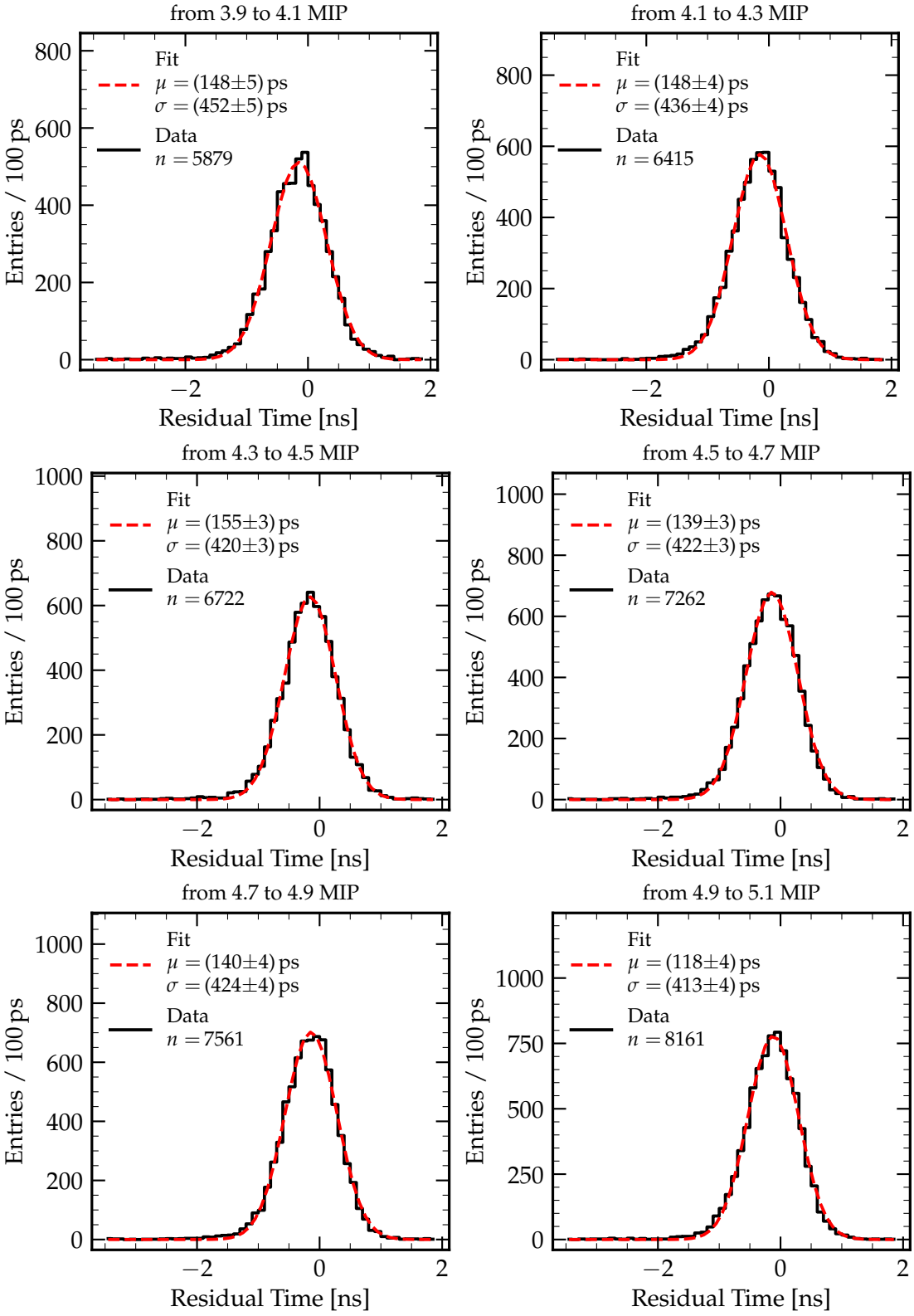

Figure C.12: Energy dependent time resolution of the Phase 2 detector. The data includes all 16 channels of the Phase 2 detector. Each fit uses a Gaussian distribution using SciPy's *curve_fit* method [87].

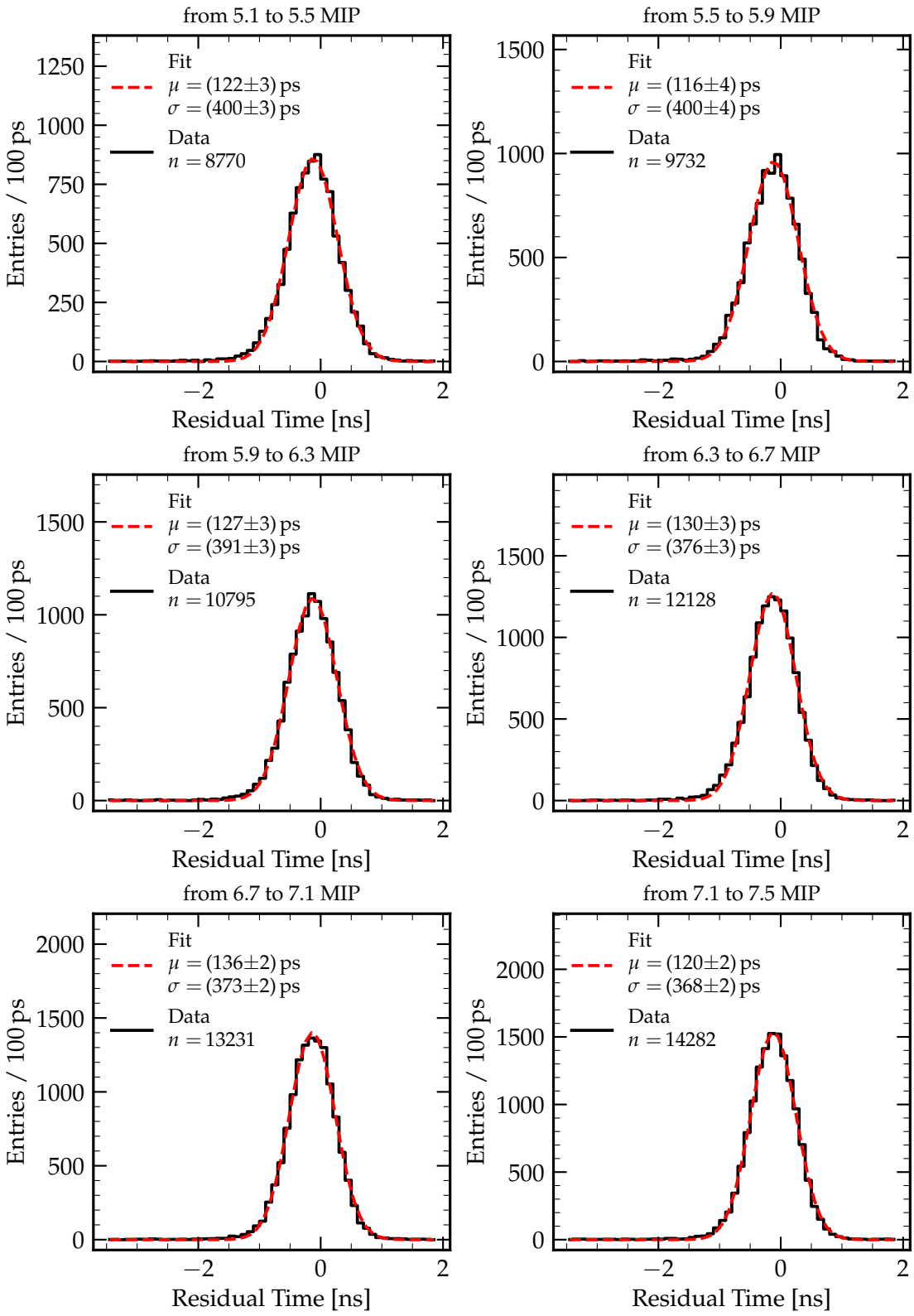

Figure C.13: Energy dependent time resolution of the Phase 2 detector. The data includes all 16 channels of the Phase 2 detector. Each fit uses a Gaussian distribution using SciPy's *curve_fit* method [87].

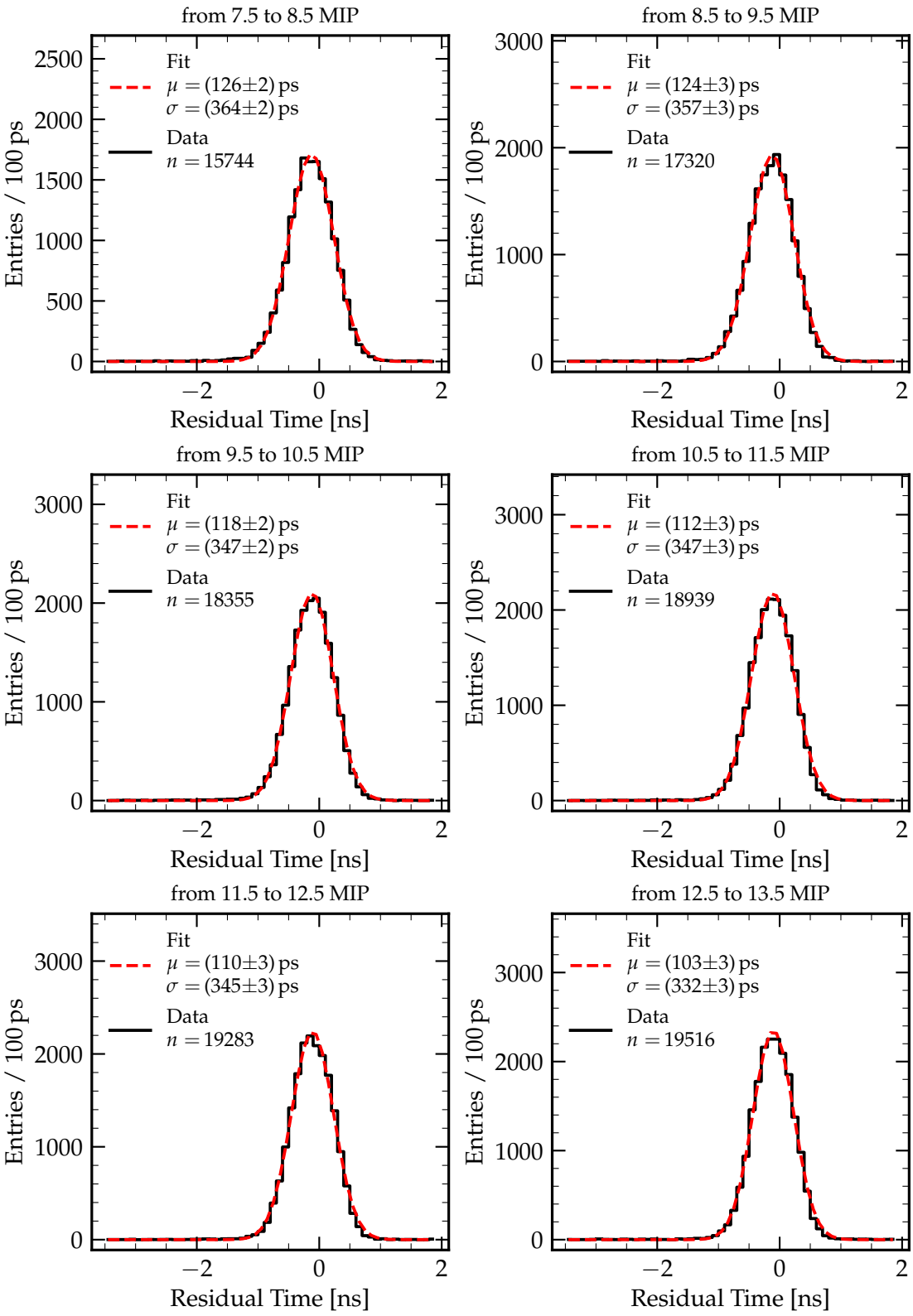

Figure C.14: Energy dependent time resolution of the Phase 2 detector. The data includes all 16 channels of the Phase 2 detector. Each fit uses a Gaussian distribution using SciPy's *curve_fit* method [87].

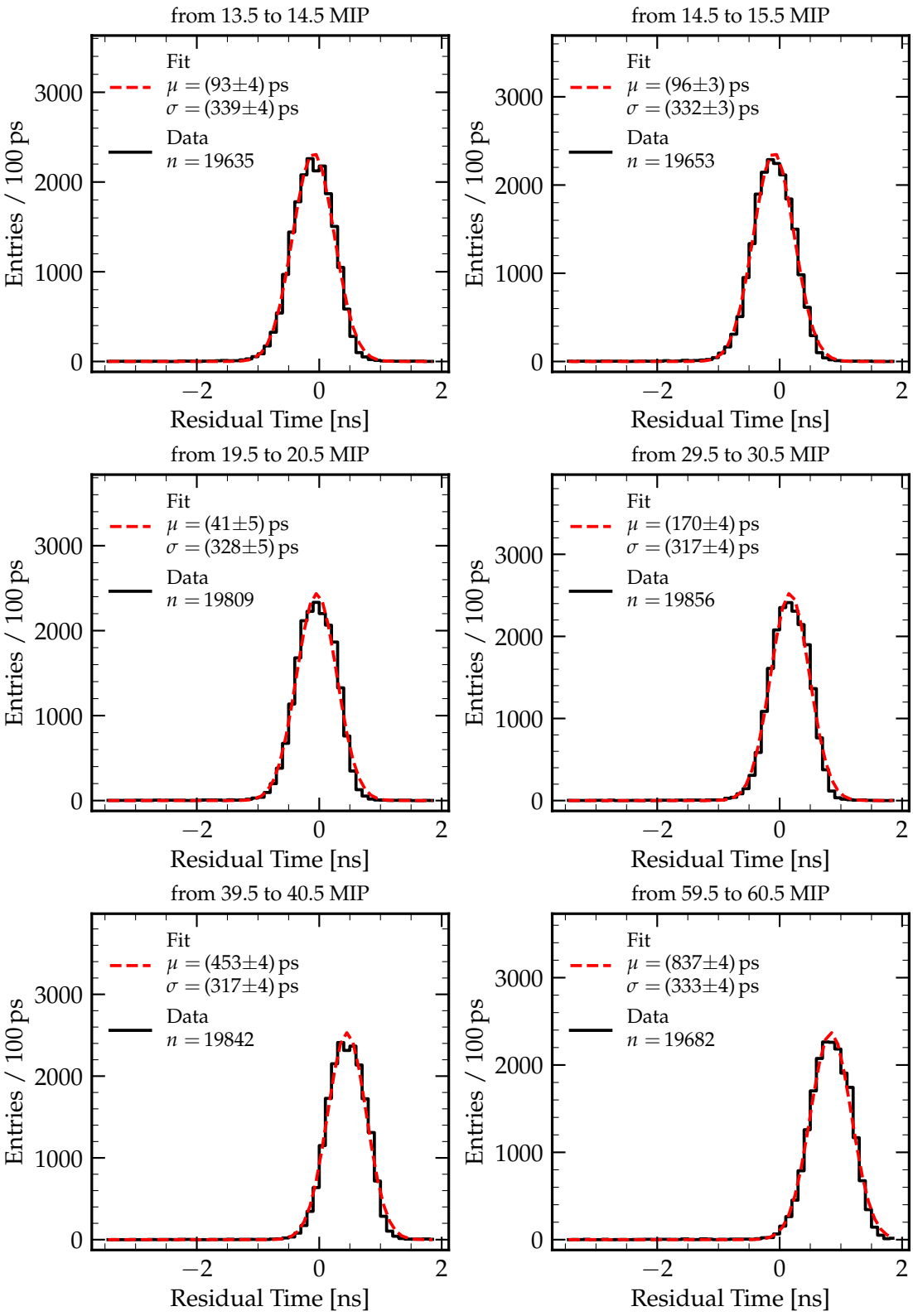

Figure C.15: Energy dependent time resolution of the Phase 2 detector. The data includes all 16 channels of the Phase 2 detector. Each fit uses a Gaussian distribution using SciPy's *curve_fit* method [87].

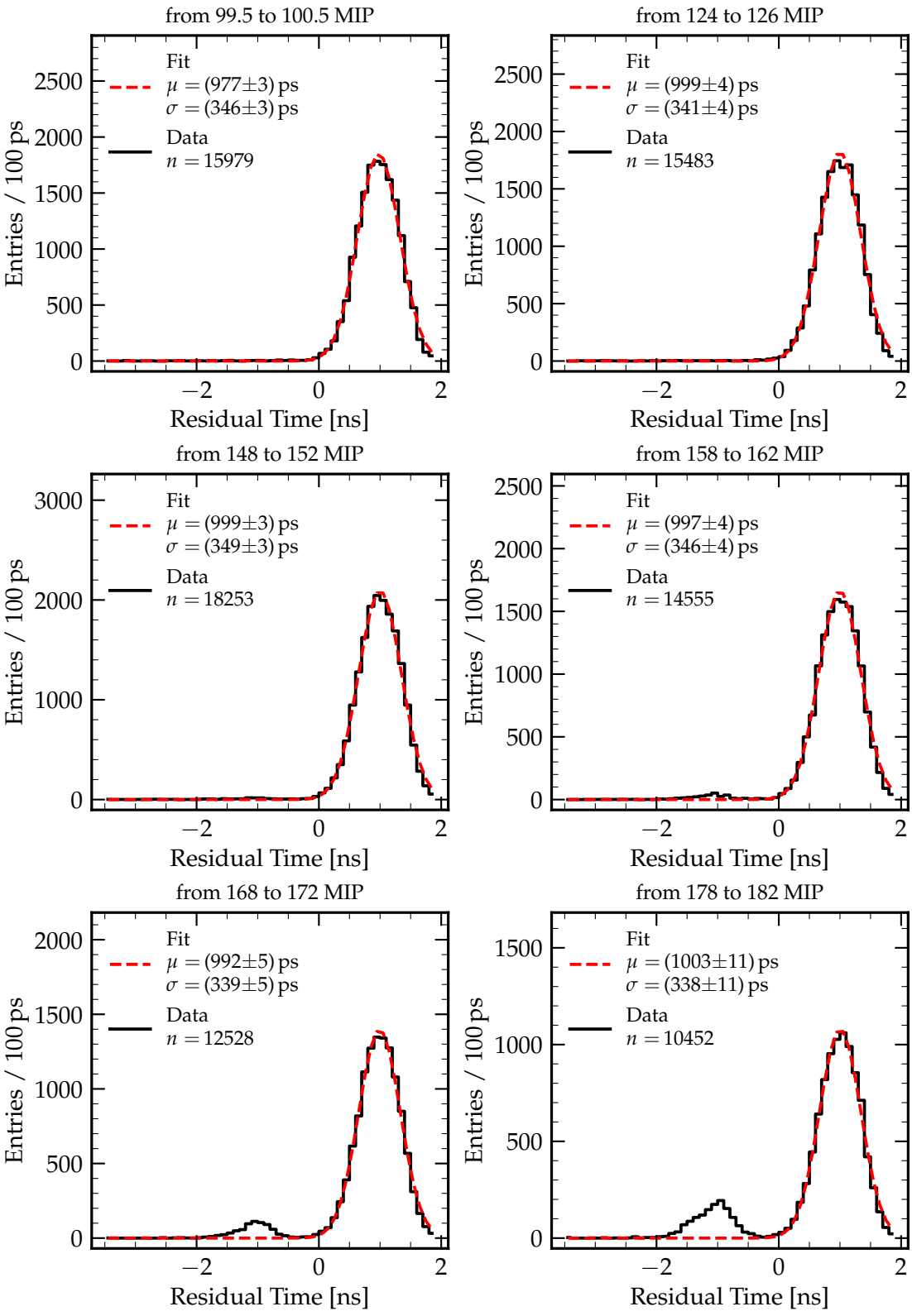

Figure C.16: Energy dependent time resolution of the Phase 2 detector. The data includes all 16 channels of the Phase 2 detector. Each fit uses a Gaussian distribution using SciPy's *curve_fit* method [87].

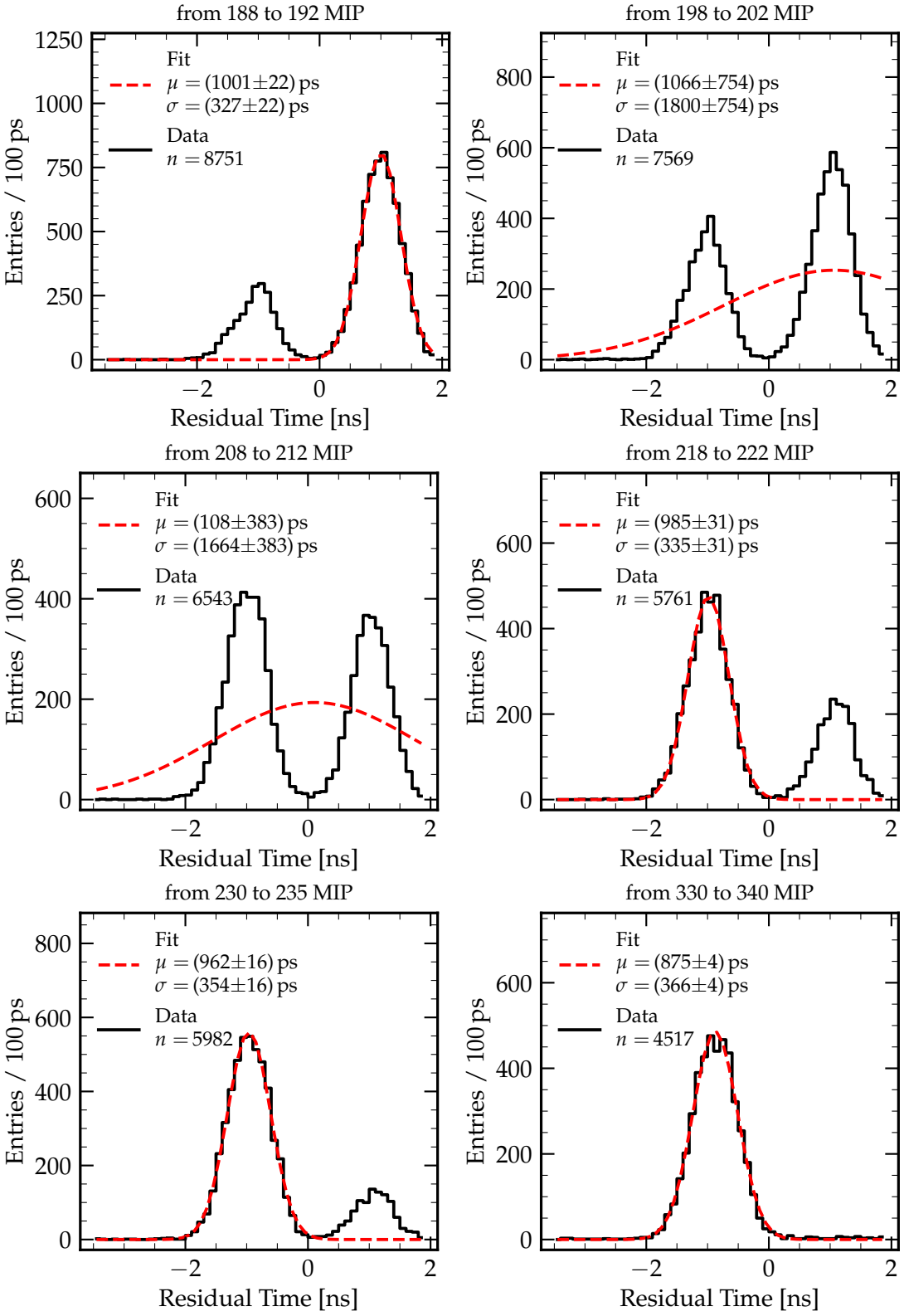

Figure C.17: Energy dependent time resolution of the Phase 2 detector. The data includes all 16 channels of the Phase 2 detector. Each fit uses a Gaussian distribution using SciPy's *curve_fit* method [87].

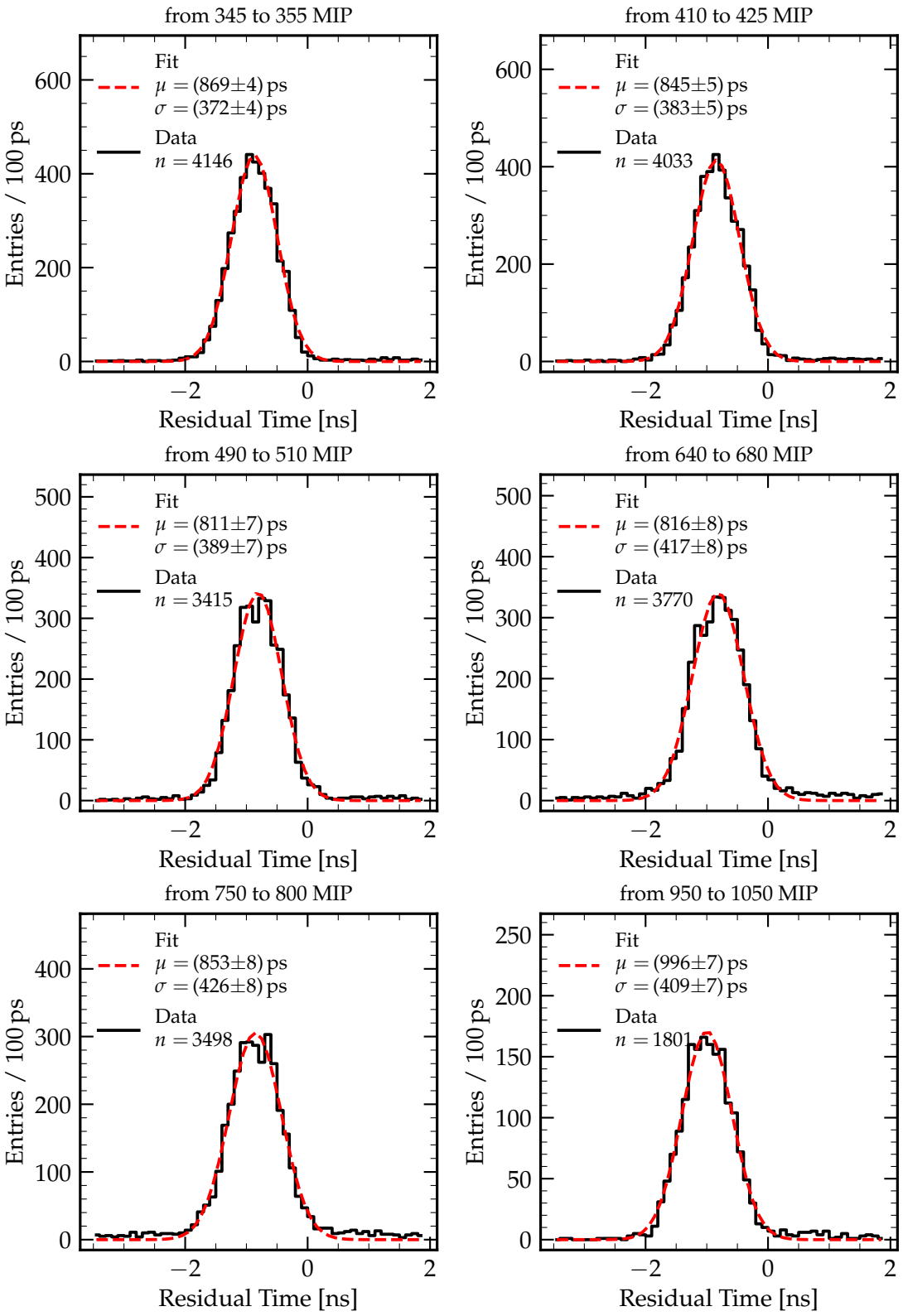

Figure C.18: Energy dependent time resolution of the Phase 2 detector. The data includes all 16 channels of the Phase 2 detector. Each fit uses a Gaussian distribution using SciPy's *curve_fit* method [87].

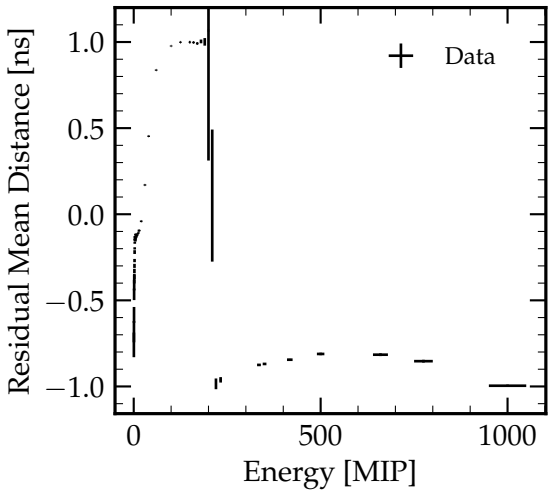

Figure C.19: Residual mean of energy dependent time resolution fits. The step around 200 MIP is the result from the switch of the mean from the positive to the negative as featured in Fig. C.17.

D

COOLING TIME ANALYSIS

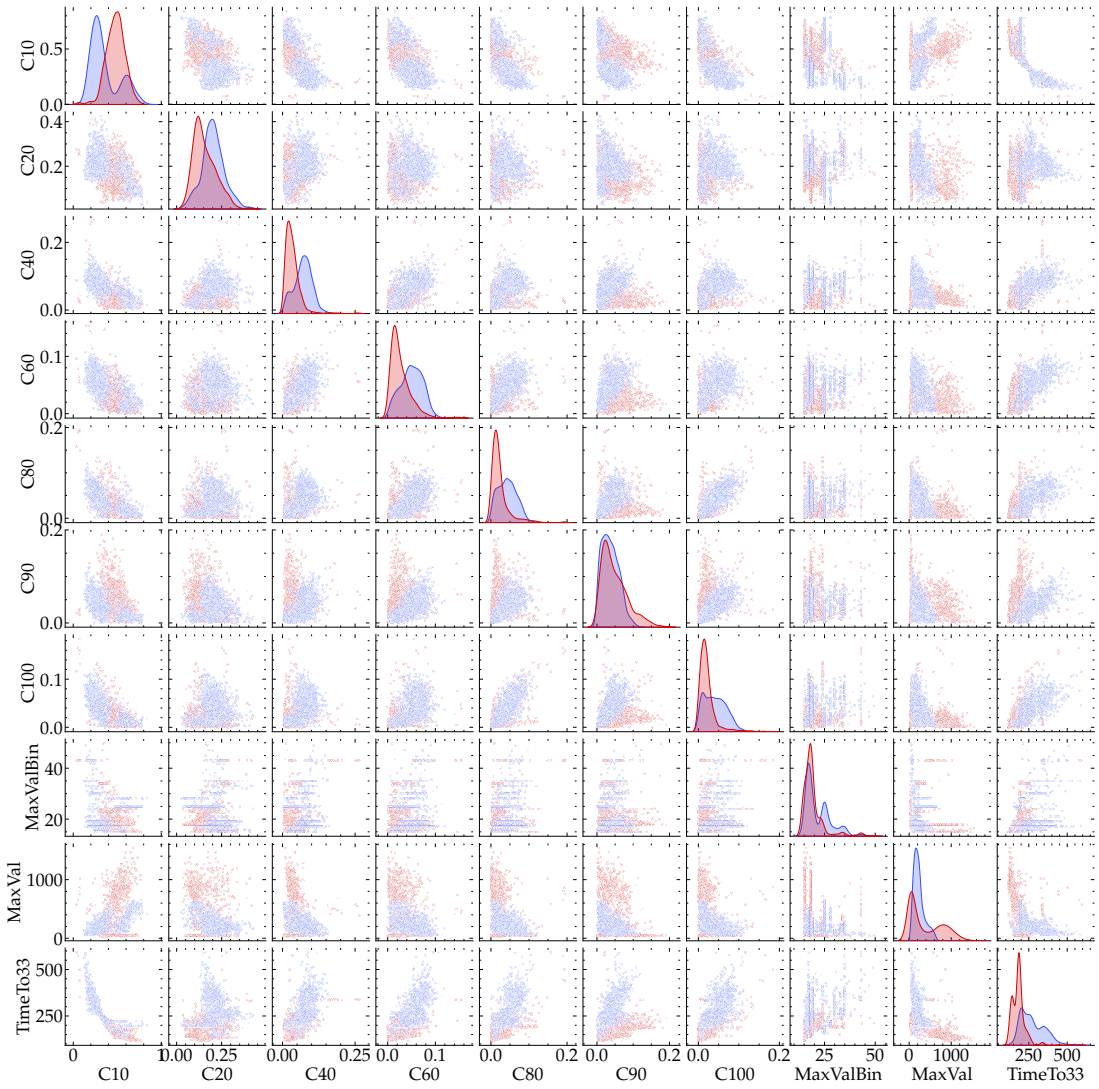

Figure D.1: Pairplot of the decision tree features for LER-HER classification. Data in red represents the LER and blue the HER. This plot uses a data sub-sample of 1000 data points.

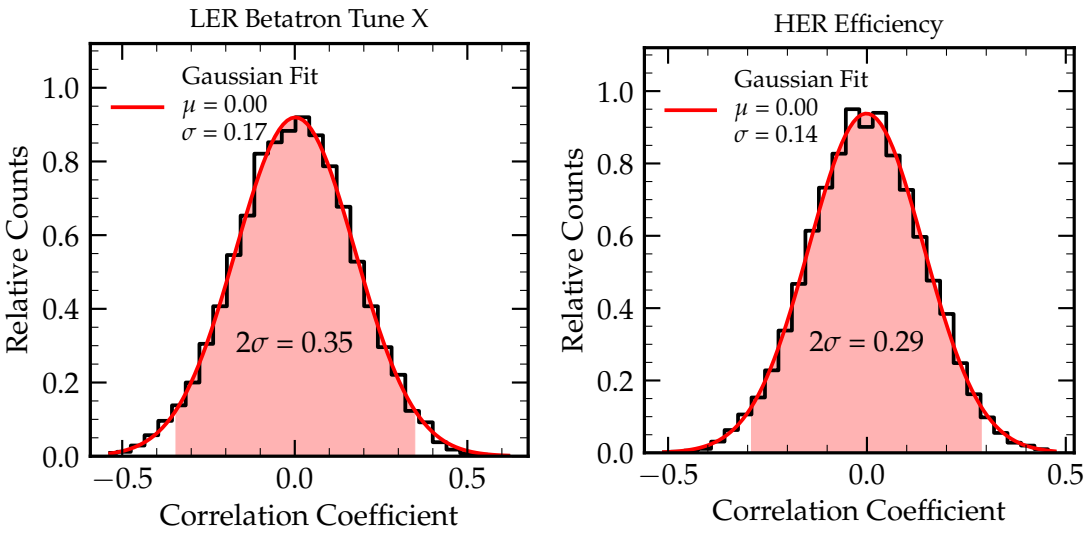

Figure D.2: Significance determination of Spearman correlation coefficients. Each data set has a size of 1000 and is simulated using the bootstrap method. The LER betatron tune x parameter is representative for all other betatron tune parameters. The HER efficiency has a similar data set size as all other parameters and is therefore representative. The fits are done using Scipy's *curve_fit* method [87].

BIBLIOGRAPHY

[1] J. H. Christenson, J. W. Cronin, V. L. Fitch, and R. Turlay. "Evidence for the 2π Decay of the K_2^0 Meson." In: *Phys. Rev. Lett.* 13 (1964), pp. 138–140. DOI: 10.1103/PhysRevLett.13.138.

[2] Nicola Cabibbo. "Unitary Symmetry and Leptonic Decays." In: *Phys. Rev. Lett.* 10 (1963), pp. 531–533. DOI: 10.1103/PhysRevLett.10.531.

[3] Makoto Kobayashi and Toshihide Maskawa. "CP Violation in the Renormalizable Theory of Weak Interaction." In: *Prog. Theor. Phys.* 49 (1973), pp. 652–657. DOI: 10.1143/PTP.49.652.

[4] Augustin, J. -E. and Boyarski, A. M. "Discovery of a Narrow Resonance in e^+e^- Annihilation." In: *Phys. Rev. Lett.* 33 (23 1974), pp. 1406–1408. DOI: 10.1103/PhysRevLett.33.1406. URL: https://link.aps.org/doi/10.1103/PhysRevLett.33.1406.

[5] J. J. Aubert and U. Becker. "Experimental Observation of a Heavy Particle J." In: *Phys. Rev. Lett.* 33 (23 1974), pp. 1404–1406. DOI: 10.1103/PhysRevLett.33.1404. URL: https://link.aps.org/doi/10.1103/PhysRevLett.33.1404.

[6] F. Englert and R. Brout. "Broken Symmetry and the Mass of Gauge Vector Mesons." In: *Phys. Rev. Lett.* 13 (1964). Ed. by J. C. Taylor, pp. 321–323. DOI: 10.1103/PhysRevLett.13.321.

[7] Peter W. Higgs. "Broken Symmetries and the Masses of Gauge Bosons." In: *Phys. Rev. Lett.* 13 (1964). Ed. by J. C. Taylor, pp. 508–509. DOI: 10.1103/PhysRevLett.13.508.

[8] G. S. Guralnik, C. R. Hagen, and T. W. B. Kibble. "Global Conservation Laws and Massless Particles." In: *Phys. Rev. Lett.* 13 (1964). Ed. by J. C. Taylor, pp. 585–587. DOI: 10.1103/PhysRevLett.13.585.

[9] Collaboration ATLAS. "Observation of a new particle in the search for the Standard Model Higgs boson with the ATLAS detector at the LHC." In: *Physics Letters B* 716.1 (2012), pp. 1–29. ISSN: 0370-2693. DOI: https://doi.org/10.1016/j.physletb.2012.08.020. URL: https://www.sciencedirect.com/science/article/pii/S037026931200857X.

[10] Serguei Chatrchyan et al. "Observation of a New Boson at a Mass of 125 GeV with the CMS Experiment at the LHC." In: *Phys. Lett. B* 716 (2012), pp. 30–61. DOI: 10.1016/j.physletb.2012.08.021. arXiv: 1207.7235 [hep-ex].

[11] *Standard Model Summary Plots March 2021*. Tech. rep. Geneva: CERN, 2021. URL: https://cds.cern.ch/record/2758261.

[12] G. Angloher et al. "The COSINUS project: perspectives of a NaI scintillating calorimeter for dark matter search." In: *The European Physical Journal C* 76.8 (2016). ISSN: 1434-6052. DOI: 10.1140/epjc/s10052-016-4278-3. URL: http://dx.doi.org/10.1140/epjc/s10052-016-4278-3.

[13] J. Grange et al. *Muon (g-2) Technical Design Report*. 2018. arXiv: 1501.06858 [physics.ins-det].

[14] B. Abi et al. "Measurement of the Positive Muon Anomalous Magnetic Moment to 0.46 ppm." In: *Phys. Rev. Lett.* 126 (14 2021), p. 141801. DOI: 10.1103/PhysRevLett.126.141801. URL: https://link.aps.org/doi/10.1103/PhysRevLett.126.141801.

[15] F. Lehner and S. Faverot-Spengler, eds. *ARGUS Fest, 20 years of B meson mixing 1987-2007. Proceedings, ARGUS-symposium, DESY, Hamburg, Germany, November 9, 2007*. Sept. 2007.

[16] T. Abe et al. "Belle II Technical Design Report." In: (2010). arXiv: 1011.0352.

[17] Yukiyoshi Ohnishi. "Highlights from SuperKEKB Commissioning for early stage of Nano-Beam Scheme and Crab Waist Scheme." In: *PoS* ICHEP2020 (2021), p. 695. DOI: 10.22323/1.390.0695.

[18] Marko Bracko and the SuperBelle Collaboration. "Status of the super KEK B factory." In: *Journal of Physics: Conference Series* 171.1 (2009).

[19] Tetsuo Abe et al. "Commissioning of KEKB." In: *Progress of Theoretical and Experimental Physics* 2013.3 (2013). DOI: 10.1093/ptep/pts101. URL: http://ptep.oxfordjournals.org/content/2013/3/03A010.full.pdf+html.

[20] Carsten Niebuhr. *Highlights from the Belle II Experiment and Flavour Physics in e^+e^-*. EPS-HEP Conference 2021. 2021. URL: https://indico.desy.de/event/28202/contributions/102726/attachments/67952/85073/EPS-HEP%20Plenary%20Belle%20II%20Flavor.pdf.

[21] Felix Müller. "Characterization and Optimization of the PrototypeDEPFET Modules for the Belle II Pixel Vertex Detector." PhD thesis. Föhringer Ring 6, 80805 München: Max-Planck-Institut für Physik & Ludwig-Maximilians-Universität München, 2017.

[22] Helmut Wiedemann. *Particle Accelerator Physics I - Basic Principles and Linear Beam Dynamics*. Berlin: Springer, 1999. DOI: 3-540-64671-x2nd{E}dition.

[23] M. Tanabashi et al. "Review of Particle Physics." In: *Phys. Rev.* D98.3 (2018), p. 030001. DOI: 10.1103/PhysRevD.98.030001.

[24] S. Myers and H. Schopper, eds. *Elementary Particles - Accelerators and Colliders*. Vol. 21C. Landolt-Boernstein - Group I Elementary Particles, Nuclei and Atoms. Springer, 2013. ISBN: 9783642230523, 9783642230530. DOI: 10.1007/978-3-642-23053-0.

[25] D.A. Edwards and M.J. Syphers. *An Itroduction to the Physics of High Energy Accelerators*. New York: John Wiley & Sons, Inc., 1993.

[26] Andrew M. Sessler. "Liouville's Theorem and Phase-Space Cooling." In: CERN, 1994. URL: http://cds.cern.ch/record/398448.

[27] M. Tanabashi et al. "Review of Particle Physics." In: *Phys. Rev.* D98.3 (2018), p. 030001. DOI: 10.1103/PhysRevD.98.030001.

[28] P. Raimondi. *Status on SuperB effort*. Talk given at the 2nd SuperB workshop, Frascati. 2006. URL: http://www.lnf.infn.it/conference/superb06/talks/raimondi1.ppt.

[29] Tetsuo Abe et al. "Achievements of KEKB." In: *Progress of Theoretical and Experimental Physics* 2013.3 (Mar. 2013). 03A001. ISSN: 2050-3911. DOI: 10.1093/ptep/pts102. eprint: https://academic.oup.com/ptep/article-pdf/2013/3/03A001/4440618/pts102.pdf. URL: https://doi.org/10.1093/ptep/pts102.

[30] Nils Braun, Alexander Glazov, Felix Metzer, and Eugenio Paoloni. "Study of the collision point properties." In: (2018). Internal note describing selection is BELLE2-NOTE-PH-2018-006.

[31] M. Satoh et al. "Commissioning Status of SuperKEKB Injector Linac." In: *Proc. of International Particle Accelerator Conference (IPAC'16), Busan, Korea, May 8-13, 2016*. International Particle Accelerator Conference 7. JACoW, 2016, p. 4152. ISBN: 9783954501472. DOI: 10.18429/JACoW-IPAC2016-THPOY027.

[32] X. Zhou, T. Natsui, Y. Ogawa, and M. Yoshida. "Ytterbium Fiber and Disk Laser of RF Gun for SuperKEKB." In: *IPAC2014: Proceedings of the 5th International Particle Accelerator Conference, Dresden, Germany, June 15-20, 2014*. International Particle Accelerator Conference. JACoW, 2014, p. 2415. ISBN: 9783954501328.

[33] Masanori Satoh. *B2GM Injector Linac Status 2020*. 2020. URL: https://indico.belle2.org/event/2419/contributions/11670/attachments/5995/9312/MSatoh_B2GM_Injector_Linac_Status_20200622.pdf.

[34] T. Mori et al. Proceedings of IPAC2012, New Orleans, Louisiana, USA. 2012. URL: https://accelconf.web.cern.ch/IPAC2012/papers/tuppr089.pdf.

[35] Hiro Nakayama. *39th B2GM - Summary of MDI Session*. Belle 2 Collaboration, 2021.

[36] P. Fischer et al. "Progress towards a large area, thin DEPFET detector module." In: *Nuclear Instruments and Methods in Physics Research Section A: Accelerators, Spectrometers, Detectors and Associated Equipment* 582.3 (2007). VERTEX 2006, pp. 843–848. ISSN: 0168-9002. DOI: https://doi.org/10.1016/j.nima.2007.07.108. URL: https://www.sciencedirect.com/science/article/pii/S0168900207015859.

[37] M. Friedl et al. "The Belle II Silicon Vertex Detector." In: *Nuclear Instruments and Methods in Physics Research Section A: Accelerators, Spectrometers, Detectors and Associated Equipment* 732 (2013). Vienna Conference on Instrumentation 2013, pp. 83–86. ISSN: 0168-9002. DOI: https://doi.org/10.1016/j.nima.2013.05.171. URL: https://www.sciencedirect.com/science/article/pii/S0168900213007936.

[38] N. Taniguchi. "Central Drift Chamber for Belle-II." In: *Journal of Instrumentation* 12.06 (2017), pp. C06014–C06014. DOI: 10.1088/1748-0221/12/06/c06014. URL: https://doi.org/10.1088/1748-0221/12/06/c06014.

[39] M. Akatsu et al. "Time-of-propagation Cherenkov counter for particle identification." In: *Nuclear Instruments and Methods in Physics Research Section A: Accelerators, Spectrometers, Detectors and Associated Equipment* 440.1 (2000), pp. 124–135. ISSN: 0168-9002. DOI: https://doi.org/10.1016/S0168-9002(99)00819-0. URL: https://www.sciencedirect.com/science/article/pii/S0168900299008190.

[40] T. Iijima et al. "A novel type of proximity focusing RICH counter with multiple refractive index aerogel radiator." In: *Nuclear Instruments and Methods in Physics Research Section A: Accelerators, Spectrometers, Detectors and Associated Equipment* 548.3 (2005), pp. 383–390. ISSN: 0168-9002. DOI: https://doi.org/10.1016/j.nima.2005.05.030. URL: https://www.sciencedirect.com/science/article/pii/S0168900205010843.

[41] A. Kuzmin. "Electromagnetic calorimeter of Belle II." In: *Nuclear Instruments and Methods in Physics Research Section A: Accelerators, Spectrometers, Detectors and Associated Equipment* 958 (2020). Proceedings of the Vienna Conference on Instrumentation 2019, p. 162235. ISSN: 0168-9002. DOI: https://doi.org/10.1016/j.nima.2019.05.076. URL: https://www.sciencedirect.com/science/article/pii/S0168900219307405.

[42] T. Aushev et al. "A scintillator based endcap KL and muon detector for the Belle II experiment." In: *Nuclear Instruments and Methods in Physics Research Section A: Accelerators, Spectrometers, Detectors and Associated Equipment* 789 (2015), pp. 134–142. ISSN: 0168-9002. DOI: https://doi.org/10.1016/j.nima.2015.03.060. URL: https://www.sciencedirect.com/science/article/pii/S016890021500385X.

[43] A. Abashian et al. "The KL/μ detector subsystem for the BELLE experiment at the KEK B-factory." In: *Nuclear Instruments and Methods in Physics Research Section A: Accelerators, Spectrometers, Detectors and Associated Equipment* 449.1 (2000), pp. 112–124. ISSN: 0168-9002. DOI: https://doi.org/10.1016/S0168-9002(99)01383-2. URL: https://www.sciencedirect.com/science/article/pii/S0168900299013832.

[44] Emi Kou, Phillip Urquijo, B2TiP Theory community, and Belle II Collaboration. "The Belle II Physics Book." In: (2018).

[45] Björn Spruck. PXD Run Coordinator; Johannes Gutenberg-Universität Mainz; Personal Conversation.

[46] Kodai Matsuoka. Run Coordinator; KEK Staff; Personal Conversation.

[47] *First turns and successful storage of beams in the SuperKEKB electron and positron rings*. 2016. URL: https://www.kek.jp/en/newsroom/release/20160302163000/.

[48] P. M. Lewis et al. "First Measurements of Beam Backgrounds at SuperKEKB." In: *Nucl. Instrum. Meth. A* 914 (2019), pp. 69–144. DOI: 10.1016/j.nima.2018.05.071. arXiv: 1802.01366 [physics.ins-det].

[49] Miroslav Alois Aaron Maria Gabriel. "Claws - a novel time resolved study of background during the first commissioning phase of SuperKEKB." PhD thesis. Föhringer Ring 6, 80805 München: Max-Planck-Institut für Physik & Technische Universität München, 2019.

[50] Hendrik Windel. "Scintillator Tiles with SiPM Readout for Fast Timing in SuperKEKB Commissioning." MA thesis. Föhringer Ring 6, 80805 München: Max-Planck-Institut für Physik & Technische Universität München, 2017.

[51] Miroslav Gabriel, Frank Simon, Hendrik Windel, et al. "A time resolved study of injection backgrounds during the first commissioning phase of SuperKEKB." In: (Dec. 2020). arXiv: 2012.10948 [physics.ins-det].

[52] FE-I4 Collaboration. *The FE-I4B Integrated Circuit Guide*. 2.3. 2012.

[53] P. Ahlburg. "Development of a FE-I4-based module for radiation monitoring with BEAST II during the commissioning phase of the Belle II detector." MA thesis. University of Bonn, 2016.

[54] A. Nomerotski et al. "PLUME collaboration: Ultra-light ladders for linear collider vertex detector." In: *Nucl. Instrum. Meth.* A650 (2011), pp. 208–212. DOI: 10.1016/j.nima.2010.12.083.

[55] I. Jaegle et al. "Compact, directional neutron detectors capable of high-resolution nuclear recoil imaging." In: (2019). DOI: 10.1016/j.nima.2019.06.037. arXiv: 1901.06657 [physics.ins-det].

[56] Karlheinz *Tscharlie* Ackermann. Mechanical Engineer; Max Planck Institute for Physics; Personal Conversation.

[57] D. Cuesta, J. Baudot, G. Claus, M. Goffe, K. Jaaskelainen, L. Santelj, M. Specht, M. Szelezniak, and I. Ripp-Baudot. "Operation of a double-sided CMOS pixelated detector at a high intensity e^+e^- particle collider." In: *Nucl. Instrum. Meth. A* 967 (2020), p. 163862. DOI: 10.1016/j.nima.2020.163862. arXiv: 2002.06941 [physics.ins-det].

[58] A. Natochii, S. E. Vahsen, H. Nakayama, T. Ishibashi, and S. Terui. *Improved simulation of beam backgrounds and collimation at SuperKEKB*. 2021. arXiv: 2104.02645 [physics.acc-ph].

[59] F. Simon, C. Soldner, and L. Weuste. "T3B — an experiment to measure the time structure of hadronic showers." In: *JINST* 8 (2013), P12001. DOI: 10.1088/1748-0221/8/12/P12001. arXiv: 1309.6143 [physics.ins-det].

[60] C. Adloff et al. "The Time Structure of Hadronic Showers in highly granular Calorimeters with Tungsten and Steel Absorbers." In: *JINST* 9 (2014), P07022. DOI: 10.1088/1748-0221/9/07/P07022. arXiv: 1404.6454 [physics.ins-det].

[61] CERN Courier. *'First turns' for SuperKEKB*. https://cerncourier.com/a/first-turns-for-superkekb/. 2016.

[62] Daniel Heuchel. "CLAWS in BEAST Phase II: Investigation of the Beam Background in the Commissioning of SuperKEKB." MA thesis. Föhringer Ring 6, 80805 München: Max-Planck-Institut für Physik & Technische Universität München, 2018.

[63] Yong Liu, Volker Büscher, Julien Caudron, Phi Chau, Sascha Krause, Lucia Masetti, Ulrich Schäfer, Rouven Spreckels, Stefan Tapprogge, and Rainer Wanke. "A Design of Scintillator Tiles Read Out by Surface-Mounted SiPMs for a Future Hadron Calorimeter." In: (2015). arXiv: 1512.05900 [physics.ins-det].

[64] Hamamatsu Photonics. *MPPC - Multi-Pixel Photon Counter*. Tech. rep. 2020. URL: https://hep.hamamatsu.com/resources/pdf/ssd/mppc_kapd0006e.pdf.

[65] Claudio Piemonte and Alberto Gola. "Overview on the main parameters and technology of modern Silicon Photomultipliers." In: *Nuclear Instruments and Methods in Physics Research Section A: Accelerators, Spectrometers, Detectors and Associated Equipment* 926 (2019). Silicon Photomultipliers: Technology, Characterisation and Applications, pp. 2 –15. ISSN: 0168-9002. DOI: https://doi.org/10.1016/j.nima.2018.11.119. URL: http://www.sciencedirect.com/science/article/pii/S0168900218317716.

[66] K. Kobayashi A. Ghassemi K. Sato. *MPPC*. Tech. rep. Hamamatsu Photonics, 2017. URL: https://www.hamamatsu.com/resources/pdf/ssd/mppc_kapd9005e.pdf.

[67] Carlos Mariñas. Technical Deputy; Universitat de València; Personal Conversation.

[68] Saint-Gobain Ceramics & Plastics, Inc. *"Premium Plastic Scintillators"*. Tech. rep. 2020-10-19. 2018. URL: https://www.crystals.saint-gobain.com/sites/imdf.crystals.com/files/documents/bc400-404-408-412-416-data-sheet.pdf.

[69] 3M. *Day lighting Film DF2000MA*. http://multimedia.3m.com/mws/media/7464690/3m-daylighting-film-df2000ma.pdf. (accessed 2020/03/09 at 3:15 pm).

[70] *SPDT RF SWITCH*. URL: https://www.minicircuits.com/pdfs/HSWA2-30DR+.pdf.

[71] *BGA614 - Silicon Germanium Broadband MMIC Amplifier*. 2011. URL: https://www.infineon.com/dgdl/Infineon-BGA614-DS-v02_01-en.pdf?fileId=db3a304314dca3890115418ffd35163a.

[72] Mini Circuits. *Coaxial Amplifier ZFL-500*. https://www.minicircuits.com/pdfs/ZFL-500.pdf. (accessed 2020/03/12 at 4:24 pm).

[73] F Hahn et al. *NA62: Technical Design Document*. Tech. rep. NA62-10-07. Geneva: CERN, 2010. URL: https://cds.cern.ch/record/1404985.

[74] Texas Instruments. *LMH6553 900 MHz Fully Differential Amplifier With Output Limiting Clamp*. Tech. rep. 2013. URL: http://www.ti.com/lit/ds/symlink/lmh6553.pdf.

[75] Picotech Technology. *PicoScope 6000 Series*. Tech. rep. 2016.

[76] Lev Davidovich Landau. "On the energy loss of fast particles by ionization." In: *J. Phys.* 8.4 (1944), pp. 201–205. URL: https://cds.cern.ch/record/216256.

[77] National Instruments. *Labview*. https://www.ni.com/de-de/shop/labview.html.

[78] Boost. *Boost C++ Libraries*. http://www.boost.org/. 2020.

[79] Rene Brun and Fons Rademakers. "ROOT - An Object Oriented Data Analysis Framework." In: *Proceedings AIHENP'96 Workshop*. https://root.cern.ch. Nucl. Inst. & Meth. in Phys. Res. A 389 (1997), Sept. 1996, pp. 81–86.

[80] Picotech Technology. *PicoScope 6 Software & Drivers*. https://www.picotech.com/downloads/linux.

[81] Gabime. *spdlog - Very fast, header-only/compiled, C++ logging library*. https://github.com/gabime/spdlog.

[82] Argonne National Laboratory. *EPICS - Experimental Physics and Industrial Control System*. https://epics.anl.gov/.

[83] Paul Scherrer Institute. https://github.com/paulscherrerinstitute/pcaspy.

[84] Picotech Technology. *PicoScope 6000 Series Programmers Guide*. Tech. rep. 2016.

[85] Hendrik Windel and Thomas Kraetzschmar. *CAT - The Claws Analysis Toolkit*. https://github.com/HendrikLamar/cat.

[86] CSS Developement Team. http://controlsystemstudio.org/.

[87] Pauli Virtanen et al. "SciPy 1.0: Fundamental Algorithms for Scientific Computing in Python." In: *Nature Methods* 17 (2020), pp. 261–272. DOI: 10.1038/s41592-019-0686-2.

[88] F. Pedregosa et al. "Scikit-learn: Machine Learning in Python." In: *Journal of Machine Learning Research* 12 (2011), pp. 2825–2830.

[89] R. Wigmans. *Calorimetry: Energy Measurement in Particle Physics*. International Series of Monographs on Physics. Oxford University Press, 2008. ISBN: 9780198502968.

[90] R.H. Landau, M.J. Páez, and C.C. Bordeianu. *Computational Physics: Problem Solving with Computers*. Wiley, 2007. ISBN: 9783527406265. URL: https://books.google.de/books?id=RBg-vgAACAAJ.

[91] Michael Waskom and the seaborn development team. *mwaskom/seaborn*. Version latest. Sept. 2020. DOI: 10.5281/zenodo.592845. URL: https://doi.org/10.5281/zenodo.592845.

[92] Ivan Popov. "CLAWS for Beam Abort." MA thesis. Technische Universität München, 2022.

[93] Ivan Popov. *39th B2GM - MDI Session - CLAWS for Beam Abort in SuperKEKB*. Master student in the Future Detectors Group at the Max Planck Institute for Physics.

[94] *FOPRA Experiment 26: Silicon-based Photon Detectors in Particle Physics Experiments*. 2020. URL: https://www.ph.tum.de/academics/org/cc/course/950597521/.

ACKNOWLEDGMENTS

First of all, I would like to express my gratitude to Hans-Günther Moser and Frank Simon. You both supported me endlessly during my thesis with an outstanding supervision, fruitful discussions and lots of advice. It was like having two excellent supervisors. Without any doubt I can say that CLAWS is by far the best PhD project I could ever have imagined. Thank you so much for this opportunity and all the possibilities you offered me. I will always remember my shift in the SuperKEKB control room during the first collisions. Once more I would like to thank Frank Simon who constantly supported and advised me since I started in his group at the MPI for Physics in 2014.

I would also like to express my gratitude to Prof. Allen Caldwell for accepting me as a PhD student and giving me the opportunity writing this thesis. Special thanks goes to Prof. Christian Kiesling for explaining me so much physics and introducing me to *Salmon Pepper*, the best sushi ever. So many thanks goes to my one and only office mate Miro. No matter if we have been in the container or in Tokyo, the time was always awesome. Marco, without you I would be a much worse programmer. Thank you for your endless patience. Thanks Christian, for discussing so many physics and statistics cases with me and the intense and endless matches of table tennis. I really enjoyed sharing the moments and coffee breaks in the container with my current and former colleagues of the Belle and Future Detectors working group: Benedikt, Daniel, 2x Fabian, 2x Felix, Fernando, Ivan, Justin, Lorenz, Malinda, Markus, Naomi, Philipp, Swathi, Thibaud and Thomas.

I would like to say *thank you* to all the Belle 2 members for the inspiring and unforgettable months in Japan. Special thanks goes to Hiro, David, Shuji, Tscharlie, Karsten and Carlos who helped me fixing all the issues which happened during the detector installations. I highly appreciate the endless hours of working and team building together with Botho & Patrick at KEK. There is a special place in my heart for you two! I am deeply grateful to Caleb, Cate, Jeff and Zac for the seemingly endless hours of playing Imperial Assault and the enjoyable time we had together. Thank you Alex, Michael, Oskar and Peter for the never ending B2GM parties.

Finally, I would like to say thank you to my friends and family. You always supported me in all these times. A very special thanks goes to my wife Sina. You gave me endless support and never complained when, for example, I spend more time of the year in Japan than in Germany. I am so thankful for your constant backing - especially during the last few month when I was 'almost done' with the thesis. I owe you so much. I love you.

Reactions in the Belle 2 *(left)* & SuperKEKB *(right)* control rooms during the first collisions of the SuperKEKB collider.

COLOPHON

This document was typeset using the typographical look-and-feel `classicthesis` developed by André Miede and Ivo Pletikosić. The style was inspired by Robert Bringhurst's seminal book on typography "*The Elements of Typographic Style*". `classicthesis` is available for both LaTeX and LyX:

https://bitbucket.org/amiede/classicthesis/

Happy users of `classicthesis` usually send a real postcard to the author, a collection of postcards received so far is featured here:

http://postcards.miede.de/

Thank you very much for your feedback and contribution.

Final Version as of December 22, 2021 (classicthesis v4.6).